Parois, Pascal (2010) *The effect of pressure on clusters, chains and single-molecule magnets.* PhD thesis.

http://theses.gla.ac.uk/1789/

The effect of pressure on clusters, chains and single-molecule magnets

Pascal Parois
<pascal@parois.net>

Submitted in fulfilment of the requirements for
the Degree of Doctor of Philosophy

Department of Chemistry
Faculty of Physical Sciences
University of Glasgow

Supervisor : Mark Murrie

Glasgow, 14th February 2010

Abstract

This research deals with the investigation of the correlation between the structures of molecules and their magnetic properties as a function of pressure. To do so, different kinds of molecules have been chosen from single-molecules magnets, chains to small molecules. The variety of molecules is necessary to find the best candidates for high pressure X-ray crystallography and high pressure magnetic measurements.

Bonds lengths and angles have been successfully altered by using high pressure without the complicating issues of chemical modifications. These structural changes produced a significant effect on the magnetic properties. A tilting of the Jahn-Teller axis in $[Mn_{12}O_{12}\text{-}(O_2CCH_2Bu^t)_{16}(H_2O)_4] \cdot MeNO_2 \cdot CH_2Cl_2$ has been observed both structurally and magnetically. Modification of $\pi\cdots\pi$ interactions from edge to edge interaction to offset $\pi\cdots\pi$ stacking in $[Gd(PhCOO)_3(DMF)]_n$ or a conversion from a $CH\cdots\pi$ interaction to a $\pi\cdots\pi$ interaction in $[N(PhCH_2)(CH_2CH_3)_3]_2[Fe_2OCl_6]$ are also reported.

Contents

List of Tables

List of Figures

Acknowledgements

I would like to begin by thanking my supervisor Mark Murrie and all the “Murrie group” for their help and guidance throughout the project.

I would like to thank, in alphabetical order of first names, Alex Prescimone, Fraser White, Russell Johnstone, Simon Parsons and Stephen Moggach for all the high pressure X-Ray crystallography done in Daresbury and Edinburgh. Not to forget all the good fun of doing crystallography at 3 am in the morning during the night shifts…Or not ☺. Thank to John E. Warren for running station 9.8 so smoothly, he is the only one able to produce X-rays with flying pigeons, well done!

For the magnetic measurements and the piston-cylinder pressure cell, Javier Sanchez Benitez, Gaétan Giriat and Konstantin Kamenev at CSEC, Edinburgh university. Not to forget Jim Gallagher and Mark Murrie in Glasgow to let me use the MPMS for weeks.

I am very grateful to all the persons who corrected this thesis.

Because a PhD is not only about work (really?), I would like to thank Guilaine for countless numbers of chats when I got bored of chemistry.

Acronyms

DAC	Diamond anvil cell (Section 2.1.1).
EPR spectroscopy	Electron Paramagnetic Resonance or EPR, often called Electron Spin Resonance (ESR) is a technique to study paramagnetic molecules. The basic physical concepts of EPR are analogous to those of nuclear magnetic resonance (NMR), but it is electron spins that are excited instead of spins of atomic nuclei.
FR species	Fast relaxing species. See LT species.
GMR	Giant magnetoresistance.
HF-EPR	High-field, high-frequency EPR spectroscopy. See EPR spectroscopy.
LINAC	Linear particle accelerator.
LT species	Low temperature species. Also called fast relaxation species. Mn_{12} analogues exist in two different forms depending on their energy barrier (Section 1.1.3).
HT species	High temperature species. Also called slow relaxation species. Mn_{12} analogues exist in two different forms depending on their energy barrier (Section 1.1.3).
MPMS	Magnetic Property Measurement System (from the Quantum Design company).
PPMS	Physical Property Measurement System (from the Quantum Design company).
QTM	Quantum tunneling of the magnetisation.
SMM	Single-molecule magnet.
SR species	Slow relaxing species. See HT species.

Chapter 1

Introduction

1.1 Magnetism, data storage and single-molecule magnets

Magnetism is fundamental, many applications rely on it: from the magnetism discovered in the fourth century BC in China, the compass for navigation discovered in the twelfth century, the dynamo and the electric motor discovered in the nineteenth century to data storage in twentieth century. Where does the magnetism come from? How do the magnetic moments interact with each other?

1.1.1 Magnetic properties and interactions

> *"Magnetism: phenomenon associated with the motion of electric charges. This motion can take many forms. It can be an electric current in a conductor or charged particles moving through space, or it can be the motion of an electron in atomic orbit. Magnetism is also associated with elementary particles, such as the electron, that have a property called spin."*
>
> Magnetism. (2009). In Encyclopædia Britannica. Retrieved June 10, 2009, from Encyclopædia Britannica Online.

Only the magnetic moment created by an electron will be discussed.

Each electron circulating around the nucleus creates a magnetic moment (Figure 1.1), it is the orbital component (quantum number m_l) which is responsible for the diamagnetic

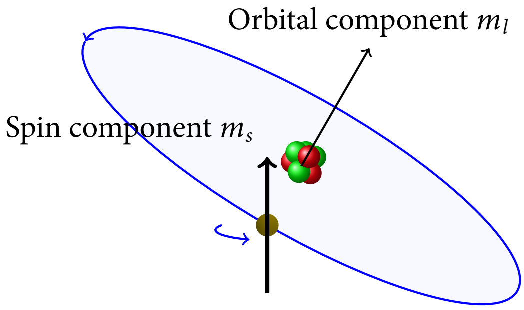

Figure 1.1: Magnetic moments created by an electron.

properties of a material. The diamagnetic component of the magnetic susceptibility is always negative but usually small compared to the magnetic moment created by the spin of the electron (quantum number m_s).

The magnetic properties of any substance can be characterised by its response to an external magnetic field. In paramagnetic materials, the magnetic moments created by the spin of unpaired electrons (Figure 1.1) tend to orient along the external field. These materials are slightly attracted by a magnetic field. Only unpaired electrons can result in a net magnetic moment as the Pauli principle states: "The wavefunction for any system of electrons must be antisymmetric with respect to the interchange of any two electrons".[1] As a result, two electrons cannot have the same four quantum numbers n, l, m_l and m_s. The spin magnetic moment μ_z is:[1] (with g_e the electron g-factor, e the electron charge, $\bar{h}$ the reduced Planck constant, m_e the electron mass and m_s the magnetic spin).

$$\mu_z = -\frac{g_e e \bar{h}}{2m_e} m_s \tag{1.1}$$

Consequently, a fully occupied orbital with two electrons of opposite spin results in the cancellation of the magnetic moment.

In paramagnetic materials, there is no strong correlation between the magnetic moments. Where there are magnetic interactions, there are two different kinds of interactions. All the magnetic dipoles are parallel and the magnetisation is maximal, this is ferromagnetism (Figure 1.2). Or, all the magnetic dipoles are anti-parallel and the magnetisation is zero when all the dipoles are identical, this is anti-ferromagnetism (Figure 1.2). When in the anti-ferromagnetic ordering the values of the elementary magnetic moments of opposite orientation are different and the net magnetic moment is non zero, this is ferrimagnetism[1] (Figure 1.2). The last interaction is super-paramagnetism: independent ferromagnetic or ferrimagnetic domains behave as a paramagnetic material (Figure 1.2). Single molecule-magnets are super-paramagnets as each molecule behaves as a tiny ferromagnet or ferrimagnet but due to the very weak coupling between the molecules, the resulting material is paramagnetic.

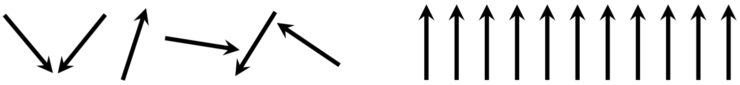

(a) Paramagnetism

(b) Ferromagnetism

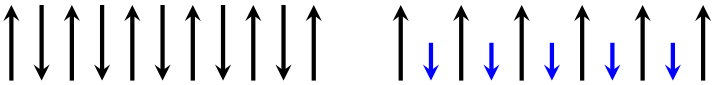

(c) Anti-ferromagnetism

(d) Ferrimagnetism

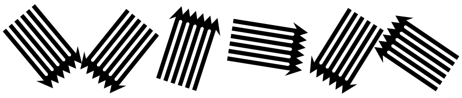

(e) Super-paramagnetism

Figure 1.2: Magnetic interactions.

As magnetic molecules are often composed of more than one type of atom, interactions between atomic dipoles can occur. Direct interaction between two paramagnetic atoms usually leads to an anti-ferromagnetic interaction as the Pauli principle states that two electron in the same orbital cannot have the same spin number. Exchange interactions between non-neighbouring magnetic ions mediated by a non magnetic ion depend on the orbitals involved. Therefore, the magnitude and sign of the exchange interaction depends upon the metal-ligand distance and the the metal-ligand-metal bridging angle (Figure 1.3).[2]

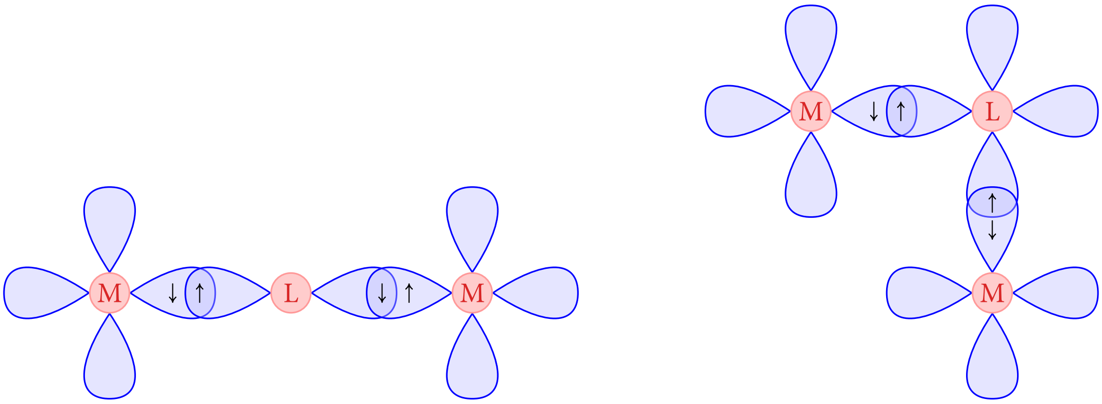

(a) Anti-ferromagnetic interaction through a linear link

(b) Ferromagnetic interaction through a 90° angle link

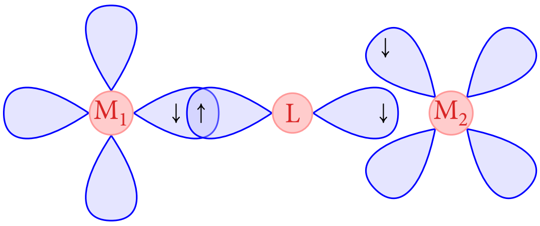

(c) Ferromagnetic interaction between two different metal centres

Figure 1.3: Common super-exchange interactions. Credits: Kettle[3].

1.1.2 21st century data storage

Magnets used for information storage rely on ferromagnetic interactions in which all the magnetic moments are parallel to each other. The Curie temperature needs to be higher than the ambient temperature. It is also necessary to have a bistable state in order to represent the state of the bit (1/0). The physical representation is a hysteresis loop due to the magnetic anisotropy of the material.

Magnetic recording has been used since 1900.[4] In 1956 IBM released the IBM 305 RAMAC (RAMAC stood for Random Access Method of Accounting and Control), a computer which included the first magnetic hard drive (IBM 350) publicly available. It was composed of fifty twenty four inches plates (figure 1.4) with an areal density of 2 kbit in^{-2} and a total capacity of about 5 MB.

Since then, the capacity of a hard drive based storage media has doubled every 12–18 months.[5] In January 2009, Seagate, a hard drive manufacturer, claimed to release a hard drive with the industry's highest areal density. Packing 1 TB of capacity on just two plate disks, Seagate's Barracuda® 7200.12 HD, a 3.5-inch 7200-RPM drive features an areal density of 329 Gbit in^{-2}[*]. This is a 1.6×10^8 increase over 53 years. Two revolutions have driven this phenomenal increase: the GMR (giant magnetoresistance) effect discovered by Peter Grünberg and Albert Fert (awarded the Nobel prize in 2007[6]); and the perpendicular recording technology.[5] The GMR effect permitted the fabrication of very sensitive heads for the reading of the magnetic field. The perpendicular recording flips the orientation of a bit from the surface into the thickness of the media (the magnetic moment is perpendicular to the surface) which allows higher areal density, it is believed that an areal density of 500-600 Gbit in^{-2} can be reached with a cobalt alloy based magnetic material.[5]

The main problem for the increase of the areal density is the super-paramagnetic effect (Figure 1.2). Normally, coupling forces in ferromagnetic materials cause the magnetic moments of neighbouring atoms to align, resulting in very large internal magnetic fields. On increasing the areal density, domains are becoming smaller and smaller, as a result, the number of magnetic interactions decreases. At some point, the thermal energy becomes sufficient to flip the magnetisation of the magnetic domain.

Current systems use two or more ferromagnetic layers which are anti-ferromagnetically coupled to the recording layer to reduce the effect of super-paramagnetism.[5] Future im-

---

[*] July 2009 update: new highest areal density of 394 Gbit in^{-2} for the seagate Momentus® 5400.6

provements include: suitable writing heads for new materials with higher coercive fields less sensitive to the super-paramagnetic effect;[7] percolated media; heat-assisted magnetic recording (allows current head to write high coercive material); discrete-track recording and patterned media recording.[5] With these developments it is difficult to speculate to the final maximum areal density possible. Terris[8] suggests that 10 Tbit in^{-2} may be possible with a suitable writing head.

Currently, materials used to store information are based on cobalt alloys, predominantly CoPtCrB alloys.[5] A random distribution of grains is dispersed all over the surface, the media itself is featureless, and the head defines all the bit locations. However, in patterned media, the bit locations are predefined on the disk and confined on small single domain "islands".

In order to reach even higher density, it is necessary to find smaller bits. At 10 TB in^{-2}, the bit area is already at 64.5 nm^2.[8] Molecules have a smaller size usually less than a few nano-metres. Obviously, these molecules require one or more centres with an unpaired electron such as metallic ions or radicals in order to have a net magnetic spin and an easy-axis magnetic anisotropy (D). No intermolecular magnetic interactions should be present, so the molecules are magnetically independent and could be used for data storage. Such molecules are called single-molecule magnets or SMMs, they represent a molecular approach to nano-magnets (nanoscale magnetic particles).

Single molecule magnets can theoretically be used to store data information, each molecule can store one bit. The most famous single molecule magnet, the Mn_{12} acetate, is contained in a cube of about 1.5 nm which gives a theoretical areal density of 0.3 Pbit in^{-2}. At the current trend, a 43 % increase per year, this density could be reached within twenty years. As the Mn_{12} acetate is only a SMM below 4 K, a lot of research is necessary, not only on the recording medium but on the head, the reading-writing technology, as well.

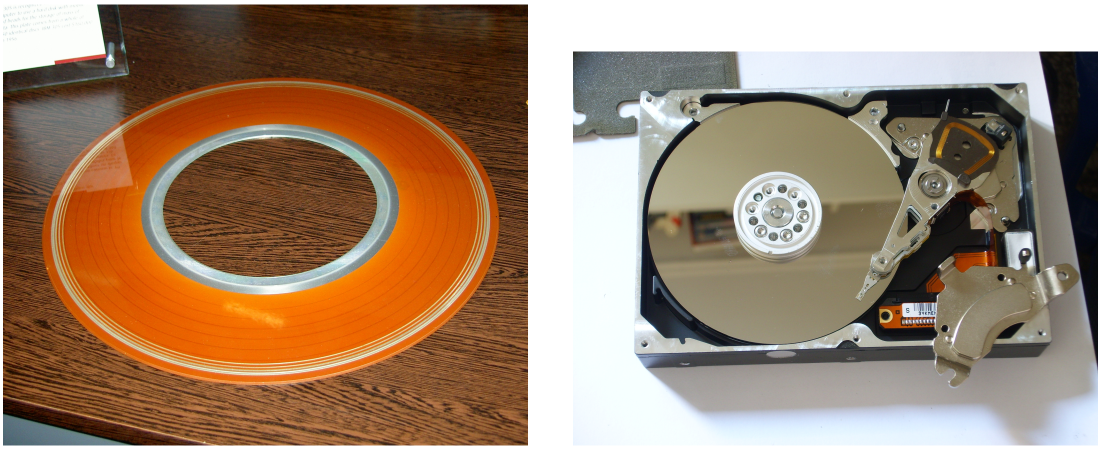

Figure 1.4: On the left: plate from the hard disk of a 1956 RAMAC 305 IBM computer. The scratch is the consequence of a crash of the head on the plate. Permission: GFDL, author: Mikaël Restoux. On the right, plate from a modern hard disk, 3.5 in diameter. Permission: CC-by-sa-3.0, author: Alessio Sbarbaro.

1.1.3 Single-molecule magnets

The first molecular magnet was reported in 1967 by Wickman *et al.*[9] They found that [Fe(dtc)$_2$Cl], monochlorobis(diethyldithiocarbamato) iron(III), has a $S = 3/2$ ground state and in the crystalline state ferromagnetically orders at 2.46 K. There was not much further activity in this area until in 1987 Miller *et al.*[10] reported that decamethylferrocenium tetracyanoethenide, [Fe(Cp*)$_2$][TCNE], ferromagnetically orders at T_c = 4.8 K. The first and most famous single-molecule magnet was reported in 1993 when Sessoli *et al.*[11] discovered a $[\mathrm{Mn_{12}O_{12}(MeCO_2)_{16}(H_2O)_4}] \cdot 2\,\mathrm{CH_3COOH} \cdot 4\,\mathrm{H_2O}$ (**1**) complex, first synthesized in 1980,[12] to exhibit a barrier to spin reversal after applying a strong magnetic field below 4 K. The term single molecule-magnet was only first employed in 1996 by George Christou and David N. Hendrickson.[13]

Nowadays hundreds of papers on SMMs have been published.[14,15] Other systems have been found based on manganese, nickel, iron, cobalt or other transition metal ions. They can be used to synthesise giant spin SMMs like $[\mathrm{Mn^{III}_{12}Mn^{II}_7O_8(N_3)_8}$-$\mathrm{(HL)_{12}(MeCN)_6]Cl_2}$ ($\mathrm{H_3L}$ = 2,6-bis(hydroxymethyl)-4-methylphenol);[16] high anisotropy energy barrier Mn$_6$ clusters such as $[\mathrm{Mn^{III}_6O_2(Et{-}sao)_6(O_2CPh(Me)_2)_2(EtOH)_6}]$ (Et–saoH$_2$ = 2-hydroxyphenylpropanone oxime)[17] or the most famous iron SMM: $\{[\mathrm{(tacn)_6Fe_8(\mu_3{-}O)_2(\mu_2{-}OH)_{12}]Br_7(H_2O)}\}\mathrm{Br} \cdot \mathrm{H_2O}$ (tacn = 1,4,7-triazacyclononane).[18] The energy barrier is the energy necessary to flip the orientation of the magnetisation. In SMMs, there are two ways to overcome the energy barrier: a classical way where the energy given to the system is higher than the barrier (magnetic fields or temperature for example). The barrier can also be crossed by quantum tunnelling through the barrier on the condition that energy levels are identical on both sides of the barrier.

Some SMMs are also based on lanthanide ions like dysprosium(III) and terbium(III). For example the Ln monomer: $[\mathrm{Pc_2Tb}]^- \mathrm{TBA}^+$ (Pc = dianion of phthalocyanine, TBA$^+$ = $(\mathrm{C_4H_9})_4\mathrm{N}^+$).[19,20] Finally some SMMs contain two different metals such as a transition metal ion and a lanthanide ion. Osa *et al.*[21] prepared a mixed metal SMM: $[\mathrm{Cu^{II}LTb^{III}}$-$\mathrm{(hfac)_2]_2}$ where $\mathrm{H_3L}$ = 1-(2-hydroxybenzamido)-2-(2-hydroxy-3-methoxy-benzylideneamino) ethane and Hhfac = hexafluoroacetylacetone, and $[\mathrm{Mn_{11}Dy_4O_8(OH)_6(OMe)_2}$-$\mathrm{(O_2CPh)_{16}(NO_3)_5(H_2O)_3}]$ behaves as a SMM below 1 K.[22]

Mn$_{12}$ acetate analogues remain the most studied SMMs. They can be prepared by either direct synthesis or by exchange of the acetic acid ligand from $[\mathrm{Mn_{12}O_{12}(MeCO_2)_{16}}$-$\mathrm{(H_2O)_4}] \cdot 2\,\mathrm{CH_3COOH} \cdot 4\,\mathrm{H_2O}$.[11,23–27] It has been found that these analogues can be put into two categories. One kind shows an energy barrier of around 60 K and a frequency dependent out-of-phase AC signal around 4-7 K. These analogues are called slow relaxation species (SR) or high temperature species (HT). The other kind shows an energy barrier of around 40 K and a frequency dependent out-of-phase AC signal around 2-3 K. These analogues are called fast relaxation species (FR) or low temperature species (LT).

The majority of the Mn_{12} acetate analogues exhibit both fast relaxing and slow relaxing features depending on how the product has been synthesised. Mn_{12} acetate, for example, is always obtained in a mixture with a proportion of the FR species around of 5 %. Structure determination with X-ray diffraction does not reveal the presence of the impurity whereas out of phase AC susceptibility clearly reveals a peak at low temperature corresponding to the FR species. This is most likely because 5 % disorder in a heavy metal complex would show larger residual electron density but be masked by the deformation in the difference map from the heavy metals themselves or that the 5 % is not present until the low temperature of the magnetic data collections. X-ray data collection on SMMs are not done routinely below 80 K. The fast relaxing species has been seen by X-ray diffraction only on pure FR samples or where the FR species is the major species. $[Mn_{12}O_{12}(O_2CC_6H_4{-}p{-}Me)_{16}(H_2O)_4] \cdot HO_2CC_6H_4{-}p{-}Me$,[28] $[Mn_{12}O_{12}(O_2CC_6H_4{-}p{-}Bu^t)_{16}(H_2O)_4] \cdot CH_2Cl_2$[28] and $[Mn_{12}O_{12}(O_2CCH_2Bu^t)_{16}(H_2O)_4] \cdot CH_2Cl_2 \cdot MeNO_2$ (**2a**)[26] are such complexes.

The crystallisation solvent is also important in determining the species obtained during the crystallisation. Soler *et al.*[26] discovered a complex that exhibits purely either of the two species depending on the crystallisation solvent: $[Mn_{12}O_{12}(O_2CCH_2Bu^t)_{16}(H_2O)_4] \cdot CH_2Cl_2 \cdot MeNO_2$ (**2a**) is purely a FR species, it crystallises with $MeNO_2$ and CH_2Cl_2. $[Mn_{12}O_{12}(O_2CCH_2Bu^t)_{16}(H_2O)_4] \cdot CH_2Cl_2 \cdot CH_3CN$ (**2b**) is purely a SR species, it crystallises with CH_3CN and CH_2Cl_2. The two complexes exhibit two different relaxation rates of the magnetization, with out-of-phase peaks in the 2-4 K region for complex **2a** (LT form) and out-of-phase peaks in the 5-7 K range for complex **2b** (HT form). The LT form has a smaller energy barrier than the HT form. A desolvation of complex **2a** also produces the SR species but the structure from X-ray diffraction could not be determined. However, the position of the out of phase AC susceptibility peaks strongly suggest a tilting of one Mn(III) Jahn-Teller axis.[26]

Takeda *et al.*[27],[29] reported that the fast relaxation species is due to a tilt of elongated Jahn-Teller bond on one of the manganese (III) ions from “vertical” to “horizontal” and reported a comparative magnetic, EPR spectroscopy and crystallographic study of SR and FR species in 1998 and 2002. The easy axis tilting has also been studied by using EPR spectroscopy by Takahashi *et al.*[30].

1.1.4 SQUID magnetometry

The principle aim of magnetometry is to measure the magnetisation (either intrinsic or induced by an applied field) of a material. This can be achieved in a number of ways utilising various magnetic phenomena. Magnetometry data in this thesis has been recorded using a SQUID (Superconducting Quantum Interference Device).

A SQUID is a very sensitive magnetometer used to measure the induced or remanent magnetic moment in a sample, usually as a function of the applied magnetic field and temperature. A SQUID magnetometer-susceptometer (SQUID-MS) combines several superconducting components, including a SQUID, superconducting magnet, detection coils, flux transformers and superconducting shields.[31] To make a measurement, a sample, typically a few cubic millimetres, is put in a gelatine capsule which is put itself in a straw. The straw is then attached to a sample rod. For high pressure measurements, the pressure cell is directly screwed to a modified sample rod. The sample is then scanned through a second-order superconducting gradiometer which is coupled to a SQUID. The SQUID itself consists of a superconducting ring with a small insulating layer known as a "weak link".[31] The SQUID is situated away from the sample and is coupled with the detection coils. The weak link is also known as a Josephson junction[32,33] (Figure 1.5). The signal from the SQUID is then processed in order to obtain the magnetic moment. If a constant biasing current is maintained in the SQUID device, the measured voltage oscillates with the changes in phase at the two junctions, which depends upon the change in the magnetic flux. Counting the oscillations allows you to evaluate the flux change which has occurred.

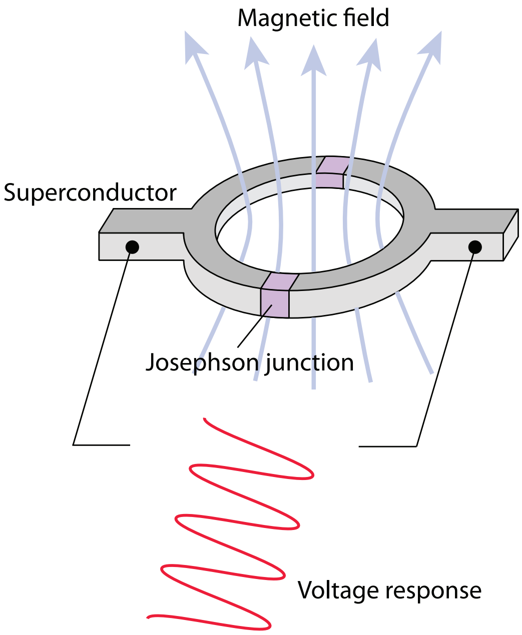

Figure 1.5: SQUID schematic details.

1.2 X-ray diffraction and synchrotron light source

Small molecule single crystal synchrotron X-ray crystallography only became a reality in the UK in 1997 with the creation of Station 9.8 at the Synchrotron Radiation Source (SRS) located at Daresbury.[34] Station 9.8 (Figure 1.6), which has been used to obtain all X-ray diffraction results of this research, utilises up to 3.8 mrad of the horizontal radiation fan from a 5 Tesla wiggler magnet placed in the SRS storage ring. This insertion device, consists of a liquid helium supercooled array of magnets arranged with alternating field directions to force electrons into a sinusoidal trajectory through the "straight" sections of a synchrotron storage ring path, which permits higher intensity radiation compared to the SRS conventional bending magnets.

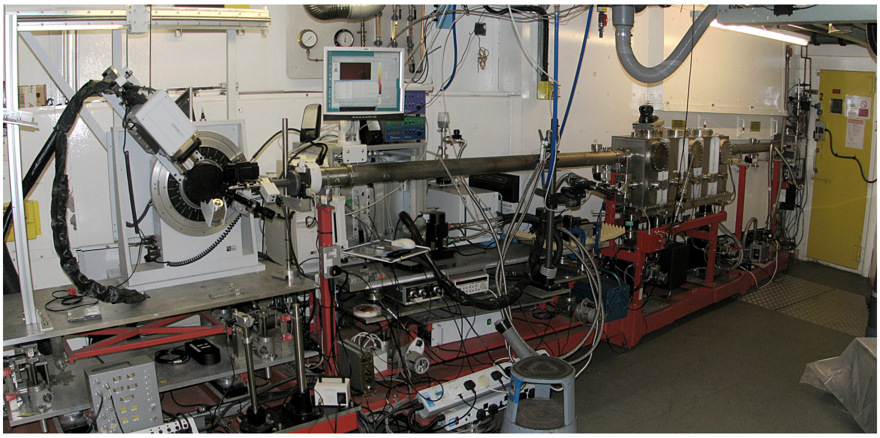

Figure 1.6: Station 9.8 hutch at Daresbury.

The SRS is a second generation synchrotron facility, which itself is a particular type of cyclic particle accelerator in which an applied magnetic field is used to bend the trajectory of the electrons, whilst simultaneously an electric field is used to accelerate them in a carefully synchronized way to produce a travelling electron beam.[35,36] The SRS was closed during my PhD in 2008 (Figure 1.7).

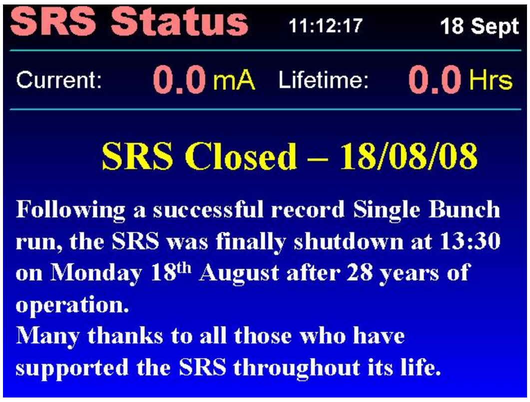

SRS Status 11:12:17 18 Sept

Current: 0.0 mA Lifetime: 0.0 Hrs

SRS Closed – 18/08/08

Following a successful record Single Bunch run, the SRS was finally shutdown at 13:30 on Monday 18th August after 28 years of operation.
Many thanks to all those who have supported the SRS throughout its life.

Figure 1.7: SRS shut down.

The SRS is composed of three main parts: a LINAC (right, Figure 1.8), a synchrotron booster (middle, Figure 1.8) and the storage ring (left, Figure 1.8).

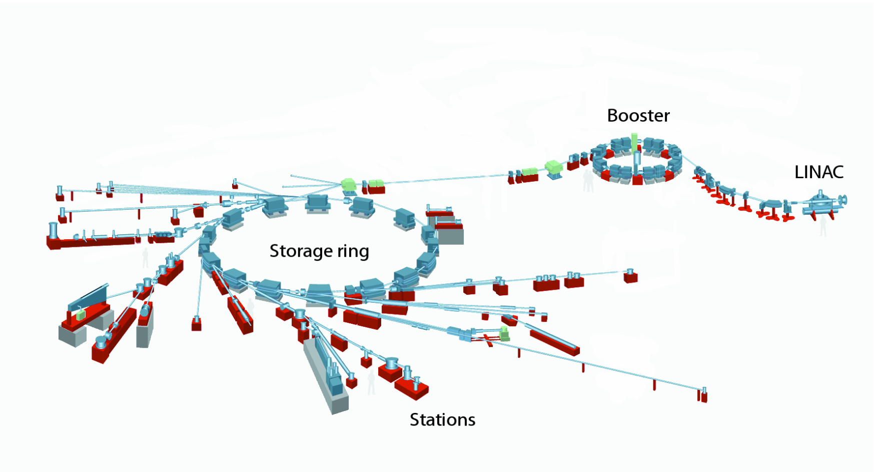

Figure 1.8: Schematic of the Daresbury synchrotron. Credits: SRS, John E. Warren

The LINAC is a linear accelerator and first accelerates the electrons at 12 MeV. Then the electrons are injected into the synchrotron booster, a 10 m diameter ring, where they are accelerated at 600 MeV. Finally, the electrons are injected into the storage ring, 30.5 m in diameter and accelerated at their nominal energy, 2 GeV. Injections into the storage ring are routinely made once a day depending upon beam type, user and storage ring vacuum conditions. Two principle modes of operation were available to the SRS users: multi-bunch and single bunch. These modes differed in the electron packet structure which subsequently affected the intensity of the radiation available to the beam-line stations.

The work undertaken during this thesis at the SRS utilised only multibunch mode (the most intense radiation mode).

X-ray radiation produced by a synchrotron source has several advantages compared to conventional laboratory X-ray sources. Advantages are that the light is at very high intensity and with a very low beam divergence. These two characteristics allow small crystals and weakly diffracting samples to be used. Another advantage is the ability to select from a wide range of X-ray energies or wavelengths. Station 9.8 had access to a wavelength range from 0.3 Å to 1.5 Å.

These characteristics are particularly useful for high pressure experiments as the chamber space is very small, effectively defining the maximum sample size and located behind two diamonds which act as weak but present X-ray absorbers, thus requiring the high intensity and good X-ray beam homogeneity and size. The completeness of data sets may be as low as 20 % due to the shading of the pressure cell, and this introduces problems in structure solution and refinement. Again, for high pressure experiments, access to short wavelengths allows a higher completeness of the data compared to longer wavelengths. On Station 9.8 conventional X-ray diffraction was undertaken at the Zr X-ray absorption edge (0.6889 Å) which gave a resolution of 0.68 Å at a detector position of $\theta = 30°$. Shorter wavelengths allow higher completeness, as a result. For high pressure single crystal diffraction a wavelength close to the Ag X-ray absorption edge (0.4859 Å)[†] was normally selected. This wavelength gave a compromise between the X-ray scattering efficiency of both light and heavy atoms whilst providing sufficient access to higher resolution data.

The design of station 9.8 allowed for ready access to this wavelength. The white radiation emitted from the wiggler is first focused and wavelength selected via a conventional Si(111) monochromator. A copper plate sits on the back of the monochromator and both sit in a gallium/indium/tin eutectic pool cooled by water. Focusing was achieved via a small bend being placed on the triangular shaped crystal (Figure 1.9). The monochromatic radiation produced from this device utilises Bragg's law and because the source is white, that is all wavelengths, Bragg's law is obeyed for higher diffraction planes of the Si(111) crystal. This results in an X-ray beam of predominantly one wavelength with a very small spread around the principle wavelength λ but also higher harmonics from the other Bragg allowed diffraction planes such as the Si(333) plane producing a wavelength known as the third harmonic $\lambda/3$. This is $1/3$ the wavelength of the principle beam and substantially less intense. To remove the higher harmonics, that is to undertake higher har-

---

[†] `http://skuld.bmsc.washington.edu/scatter/AS_periodic.html` and sources therein

monic rejection, the beam is passed through a second X-ray optic in the form of a mirror. The mirror focuses the beam in the other plane far more efficiently than the monochromator producing a highly focussed asymmetric monochromatic source. To remove the asymmetry the beam is finally passed through a conventional X-ray collimator and shutter assembly before sample exposure. Conventionally, for high pressure experiments a collimator size of 500 microns was selected. This gave a beam significantly greater than the sample but utilised the cell's own tungsten gasket (see next section) as a secondary collimator.

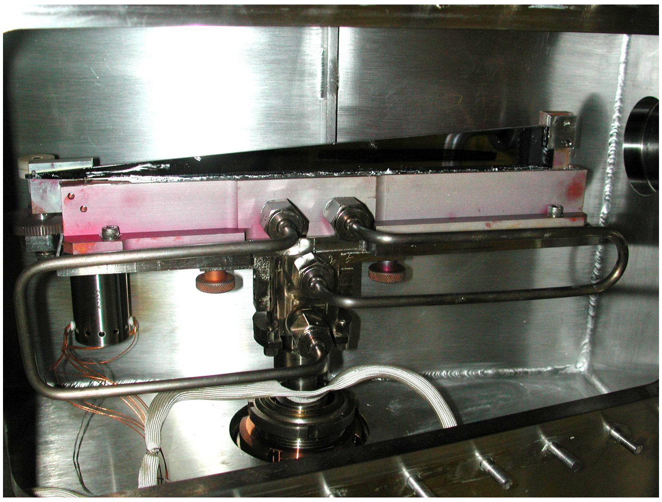

Figure 1.9: Si(111) monochromator at Station 9.8, SRS, Daresbury. Credits: SRS, John E. Warren

Other characteristics of synchrotron light sources are pulsed light emission and a high level of polarisation. The pulse durations are not normally accessed or considered relevant in high pressure or conventional small molecule single crystal diffraction modes, whilst the polarisation forces the diffractometer geometry to be arranged differently to conventional laboratory sources.

1.2.1 Structural Changes at High Pressure

Pressure has most effect on inter-molecular interactions by reducing as much as possible voids in the structure. Intra-molecular bond distances and angles modifications can also take place. These include changes in metal-ligand distances; angular changes at bridging ligands; changes in spin state and increases in coordination number.

The effect of pressure on the crystal structures of approximately half of the 20 naturally occurring amino acids has been studied by Moggach *et al.*[37] using X-ray diffraction. Very few investigations of di- or oligopeptides have been published. Beyond 10 GPa remains largely *terra incognita*. Crystallographic confirmation of high-pressure polymorphism has been obtained for glycine, L-cysteine, L-serine, L-leucine and L-alanine; spectroscopic evidence for transitions has been seen for DL-valine and L-threonine. Initially, compression of interstitial voids occurs. The compression occurs anisotropically. Those contacts that are long by comparison with averages drawn from the Cambridge Database usually compress the most.[37] "Super-short" contacts are apparently not formed in organic crystals up to about 10 GPa. Compression may occur until one contact in the structure has reached a lower limit, and this limit is predictable from a survey of ambient pressure structures in the Cambridge Database.[37,38] Present work in this thesis also shows the same behaviour on the molecule studied. The highest pressure study yet performed in this field is on α-glycine at 23 GPa[39] using Raman scattering technique.

Crystallographic work on transition metal complexes at high pressure has been used broadly either to explore intra- and inter-molecular potentials, or to modify the properties of functional materials. High pressure crystallographic studies on molecular transitional metal compounds are quite rare.[40] The effect of pressure on metal carbonyls has been studied extensively by vibrational spectroscopy, and an excellent summary of work carried out prior to 2000 is available in a review by Edwards and Butler[41]. Dramatic changes in IR or Raman spectra have been shown to occur in some compounds, indicating that some substantial molecular rearrangement has occurred. The geometry of $Ru_3(CO)_{12}$[42] has been studied by high pressure crystallography. Intra-molecular and inter-molecular interactions have been investigating in $Co_2(CO)_6(PPh_3)_2$[43] or $[4-\text{chloropyridinium}]_2[CoX_4]$ where X = Cl or Br.[44] High pressure can also be used to form bonds, for example in the formation of a new Sb–Cl bond in $[Me_2N(H)CH_2CH_2NH_3][SbCl_5]$.[45] A large variety of modifications can be induced by pressure.

1.3 Correlation of structure and magnetism

The fundamental magnetic properties of a cluster are strongly dependent on the nature of the metal ions used to form the complex, the distances between the ions, and the angles subtended at the ligand atoms which link the metal centres together.

Inter-atomic geometry can be altered by applying pressures of 1-10 GPa using a diamond anvil cell. The structures of the molecules can be determined by X-ray crystallography, and their magnetic properties measured using a SQUID-MS. We can therefore probe, in a very controlled and systematic way, the effect that changes in geometry have on structural and magnetic properties of a given complex.

Very few publications have been made on combined studies, especially on single-molecules magnets. Tancharakorn *et al.*[46] have reported a decrease in the J value with pressure on $[(CH_3)_4N][MnCl_3]$. They also notice phase changes in the magnetic measurements that could be correlated by the structural phase changes. Suzuki *et al.*[47] induced a transition from anti-ferromagnetic interactions to ferromagnetic interactions by using pressure. The transition occurred at 1.2 GPa on $[Cu_2(OH)_3(CH_3COO)] \cdot H_2O$.

We have chosen to study Mn_{12} clusters, chains and iron oxo-bridged dimers:

1. molecular clusters: $[Mn_{12}O_{12}(O_2CCH_2Bu^t)_{16}(H_2O)_4]$ and $[Mn_{12}O_{12}(MeCO_2)_{16}(H_2O)_4]$;
2. chain structures: $[Gd(PhCOO)_3(DMF)]_n$ and $[VO(salpropane)]_n$;
3. Iron chloride and salen complexes: $[N(PhCH_2)(CH_2CH_3)_3]_2[Fe_2OCl_6]$, $[N(CH_3)_4]_2[Fe_2OCl_6] \cdot CH_3CN$ and $[Fe(salen)Cl]_2$.

Some have simple structures like the dimers or more complicated structures with low symmetry like the $[Mn_{12}O_{12}(O_2CCH_2Bu^t)_{16}(H_2O)_4] \cdot CH_2Cl_2 \cdot MeNO_2$ complex. Some have simple magnetic properties like the dimers or much more complicated properties for the SMMs. We will conclude at the end of thesis on what is possible given the technical limitations we faced and any evidence on a possible correlation will be discussed.

Chapter 2

Experimental section

2.1 High pressure cells

Pressure is Force per unit Area ($P = F/A$). It is however difficult to induce high pressure and often requires huge mechanical parts compared to the size of the sample chamber. There are two different kinds of pressure: static pressure and shock compression.

Shock compression can achieve a higher pressure, over 1000 GPa but only for a short time. This is conventially produced by dynamic anvil cells, explosives, gas guns, pulsed power (magnetic pulsed) or lasers.[48]

Static pressure is achieve by using pressure cells. They can be cylinder, belts, Drickramer, Bidgman, anvil, multiple anvil cells and finally the diamond anvil cell.[49] The piston cylinder pressure cell perhaps is the simplest cell which is compatible with the physical constraints of the SQUID-MS (10 mm diameter chamber). The cell used for the magnetic measurements is described in section 2.1.2. Diamond anvil cells (DAC) have been used for more than 50 years and are now widely available. Diamond Anvil cells have been used for all the high pressure crystallography measurements and are described in section 2.1.1.

2.1.1 Diamond anvil cells or DAC (X-ray)

The diamond anvil cell was developed around 50 years ago by Charlie Weir.[50] The cell used during my PhD is a modified Merrill–Bassett miniature diamond anvil cell. Conventional Merril-Basset DAC currently utilise beryllium for the backing seat which produces a powder pattern on the detector, hiding sample reflections in some places (Figure 2.1). Beryllium is also less stable to some organic acids, oxides, nitrides and is toxic. A new diamond cut from Boehler–Almax industries allows the use of a tungsten carbide (WC) backing seat with no decrease in the opening angle[51] (Figure 2.2). The sample is loaded with a hydrostatic medium. This is conventionally a liquid which maintains its phase across the pressure regime under study and which does not interact or react with the crystal sample. Depending on the medium fluid, the cell can reach between 2.5 GPa (parafin) to 10 GPa (methanol/ethanol/water mixture). The pressure cell is attached to a stainless steel table (usually with superglue or some other adhesive) which has a vertical pin that can fit into a standard goniometer head (Figure 2.3).

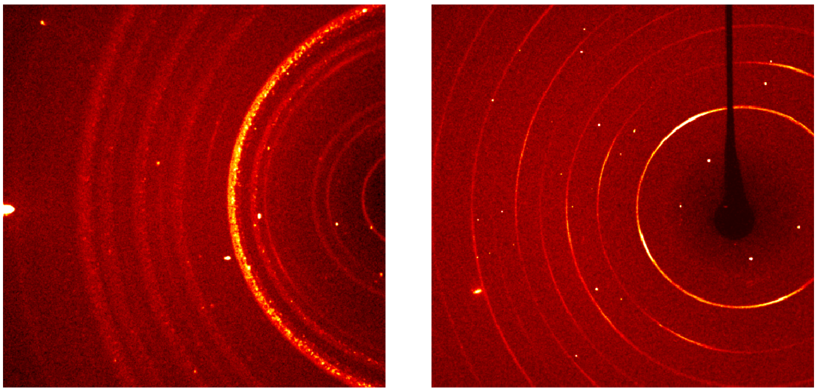

Figure 2.1: CCD images from complex $[Mn_2Dy_2O_2(O_2CCMe_3)_8(HOCCMe_3)_2(MeOH)_2]$. On the left: 60 s exposure on a lab source with a Be backing-seat diamond Anvil cell. On the right: 1 s exposure on a synchrotron source with a WC backing-seat cell.

Note the presence of very strong reflections on the edge of the 60 second lab exposure. This reflection is more than likely attributable to a diamond reflection.

The beryllium powder rings are made many times worse under synchrotron conditions as with the low divergence and high intensity, all the rings become many times stronger with a significant degree of texture, which is not resolvable under lab conditions. This makes it even harder to deconvolute overlapping sample and beryllium reflections.

In order to record the pressure of the sample within the cell, conventionally a small ruby chip is also mounted with the sample. The ruby diffraction pattern is often very weak and if present can be readily deconvoluted.

The Raman R1 and R2 fluorescence peaks can be used to track the pressure within the cell.[52]

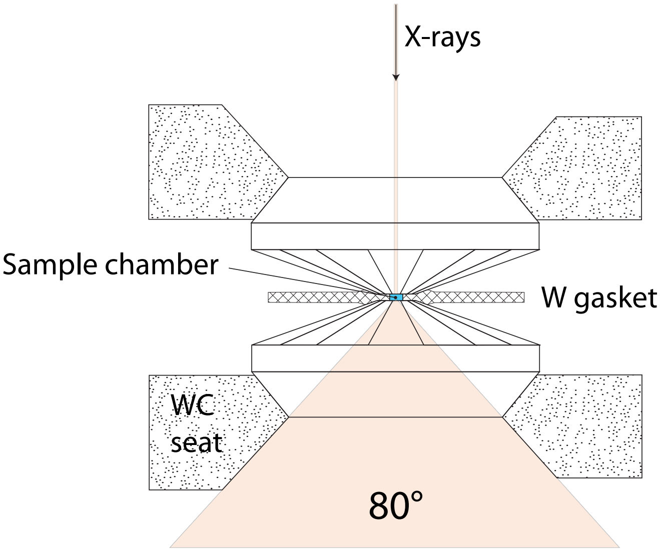

Figure 2.2: Scheme of the Be free diamond anvil cell. Not to scale.

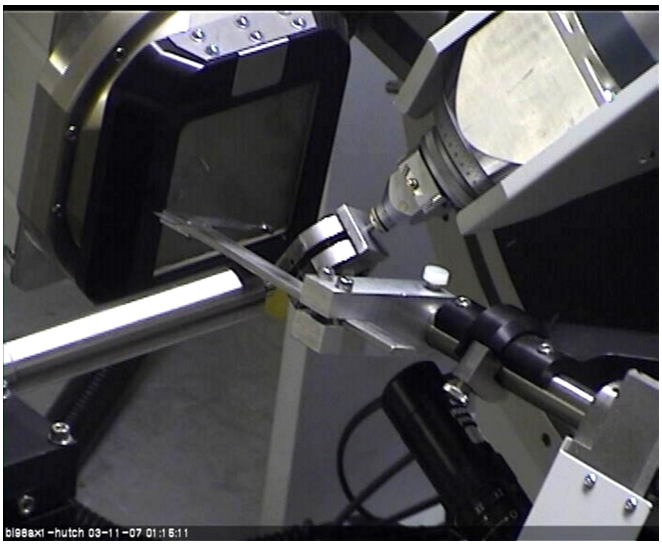

Figure 2.3: DAC in place on the Station 9.8 diffractometer in SRS, Daresbury.

2.1.2 Piston cylinder pressure cell (magnetic measurements)

High-pressure experiments were carried out with a piston cylinder pressure cell made by the Centre for Science at Extreme Conditions (CSEC) at the university of Edinburgh (unpublished). Two different cells were used: one is made from a CuBe alloy (BERYLCO-25) and can reach a maximum pressure of 1.4 GPa at ambient temperature. The second cell is made with two different alloys: the outer body is made of a CuBe alloy and the inner body is made of a CrNiAl alloy. Both cells have a 8.8 mm diameter in order to fit into the MPMS. The CrNiAl alloy produces a higher background than the CuBe alloy but can reach a higher pressure. The maximum pressure for the NiCrAl cell at ambient temperature is 2 GPa. Both cells consist of (Figure 2.4 and 2.5):

- a 21 mm in body length (6);
- a bottom screw with a backup piston made of zirconia for the CuBe cell or NiCrAl for the NiCrAl cell (1);
- a bottom zirconia pusher (2);
- a Teflon® capsule which contains the sample plus a fluid medium (3). The capsule is 5 mm long with a diameter of 2.5 mm. The sample is loaded with Daphne 7373 (IDEMITSU-ILS) oil[53] in order to have a hydrostatic pressure;
- a top zirconia pusher (4);
- a top screw with a backup piston made of zirconia for the CuBe cell or NiCrAl for the NiCrAl cell (5);
- two copper rings to seal the sample space (Figure 2.5).

Pressure is applied by using a manual hydraulic press, an external pressure sensor between the press and the cell is used to measure the pressure applied to the pressure cell. The pressure is transmitted via a piston through the top screw, the piston is then removed and the cell attached to the rod via the top screw. A chip of lead or tin placed in the Teflon® capsule with the sample is used as a pressure calibrant in a similar manner to the use of ruby in the diamond anvil cell. The superconducting transition of the calibrant was used to determine the pressure inside the cell[54] at low temperature. A drop in pressure of up to 0.5 GPa is usually observed between ambient and low temperature. The evolution of pressure as a function of temperature for the lead is reported in Equation 2.1 and in Equation 2.2 for tin. T_c is the superconducting transition of the given metal, P is the associated pressure.

$$T_c(P) = T_c(0) - (0.365 \pm 0.003)P \tag{2.1}$$

$$T_c(P) = T_c(0) - (0.4823 \pm 0.002)P + (0.0207 \pm 0.0005)P^2 \tag{2.2}$$

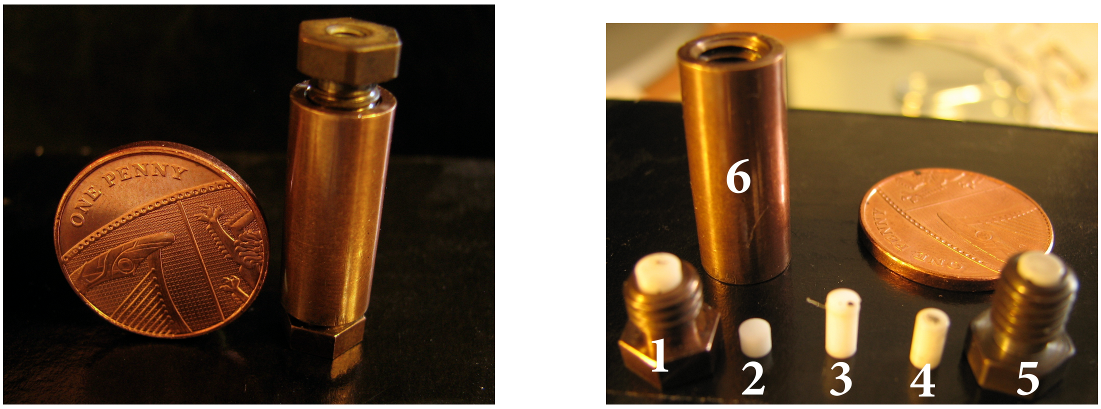

Figure 2.4: Components of the CuBe pressure cell

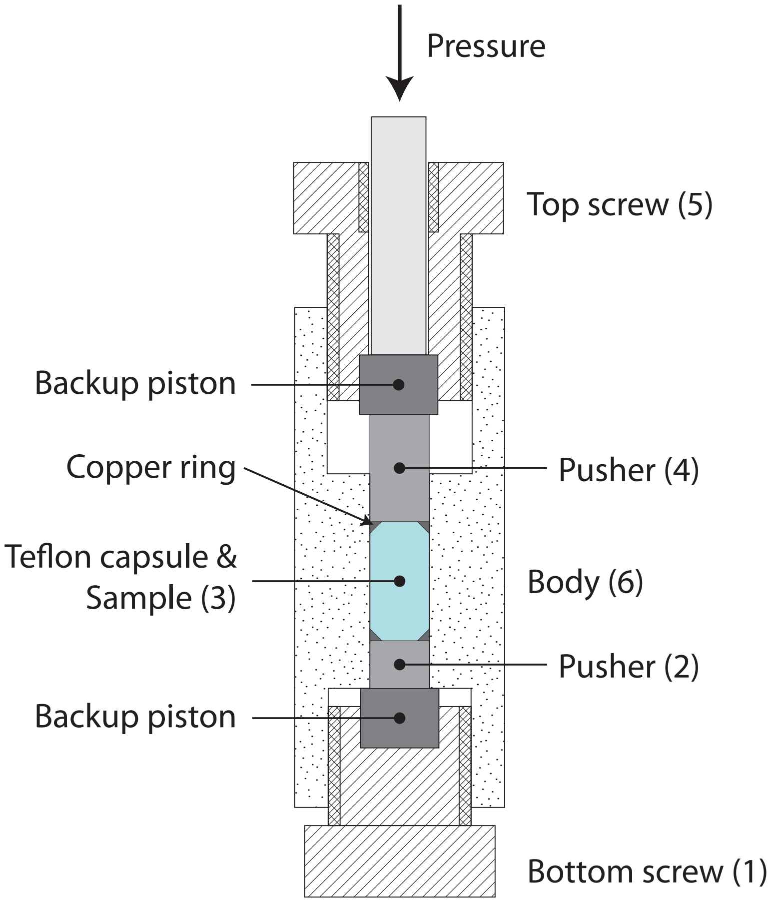

Figure 2.5: Schematic of the CuBe piston cylinder pressure cell.

2.2 Crystallography

2.2.1 General Procedures

High-pressure experiments were carried out with a modified Merrill-Bassett diamond anvil cell equipped with 600 μm culet diamonds and a tungsten gasket.[51] The sample and a chip of ruby (as a pressure calibrant) were loaded into the DAC with a 4:1 mixture of methanol and ethanol or 1:1 mixture of pentane and isopentane or parafin as a hydrostatic medium. The ruby fluorescence method was utilised to measure the pressure.[52]

2.2.2 Data Collection, Reduction and Refinement

A sphere of data was collected on a single crystal at ambient temperature and pressure in order to provide data for comparison with the high pressure studies, which were also performed at ambient temperature (see below). Diffraction data were collected on a single crystal on a Bruker SMART APEX diffractometer with graphite-monochromated Mo-Kα radiation (λ =0.71073 Å). These data were integrated using the program SAINT,[55] while the absorption correction was carried out using the program SADABS.[56] Refinement was carried out against $|F|^2$ using all data[57] starting from the ambient temperature coordinates.

High pressure diffraction data were collected with synchrotron radiation on a Bruker APEX II diffractometer at the STFC Daresbury Laboratory on Station 9.8 (λ =0.4767 Å). The data collection strategy was ω-scans in eight settings of 2θ and ϕ with a frame and step size of one second and 0.3° respectively. This data collection strategy was based on that described previously.[58] The data were integrated using the program SAINT using "dynamic masks" to avoid integration of regions of the detector shaded by the body of the pressure cell.[58] Absorption corrections for the DAC and sample were carried out with the programs SHADE[59] and SADABS respectively.

Refinements were carried out against $|F|^2$ using all data (CRYSTALS). Because of the low completeness of the data-sets, all 1,2 and 1,3 distances in the ligands were restrained to the values observed from our ambient pressure structure. All torsion angles and metal to ligand distances were refined freely. Hydrogen atoms attached to carbon were placed geometrically and not refined.

All C, N and O atoms were refined with isotropic thermal parameters, while metallic centres were refined anisotropically. This parametrization strategy was dictated by the quality of the data collected.

Software for Structure Analysis

Crystal structures were visualized using the programs DIAMOND[60] and MERCURY.[61] Analyses were carried out using PLATON,[62] as incorporated in the WIN-GX suite.[63] Searches of the Cambridge Database[38,64] were performed with the program CONQUEST and version 5.29 of the database with updates up to January 2008.

2.3 Magnetic measurements

The data were measured using a Quantum Design MPMS XL SQUID magnetometer. High pressure measurements were made in the piston cylinder cell described in Section 2.1.2. For AC susceptibility, using zero DC field with 3 G AC drive field and temperature scans from about 7 K to 1.8 K at different fixed frequencies between 0.1 Hz and 50 Hz were carried out. Hysteresis loops were measured on the MPMS at 2 K between -5 T and 5 T with a minimum field step of 0.02 T between -1.4 T and 0.8 T (Appendix A).

$[Mn_{12}O_{12}(MeCO_2)_{16}(H_2O)_4] \cdot 2\,CH_3COOH \cdot 4\,H_2O$ (**1**) has been studied using a NiCrAl pressure cell. Five manually oriented single crystals of complex **1** (weight: 5.89 mg) were placed in the Teflon® capsule with the long easy axis of the crystal aligned parallel to the long axis of the Teflon® capsule. Because of the shape of the capsule, nothing was necessary to keep the crystals in a vertical position. Crystals had a parallelepiped shape, the length was about 2 mm and the width about 0.5 mm. Further alignment was done by field cooling the cell in a field of 5 T from ambient temperature to 10 K. Below 150 K, the oil used as a pressure medium is frozen and the crystals retain their orientation when the field is switched off. A powder sample of **1** (weight: 11.40 mg) as also been measured at high pressure in a NiCrAl cell by Javier Sanchez Benitez in the PPMS at Edinburgh.

Several single crystals of $[Mn_{12}O_{12}(O_2CCH_2Bu^t)_{16}(H_2O)_4] \cdot MeNO_2 \cdot CH_2Cl_2$ (**2a**) were placed in the Teflon® capsule (weight: 4.84 mg). Because of the "block" shape of the crystals, no manual orientation could be carried out. However, the crystals have been magnetically aligned by using field cooling at 5 T from ambient temperature to 10 K. A ground sample would have been better but the sample was not stable during the grinding, probably the complex changes structure when solvent is lost. Soler *et al.*[26] reported a conversion from fast relaxing (FR) species to slow relaxing (SR) species with solvent loss on the same complex.

The pressure cell induces a background signal which needs to be treated before analysing the data. Depending on the experiment, the background can be expressed as a simple mathematical function, see Section 2.3.1 or needs to be suppressed experimentally, see Section 2.3.2.

2.3.1 AC susceptibility

In AC measurements, a small AC drive field is superimposed on the DC field, causing a time-dependent moment in the sample. At low frequencies, the magnetic moment of the sample follows the $M(H)$ curve that would be measured in a DC experiment. At higher frequencies the magnetisation of the sample may lag behind the drive field, an effect that is measured by the magnetometer. Thus, the AC susceptibility measurements leads to two signals: the magnitude of the susceptibility m and the phase shift ϕ. The real component m' is defined as: $m' = m\cos(\phi)$ and the imaginary component of the out of phase AC susceptibility: $m'' = m\sin(\phi)$.[65]

Frequencies higher than 200 Hz are unusable with the pressure cell because the background from the cell hides any potential peaks in the imaginary component of the out of phase AC susceptibility. For frequencies between 25 Hz and 200 Hz, peaks in the out phase AC susceptibility are visible but unusable due to a non linear baseline (see Figure 2.6) which is essential to have good fit of the data. Below 25 Hz the background is constant and has been fitted as a constant at the same time as the data.

For single-molecule magnets, out of phase AC susceptibility curves are usually fitted by using Lorentzian curves. We have discovered that the out of phase AC susceptibility curves from the Mn_{12} analogues, including the Mn_{12} acetate, cannot be fitted with Lorentzian curves (Figure 2.7), especially at high pressure (Figure 2.8).

The experimental data profile lies between a Lorentzian and Gaussian model. On one hand, the Gaussian sum fit of the low temperature (LT) peak plus the high temperature peak (HT) results in an underestimated maximum for the HT peak fit and the LT peak fit is completely misplaced. A fit with a Gaussian curve of the HT peak alone between

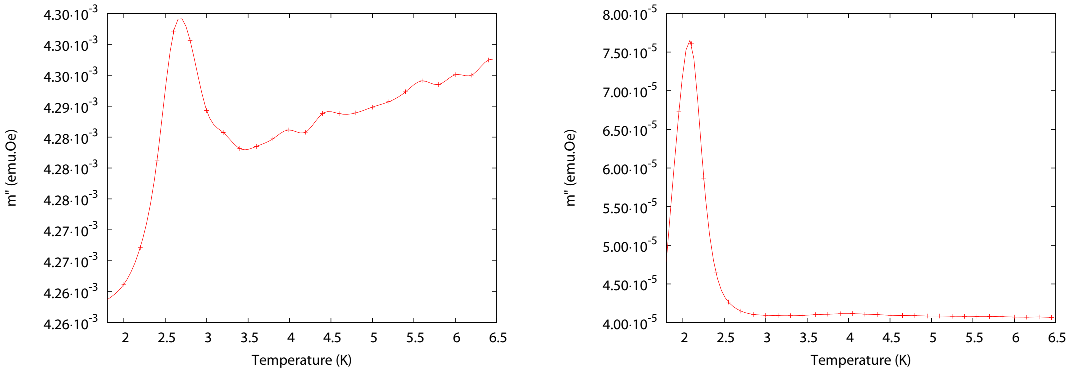

Figure 2.6: Out of phase component of the AC susceptibility of **2a**. Illustration of the non-linear baseline when using the CuBe pressure cell at ambient pressure. DC field = 0 Oe, AC drive field = 3 Oe. On the left: $\nu = 99.95$ Hz. On the right $\nu = 1.00$ Hz. The line is a guide for the eye.

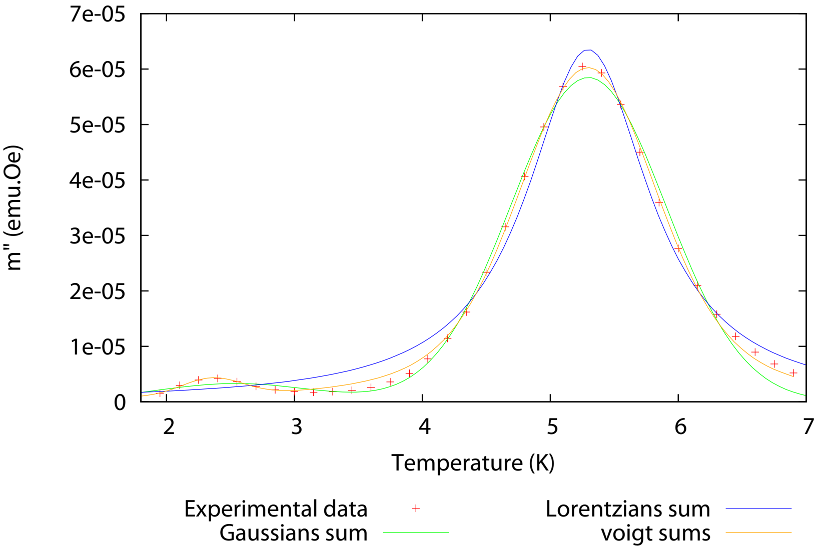

Figure 2.7: Out of phase component of the AC susceptibility of **1** at ambient pressure in the straw on five manually aligned single crystals at 25 Hz. Illustration of different models of fitting.

3.4 K and 7 K shows exactly the same result. On the other hand, a sum of two Lorentzians could not fit the two peaks at all, only the HT peak was more or less fitted. The result is the same if only the HT peak is fitted. The fit result of the HT peak with a Lorentzian shows an overestimated maximum (Figure 2.7).

At high pressure on complex **1** when using one curve to fit the HT peak the position of the peak is misplaced (Figure 2.8). Cornia *et al.*[66] reported that the Mn_{12} acetate complex could exist in different isomers due to the disorder of the acetic acid molecule. There is a possibility that the HT peak in our data reveals such isomers. The number of Lorentzian curves has been increased in order to accommodate the presence of different isomers in our data. With four curves for the HT peak the fit has improved (Figure 2.8). But it is difficult to assign such change to the isomers as we also increase the number of parameters which automatically improves the quality of the fit.

We can also increase dramatically the number of curves by using nine Lorentzians curves for the fit of the HT peak in order to check another hypothesis, a Gaussian distribution of Lorentzian curves (Figure 2.9). The figure has been made in two steps, the first step is the fit of the HT peak with nine Lorentzian curves. Such number of curves give us twenty seven parameters plus three parameters for the LT peak compared to the seventy-five data points we have. In this case, starting the fit from random values gives every result imaginably possible. The Lorentzian curves have been manually placed on a Gaussian curve and then the parameters have been allowed to relax. The result is the blue curves in Figure 2.9 and the corresponding sum is the green curve. The second step is the fit of a Gaussian against the peak position of the Lorentzian Curves as represented with a black curve in Figure 2.9. Figure 2.9 reveals a good correlation between the blue and the black curves which could mean that the peak is only an average of a distribution of species. Such a normal distribution can be due to random disorders (distribution of environments) like defects, impurities or dislocations.[67,68] However it does not correlate with the hypothesis of isomers[66,69] as we should see discrete curves and not a distribution of curves. Hill *et al.*[70] also noticed a broadening mechanism (g, D, and E strain) such as asymmetric line-shapes and a small, but measurable m_s dependence of the line-widths but did not explain it.

This behaviour has been encountered on the Mn_{12} acetate as described in Figure 2.9 and on **2a**, both on single crystals and powder data, at ambient pressure and higher pressure. As a result, we choose to fit all the out of phase AC susceptibility results in this chapter using a Gaussian distribution of Lorentzians. Such a distribution can be modeled as a Voigt profile.

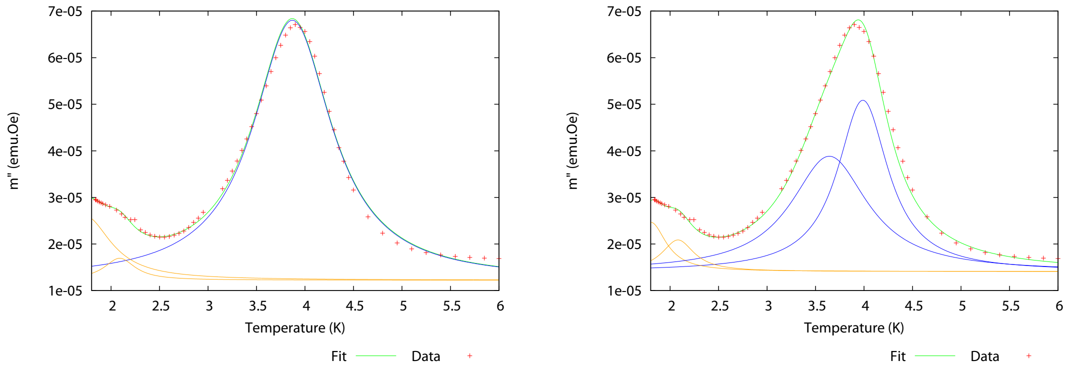

(a) 1 Lorentzian

(b) 2 Lorentzians

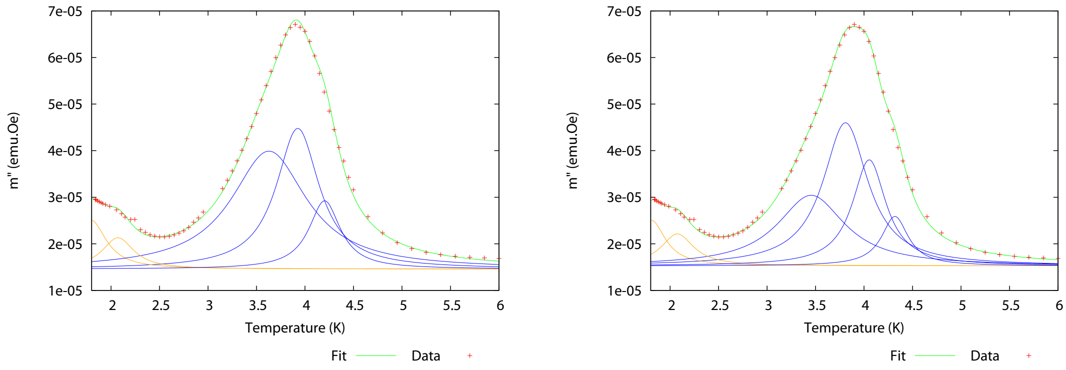

(c) 3 Lorentzians

(d) 4 Lorentzians

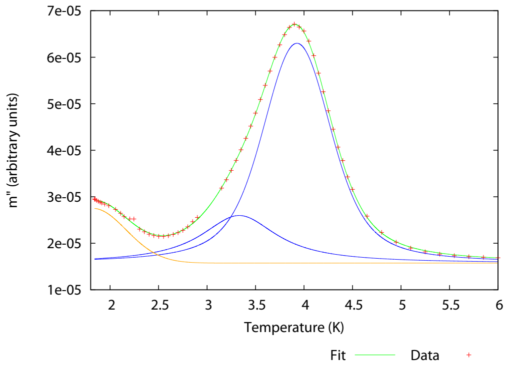

(e) Voigt profile

Figure 2.8: Fits of the out of phase component of the AC susceptibility of **1** at 1.45 GPa in the NiCrAl pressure cell on five manually aligned single crystals at 0.5 Hz. Illustration of different models of fitting. The number of curves refers to the high temperature (HT) peak only.

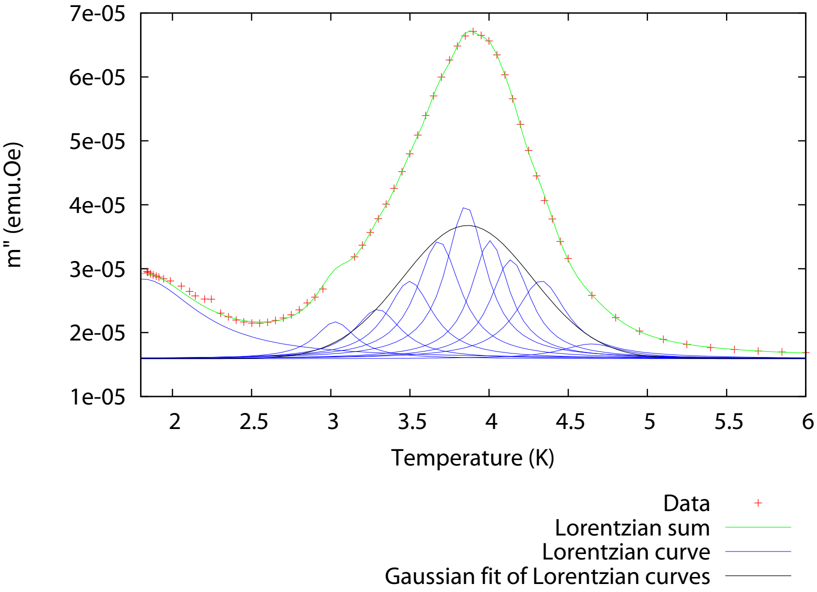

Figure 2.9: Out of phase component of the AC susceptibility of **1** at 1.45 GPa at 0.5 Hz.

Fityk[71] has been used to fit the m'' vs T AC data. This software can fit the sum of Voigt profiles, Gaussian and Lorentzian curves. Fitting the sum is more accurate when peaks are overlapping. Fityk uses the Voigt definition described by Wells[72]. The definition of the Voigt profile is described in equation 2.3. a_0 is the height, a_1 is the center, a_2 is proportional to the Gaussian width and a_3 is proportional to the ratio of Lorentzian and Gaussian widths.

$$y = a_0 \frac{\displaystyle\int_{-\infty}^{+\infty} \frac{\exp(-x^2)}{a_3^2 + \left(\frac{t-a_1}{a_2} - x\right)^2} \mathrm{d}x}{\displaystyle\int_{-\infty}^{+\infty} \frac{\exp(-t^2)}{a_3^2 + x^2} \mathrm{d}x} \tag{2.3}$$

The general equation for the out of phase AC susceptibility fitting as a function of the temperature t is therefore for n peaks:

$$m'' = C + \sum_{1\leqslant i\leqslant n} a_{i,0} \frac{\displaystyle\int_{-\infty}^{+\infty} \frac{\exp(-x^2)}{a_{i,3}^2 + \left(\frac{t-a_{i,1}}{a_{i,2}} - x\right)^2} \mathrm{d}x}{\displaystyle\int_{-\infty}^{+\infty} \frac{\exp(-x^2)}{a_{i,3}^2 + x^2} \mathrm{d}x} \tag{2.4}$$

a parameters have been described previously, C is a constant to model the background of the pressure cell.

The energy barrier to reorientation of the magnetisation ($\Delta E/k_B$) has been calculated from the Arrhenius law (equation 2.5) by plotting the natural logarithm of the relaxation time as a function of the inverse temperature. τ is given by $1/(2\pi\nu)$, with ν being the frequency of the oscillating AC field. The slope of the best fit is the energy barrier in Kelvin and the intersection with the y-axis gives the relaxation time τ_0. Because we are using a Voigt profile for the out of phase AC susceptibility peaks, the energy barrier results are only for the major species. It is possible from the fit to get the Gaussian part of the Voigt profile and use it to calculate the distribution of the energy barrier resulting from the distribution of species. Due to the complexity of such calculation, it has not been done but Park *et al.*[73] has reported such a distribution from EPR measurements.

$$\tau = \tau_0 \exp\left(\frac{\Delta E}{k_B \cdot T}\right) \tag{2.5}$$

2.3.2 Hysteresis loop

Hysteresis loops were collected with a 40 hour sequence and a maximum resolution of 0.02 T step at 2 K (Appendix A). Because the pressure cell has a background which cannot be estimated as a simple mathematical function, it needs to be removed numerically.

Measuring the background of the cell alone is very difficult: the cell is an assembly of different parts which can result in a different background simply by unloading and loading the cell. In order to measure the cell background, the cell would need to be centred in the SQUID magneto-susceptometer which is very difficult because the cell is designed to have a low signal response and the cell gives a response on its whole length.

Instead, an estimation of the background was calculated with a measurement from the sample itself and from the sample inside the cell at ambient pressure. The subtraction of the two measurements is used as a background which includes the cell, the medium and the Teflon® capsule. The signal from the sample at different pressures was then calculated from the measurement of the sample inside the cell at a given pressure and then subtraction of the background as calculated above (see Equation 2.6). As a result, the signal from the sample will result from the calculation from three measurements which results in a higher standard deviation, about three times more important than a measurement outside the pressure cell.

$$\begin{aligned} M_{\text{sample}}^{\text{x GPa}} = M_{\text{sample + cell}}^{\text{x GPa}} - \left(M_{\text{sample + cell}}^{\text{ambient pressure}} - M_{\text{sample}}^{\text{ambient pressure}}\right) \pm \\ \left(\Delta M_{\text{sample + cell}}^{\text{x GPa}} + \Delta M_{\text{sample + cell}}^{\text{ambient pressure}} + \Delta M_{\text{sample}}^{\text{ambient pressure}}\right) \end{aligned} \tag{2.6}$$

After removing the background of the cell, only the signal from the sample remains. For single-molecule magnets, one way to show the hysteresis loop is to plot the numerical differentiation of the data to highlight the quantum tunnelling steps (see Figure 2.10 for an example on **1** at 1.45 GPa). Due to the accumulation of errors during the background removal, the result is not useable.

The main reason for these poor data is the way the derivative is calculated. The derivative of each data point has been assumed to be the slope of the straight line between the previous and next data point (finite difference formula). In this case, the standard deviation of the slope can be important. Higher orders can be used to estimate the derivative like the five-point stencil or nine-point stencil methods in order to reduce the standard deviation and have a better estimate of the slope, but the number of points is still statistically low. It is important to note that each measurement point suffers from random errors, these errors are not important but through the calculation they can become very important especially if a low number of data points is involved. Random errors follow a Gaussian distribution centred on zero, the average is therefore zero. As the fitting of the curve has been done on hundreds of data points, the impact of random errors has been reduced. That is why the exact derivative of the fit gives much better results than any numeric derivative. The result of the derivative from both the experimental data (finite difference formula) and the fitting of the hysteresis loop of **1** at 1.45 GPa is shown in Figure 2.10.

Since it is difficult to theoretically express the magnetisation curves, a phenomenological equation has been used for each step i in the hysteresis loop from Takeda *et al.*[27]:

$$M_i = M_s^i \frac{\left[1 - \exp\left(-2A_i\left(H \pm H_0^i\right)\right)\right]}{\left[1 + \exp\left(-2A_i\left(H \pm H_0^i\right)\right)\right]} \tag{2.7}$$

The curve has no physical meaning and only fits the shape of the step. M_s^i is the saturation magnetisation for each step, H_0^i the coercive field for the step and A_i is a parameter fitting the slope during the step. The whole hysteresis loop is composed of two symmetric curves: one curve from -5 T to 5 T and its mirror image from 5 T to -5 T. Each part is then fitted with a sum of equation 2.7. In this case, the different H_i^0 parameters are

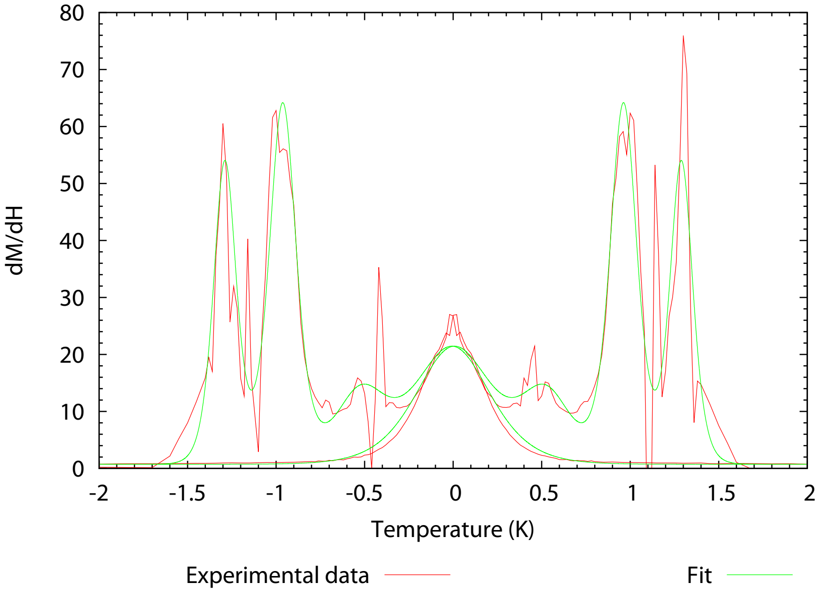

Figure 2.10: Derivative of both the experimental data and the fit of the hysteresis loop of **1** at 1.45 GPa.

independent. In order to get a better estimate of the anisotropy, we can use the axial zero field splitting Hamiltonian to first order:[74]

$$\mathcal{H} = D\hat{\mathbf{S}}_z^2 + g\mu_B\hat{\mathbf{S}} \cdot H_z \tag{2.8}$$

where D represents the axial zero field splitting parameter, μ_B is the Bohr magneton, $\hat{\mathbf{S}}_z$ the easy axis spin operator and H_z the applied field. If the field is applied along the easy axis, the eigenstates of this Hamiltonian are $|S, m\rangle$, where m is the magnetic quantum number. QTM occurs when the states $|S, m\rangle$ $(m < 0)$ coincide in energy with the states $|S, m'\rangle$ $(m' > 0)$ at the field of:

$$H_{m,m'} = \frac{D\,(m + m')\,k_B}{g\mu_B} \tag{2.9}$$

Equation 2.7 and 2.9 have been combined in equation 2.10 which has been used in the algorithm for the fitting. D is the axial zero field splitting parameter in Kelvin, k_B is the Boltzmann constant, μ_B is the Bohr magneton and g is the g-factor. The fitting parameters are D, M_s^i, A_i and B. Fixed parameters are $m_i + m_i'$, zero for the first step, -1 for the second and so on. The g-factor has been fixed at 1.9 for all pressures.[11,74–76] The term B in Equation 2.10 is linear to the external field, H. This accounts for the fact that the Mn_{12}

cluster exhibits a uni-axial magnetic anisotropy and the field is not completely parallel to the easy axis of all molecules due to the mis-alignment of the crystals in the cell.

$$M = B \cdot H + \sum_{1 \leqslant i \leqslant n} M_s^i \cdot \frac{\left[1 - \exp\left(-2A_i\left(H \pm \frac{D\left(m_i + m_i'\right)}{g\mu_B}\right)\right)\right]}{\left[1 + \exp\left(-2A_i\left(H \pm \frac{D\left(m_i + m_i'\right)}{g\mu_B}\right)\right)\right]} \tag{2.10}$$

The energy barrier can be calculated from the anisotropy with:

$$\Delta E = S^2 \left|D\right| \tag{2.11}$$

However, equation 2.10 cannnot be used for complex **1** as higher order terms have not been included, resulting in an incorrect estimation of the steps. In **1**, the space between the steps is no longer constant. As a result, only the simple version of the equation has been used, where the coercive field of each step has been considered to be independent from each other:

$$M = B \cdot H + \sum_{1 \leqslant i \leqslant n} M_s^i \cdot \frac{\left[1 - \exp\left(-2A_i\left(H \pm H_0^i\right)\right)\right]}{\left[1 + \exp\left(-2A_i\left(H \pm H_0^i\right)\right)\right]} \tag{2.12}$$

A python routine to fit the curve has been written using the openopt[*] module. Instead of using the two symmetric equations, one for each part of the curve, only one equation has been used with the data points of the first part of the curve (-5 T to 5 T) and the symmetric $(-H, -M)$ of the (H, M) data points of the second part (from 5 T to -5 T).

Constraints on the parameters have also been used in order to avoid divergence during the fitting. The slope of the loop A_i has been restrained to values greater than 3 or 4. This limit has been found on a trial and error basis. The algorithm sometimes tends to attribute a value near zero which leads to some problems. If the contribution of a particular step is null, the M_s^i parameter should tend to zero instead. The M_s^i has been constrained to be positive. The D parameter (for equation 2.10) has sometimes been constrained between plausible values for the anisotropy found in these kind of complexes. After the fit, parameters have been checked against their constraints. As the constraints are only used to avoid divergence they should not be reached by the end of the fitting. An exception has been made for the slope which sometimes hits the limit imposed by the

---

[*] `http://openopt.org`

constraints, especially on small steps, where the curve is difficult to estimate. It has no effect on the other parameters and thus on the result of the fit. No restraints have been used on the B parameter.

Chapter 3

Single-molecule magnets

Mn_{12} acetate analogues are the most studied SMMs with a lot of literature material.[11,13–15] They have a strong magnetic signal response thus a high signal/noise ratio. Synthesis of the Mn_{12} acetate is easy and all analogues can be made from the $[Mn_{12}O_{12}(MeCO_2)_{16}(H_2O)_4] \cdot 2\,CH_3COOH \cdot 4\,H_2O$ (**1**) complex by ligand substitution.[11,23–27] Mn_{12} analogues have been chosen for all these reasons. Among all the available analogues, two have been chosen in particular: the historical Mn_{12} acetate[12] as a reference and the "horizontal" elongated Jahn-Teller analogue $[Mn_{12}O_{12}(O_2CCH_2Bu^t)_{16}(H_2O)_4] \cdot MeNO_2 \cdot CH_2Cl_2$ (**2a**)[26] (Figure 3.1).

Both magnetic measurements and single crystal X-ray diffraction under pressure have been done on **2a**. Only magnetic magnetic measurements have been done on **1**. The magnetic study includes out of phase AC susceptibility measurements (below 10 K) and hysteresis loops at 2 K.

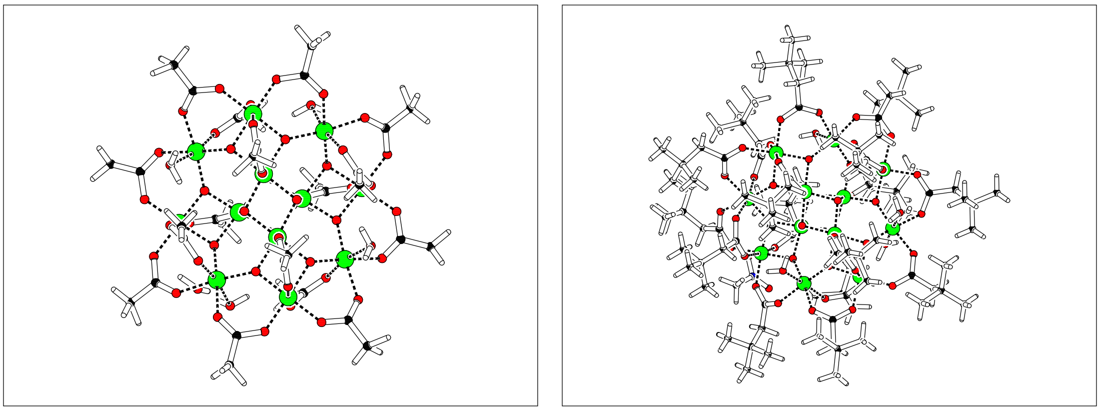

(a) $[Mn_{12}O_{12}(MeCO_2)_{16}(H_2O)_4] \cdot 2\,CH_3COOH \cdot 4\,H_2O$ (**1**)

(b) $[Mn_{12}O_{12}(O_2CCH_2Bu^t)_{16}(H_2O)_4] \cdot MeNO_2 \cdot CH_2Cl_2$ (**2a**)

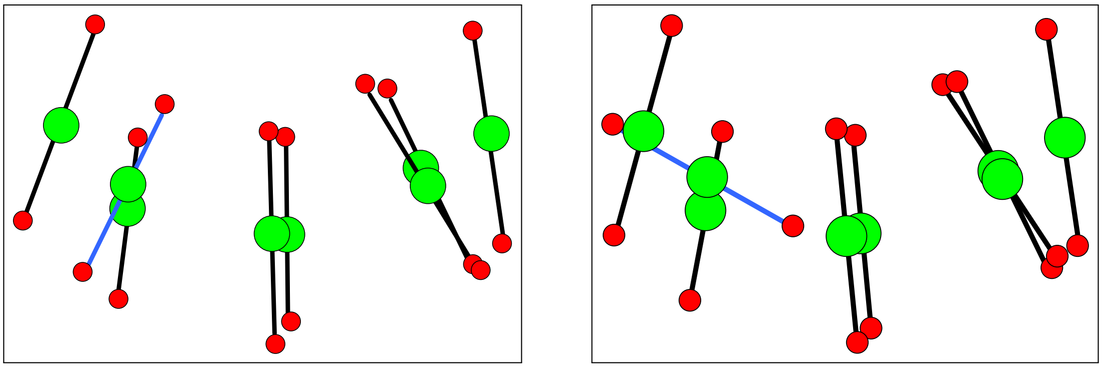

(c) “Vertical” elongated Jahn-Teller configuration of **1**

(d) “Horizontal” elongated Jahn-Teller configuration of **2a**

Figure 3.1: Mn_{12} analogues with their elongated Jahn-Teller axis orientation. In blue the tilted axis, Mn are in green, O in red, C in black and H in white.

3.1 $[\mathrm{Mn_{12}O_{12}(O_2CCH_2Bu^t)_{16}(H_2O)_4}] \cdot \mathrm{MeNO_2} \cdot \mathrm{CH_2Cl_2}$

3.1.1 Synthesis

$[\mathrm{Mn_{12}O_{12}(O_2CCH_2Bu^t)_{16}(H_2O)_4}] \cdot \mathrm{MeNO_2} \cdot \mathrm{CH_2Cl_2}$ (**2a**) has been prepared by following the Soler *et al.*[26] synthesis. A slurry of $[\mathrm{Mn_{12}O_{12}(MeCO_2)_{16}(H_2O)_4}] \cdot 2\,\mathrm{CH_3COOH} \cdot 4\,\mathrm{H_2O}$ (**1**) (see Section 3.2.1) (0.4 mmol, 800 mg) in toluene (40 mL) was treated with an excess of tertbutylacetic acid (7.8 mmol, 1 mL). The mixture was concentrated in vacuo, with a temperature bath around 50°, to remove acetic acid as the toluene azeotrope. As the solvent volume was reduced, the black solid slowly dissolved. When almost all the toluene had been removed, more toluene (30 mL) was added and removed by evaporation, and the process repeated twice. The resulting oil was dissolved in toluene, and treated with a further amount of tertbutylacetic acid and the entire process repeated. After the final evaporation, the resulting oil was dissolved in a minimum amount of dichloromethane in order to make handling easier (the oil is very sticky).

A small amount of the previous dichloromethane solution, around 10 mg, is dissolved in 50 mL of a $\mathrm{CH_2Cl_2/MeNO_2}$ solution (50/50 in volume). The solution is then filtered and left to evaporate slowly in a partially-closed beaker. Crystals of complex $[\mathrm{Mn_{12}O_{12}}\text{-}\mathrm{(O_2CCH_2Bu^t)_{16}(H_2O)_4}] \cdot \mathrm{MeNO_2} \cdot \mathrm{CH_2Cl_2}$ (**2a**) appear within 24 hours or a week depending on the concentration. Crystals are fragile, they probably lose solvent which could result on the out of phase AC susceptibility m'' response a shift from a LT species to a HT species as reported by Soler *et al.*[26].

A small amount of the previous dichloromethane solution, around 10 mg, is dissolved in a minimum amount of warm MeCN. Depending on the amount of dichloromethane used to make the mother solution, adding a small amount of dichloromethane can help to solubilise the product. The solution is then slowly cooled and left for crystallisation. Crystals of $[\mathrm{Mn_{12}O_{12}(O_2CCH_2Bu^t)_{16}(H_2O)_4}] \cdot \mathrm{CH_2Cl_2} \cdot \mathrm{MeCN}$ (**2b**) appears within an hour or a day. No further measurements were carried out on **2b**.

3.1.2 Data Collection

Four datasets of $[\mathrm{Mn_{12}O_{12}(O_2CCH_2Bu^t)_{16}(H_2O)_4}] \cdot \mathrm{MeNO_2} \cdot \mathrm{CH_2Cl_2}$ (**2a**) from ambient pressure to 1.44 GPa have been collected (Table 3.1). The datasets from ambient pressure to 1.12 GPa were collected in the CuBe pressure cell. The last dataset at 1.44 GPa was collected in the NiCrAl pressure cell as the maximum pressure of the CuBe cell had been reached. The sample has been pseudo-aligned by field cooling at 5 T from ambient to 10 K. T_c is the temperature of the superconducting transition of lead used as a pressure calibrant in the pressure cell.

Table 3.1: Dataset of pseudo-aligned crystals of complex **2a** from ambient pressure to 1.44 GPa

Dataset	T_c (Pb) K	Pressure GPa
HP0 (CuBe cell)	7.20	0
HP1 (CuBe cell)	7.03	0.47
HP2 (CuBe cell)	6.90	0.82
HP3 (CuBe cell)	6.79	1.12
HP4 (NiCrAl cell)	6.68	1.44

AC susceptibility measurements under pressure on complex **2a** shows one major phenomenon: conversion from the low temperature species (LT) to the high temperature species (HT).

3.1.3 Out of phase AC susceptibility

The out of phase AC susceptibility has been measured at various frequencies between 0.1 Hz and 40 Hz. The evolution of the out of phase AC susceptibility at 1 Hz and 10 Hz as a function of pressure has been plotted in Figure 3.2. The evolution of the out of phase AC susceptibility between ambient pressure and 1.44 GPa as a function of the frequency has been plotted in Figure 3.3. Tabulated values for the LT and HT peaks are available in their respective sections. Because the background is changing with pressure, the background constant from the fit (C parameter from Equation 2.4) has been subtracted from the data so all curves are lying on a common base line.

The different AC graphs m'' versus T reveal a conversion from the LT peak to the HT peak with increasing pressure. The ambient pressure AC susceptibility shows only one peak at low temperature (2.1 K at 1 Hz and 2.3 K at 10 Hz) whereas, at 1.44 GPa, only one peak is present at high temperature (4.1 K at 1 Hz and 4.8 K at 10 Hz). In between, both species are present in different proportions.

Results from the least squares fit are in a good agreement with the data as shown in the

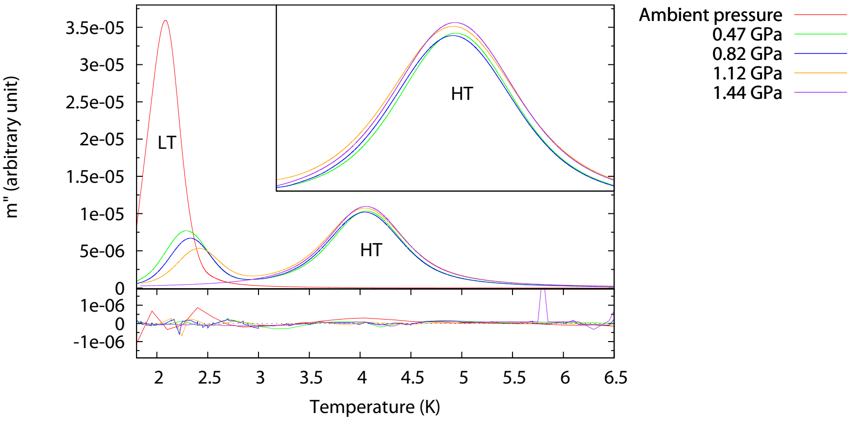

(a) 1 Hz

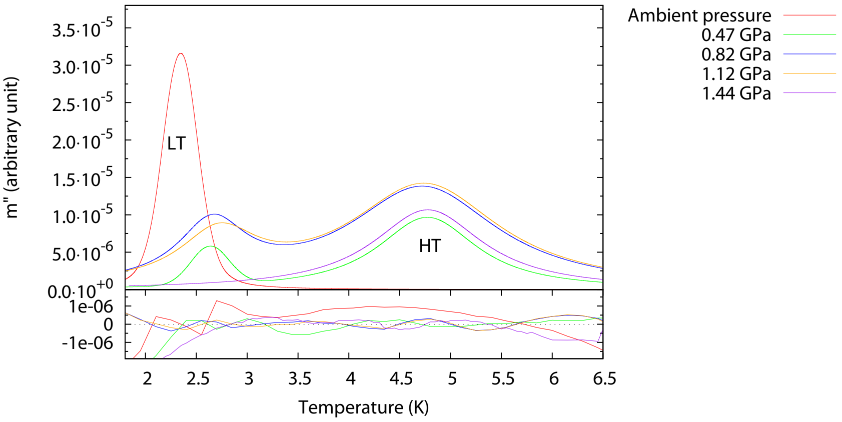

(b) 10 Hz

Figure 3.2: Evolution of the out of phase AC susceptibility peaks for complex **2a** under pressure at 1.00 Hz and 10.00 Hz. The background has been subtracted from the data with the calculated value from the fit (constant *C*). Lines are the best fit from equation 2.4 minus the background (constant *C*). The lower graphic in both a) and b) is the difference between the model and the experimental data. Raw data have been corrected with their respective background so all the curves lie on the same baseline.

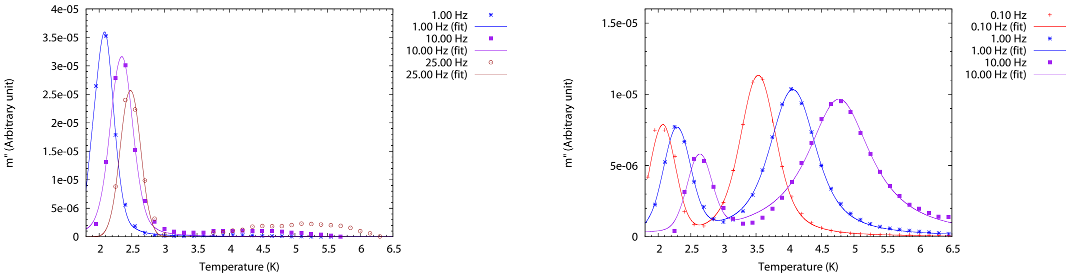

(a) ambient pressure

(b) 0.47 GPa

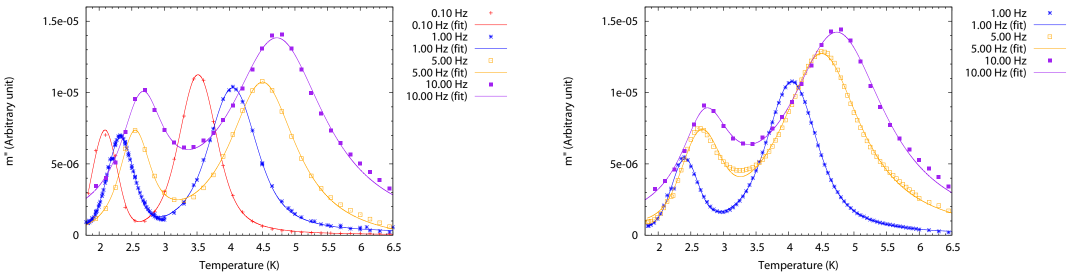

(c) 0.82 GPa

(d) 1.12 GPa

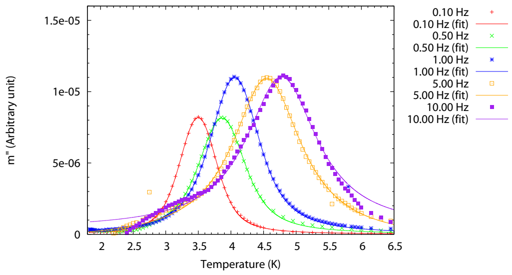

(e) 1.44 GPa

Figure 3.3: AC susceptibility data m'' versus T of **2a** at various frequencies and pressures. Lines are the best fit from equation 2.4. Raw data have been corrected with their respective background so all the curves lie on the same baseline.

lower sections of Figure 3.2. The ambient pressure experiment has a higher difference with the model due to a lack of data in this area (Figure 3.4). The low temperature part of the peak is absent and the steep slope of the peak can lead to higher errors. At 10 Hz, data already show a degradation due to the background which explains the larger deviation between the fit and the experimental data.

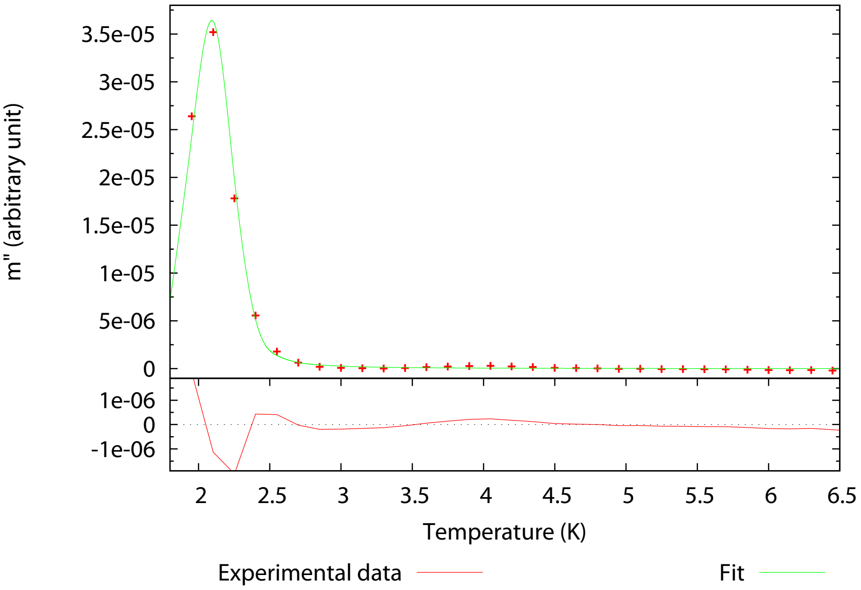

Figure 3.4: Details of the fitting of complex **2a** at ambient pressure and 1 Hz. Raw data have been corrected with its background.

Evolution of the energy barrier of the LT species

The peak positions obtained by least-squares fitting the out-of phase (m'') peaks using equation 2.4 for the LT species are listed in Table 3.2 for all pressures.

Data at 1 Hz and 10 Hz are available for all pressures. 0.1, 5 and 25 Hz are available at only certain frequencies. All the data show an increase in the temperature peak position at a certain frequency. The increase is 0.3 K at 1 Hz and 0.4 K at 10 Hz over 1.44 GPa. An increase of the temperature suggests an increase in the energy barrier.

The natural logarithm of the relaxation time as a function of the inverse temperature is shown in Figure 3.5. The energy barrier and relaxation time obtained from the least squares fit are summarised in Table 3.3. Because of the limited frequencies available, the value of the energy barrier only gives a rough idea.

According to these results, at ambient pressure, the energy barrier of the LT species of

Table 3.2: Out-of-phase Ac susceptibility results as a function of pressure for the LT isomer of complex **2a**

AC freq Hz	peak temp K	ln (τ)	(peak temp)$^{-1}$ K^{-1}
	Ambient pressure		
1	2.074	−1.838	0.482
10	2.343	−4.140	0.427
25	2.478	−5.058	0.403
	0.47 GPa		
0.1	2.069	0.465	0.484
1	2.290	−1.838	0.437
10	2.627	−4.140	0.381
	0.82 GPa		
0.1	2.087	0.465	0.479
1	2.327	−1.838	0.430
5	2.547	−3.447	0.392
10	2.658	−4.140	0.376
	1.12 GPa		
1	2.407	−1.838	0.416
5	2.653	−3.447	0.377
10	2.724	−4.140	0.367

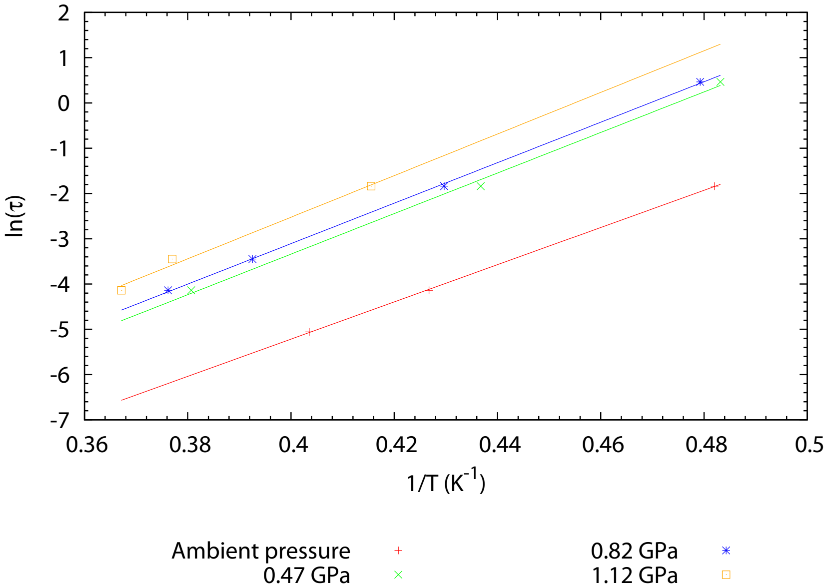

Figure 3.5: ln (τ) vs $1/T$ at different pressures for the LT species of complex **2a**. τ is given by $1/(2\pi\nu)$, with ν being the frequency at which the AC field was oscillating. The straight lines are the best fits to an Arhenius law, Equation 2.5.

Table 3.3: Evolution of the energy barrier and the relaxation time of the LT isomer of complex **2a** as a function of pressure

Pressure GPa	$\Delta E/k_B$ K	τ_0 s
0	41	4×10^{-10}
0.47	45	6×10^{-10}
0.82	45	8×10^{-10}
1.12	46	8×10^{-10}

$[Mn_{12}O_{12}(O_2CCH_2Bu^t)_{16}(H_2O)_4]\cdot MeNO_2\cdot CH_2Cl_2$ (**2a**) is 41 K. Soler *et al.*[26] reported an energy barrier of 42 K calculated from the out of phase AC susceptibility and DC magnetization decay on **2a**. They used crystals kept in their mother liquor for the experiment. The 1 K difference is probably not significant and could be due to the error in the fitting. From ambient pressure to 1.12 GPa, the energy barrier is increasing by 5 K from 41 to 46 K. It is difficult to say if the changes are significant as the fit only uses three or four frequencies.

However, these results are in agreement with an increase in temperature of the m'' peak position from the out of phase AC susceptibility.

At ambient pressure the τ_0 value of the LT species is 4×10^{-10} s. Soler *et al.*[26] reported a value of 2.2×10^{-10} s. The order of magnitude is about the same but it is difficult to tell if it is the difference is significant or not. On increasing pressure, the τ_0 value increases by 4×10^{-10} s. Unfortunately, no conclusion can be made on the increase as the difference might not be significant.

Evolution of the energy barrier of the HT species

In Table 3.4 the peak positions obtained by least-squares fitting the out-of phase m'' peaks with Voigt profiles using Equation 2.4 of complex **2a** (HT species) are listed from 0.47 GPa to 1.44 GPa.

On increasing pressure, the LT species show an increase in m'' peak temperature and the energy barrier. Results for the HT species are not as clear. Between 0.47 GPa and 1.44 GPa, the m'' peak temperatures are both increasing and decreasing, depending on the frequency and the differences are smaller than the changes encountered for the LT species. At 10 Hz, the m'' peak temperature only increases by 0.007 K while the change

Table 3.4: Out-of-phase Ac susceptibility results as a function of pressure for the HT isomer of complex **2a**

ac freq Hz	peak temp K	ln (τ)	(peak temp)$^{-1}$ K^{-1}
		0.47 GPa	
0.1	3.534	0.465	0.283
1	4.064	−1.838	0.246
10	4.771	−4.140	0.210
		0.82 GPa	
0.1	3.515	0.465	0.284
1	4.046	−1.838	0.247
5	4.506	−3.447	0.222
10	4.729	−4.140	0.211
		1.12 GPa	
1	4.048	−1.838	0.247
5	4.504	−3.447	0.222
10	4.745	−4.140	0.211
		1.44 GPa	
0.1	3.498	0.4647	0.286
0.5	3.862	−1.145	0.259
1	4.058	−1.838	0.246
5	4.549	−3.447	0.220
10	4.778	−4.140	0.210

for the LT species at the same frequency was 0.4 K. In these conditions, it is difficult to conclude whether any changes are significant.

The natural logarithm of the relaxation time as a function of the inverse temperature is shown in Figure 3.6. The energy barriers and the τ_0 values obtained from the least squares fit are summarised in Table 3.5.

Table 3.5: Evolution of the energy barrier and the relaxation of the HT isomer complex **2a** as a function of pressure

Pressure GPa	Energy barrier K	Relaxation time s
0.47	63	3×10^{-8}
0.82	63	3×10^{-8}
1.12	64	2×10^{-8}
1.44	60	6×10^{-8}

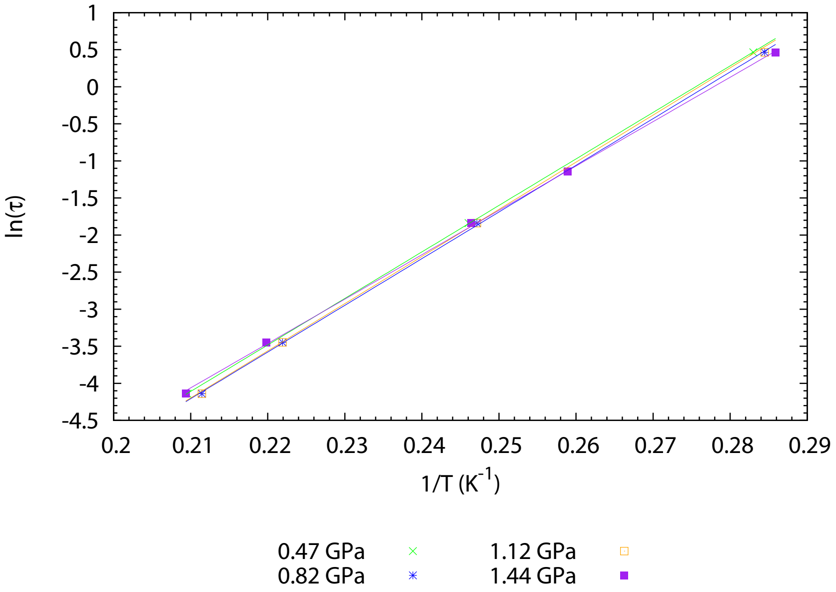

Figure 3.6: $\ln(\tau)$ vs $1/T$ at different pressures for the HT species of complex **2a**. τ is given by $1/(2\pi\nu)$, with ν being the frequency at which the AC field was oscillating. The straight lines are the best fits to an Arhenius law, Equation 2.5.

At 0.47 GPa, the energy barrier of the pressure-induced HT species is 63 K. This value is similar to the value of 62 K found by Soler *et al.*[26] on the high temperature complex $[Mn_{12}O_{12}(O_2CCH_2Bu^t)_{16}(H_2O)_4] \cdot CH_2Cl_2 \cdot MeNO_2$ (**2a**) at ambient pressure. Soler *et al.*[26] reported that complex **2a** has a tilted elongated Jahn-Teller axis compared to $[Mn_{12}O_{12}(O_2CCH_2Bu^t)_{16}(H_2O)_4] \cdot CH_2Cl_2 \cdot MeCN$ (**2b**) (Figure 3.1). The out of phase AC susceptibility reported by Soler *et al.*[26] on complex **2a** shows that the low temperature peak belongs to the fast relaxing species **2a**. Similarly, the high temperature peak belongs to the slow relaxing species **2b**. Hence, the AC m'' data reported by Soler *et al.*[26] on both **2a** and **2b** is consistent with a conversion of **2a** from the low temperature species to the high temperature species with increasing pressure. High pressure X-ray crystallography confirms a conversion of **2a** from low temperature species to high temperature species with applied pressure (Section 3.1.5).

From 0.47 GPa to 1.12 GPa, our data do not reveal any changes in the energy barrier. Compared to the small fluctuations of the m'' peaks from the out of phase AC susceptibility, the value of the energy barrier is understandable and no significant changes occurred. However, At 1.44 GPa, the fitting results in a value of 60 K for the energy barrier and the m'' peaks do not show a clear decrease in the temperature at all frequencies. Thus, no conclusion can be made on the decrease of the energy barrier at 1.44 GPa.

3.1.4 Hysteresis loop

In the out of phase AC susceptibility of **2a** we have seen a conversion from the FR species to the SR species, which will cause an increase in the energy barrier to reorientation of the magnetisation. Thus, the hysteresis loop should open under pressure because $\Delta E/k_B$ increases, hence T_B increases and the loop is wider.

The ambient pressure hysteresis loop (*ie* measured in a straw) shows a step at 1 T. This is due to the presence of a HT species impurity (Figure 3.7). The sample in the pressure cell does not have this impurity as shown in the AC susceptibility results at ambient pressure in the pressure cell (Figure 3.3) and on the hysteresis loop at ambient pressure (Figure 3.7). Two different samples, both single crystals, from the same synthesis have been used. One has been placed in a gelatine capsule for the ambient pressure measurement in the straw; the other one has been put in the Teflon® capsule and then placed in the pressure cell. The main consequence is a small error in the background as the ambient pressure dataset outside the cell is used to calculate the signal from the sample (Equation 2.6).

The evolution of the hysteresis loop under pressure is summarised in Figure 3.8 and Figure 3.9. Curves are the best fit using equation 2.10. The first noticeable result is an opening of the hysteresis loop, this implies an increase in the energy barrier which is indeed observed in the out of phase AC susceptibility experiments with a conversion from the FR species to SR species. The loop is not fully open as is in Mn_{12} acetate but is similar to the hysteresis loop of **1** at high pressure (Figure 3.24 in Section 3.2.4).

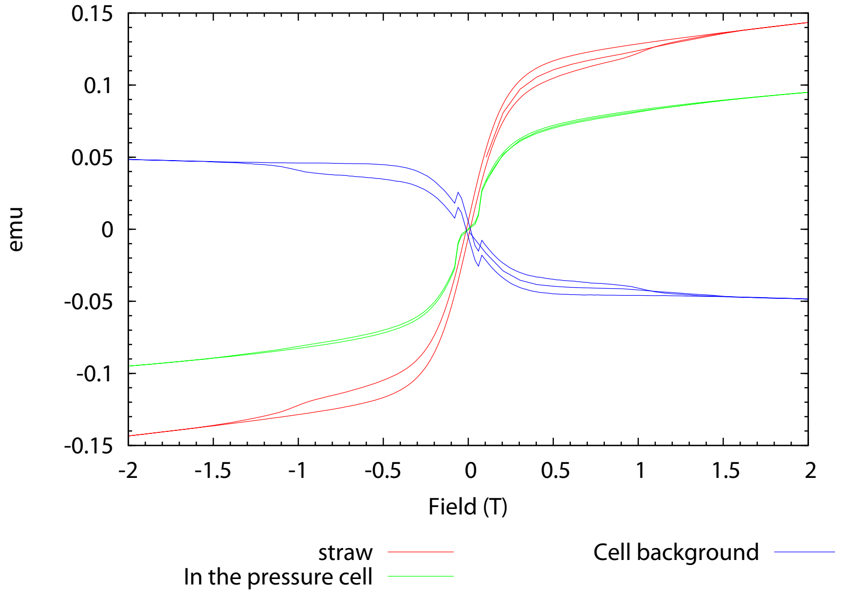

Figure 3.7: Hysteresis loop of **2a** outside the pressure cell, in the pressure cell at ambient pressure and the resulting background.

The results from the fitting in Table 3.6 gives an anisotropy between 0.66 K and 0.68 K in the range 0.47 GPa – 1.12 GPa. At 1.44 GPa, the anisotropy drops to 0.61 K. Using equation 2.11 and assuming a ground spin state equal to 10^{70} and fixed on increasing pressure gives the energy barrier summarised in Table 3.7.

The energy barrier calculated from the hysteresis loop results from the first order Hamiltonian. Ignoring higher order terms may explain the differences between the results from the out of phase AC susceptibility and the hysteresis loop. However, there is a correlation between the two experiments. Both results have an energy barrier more or less stable within ±1 K between ambient pressure and 1.12 GPa. At 1.44 GPa, both experiments show a drop in the energy barrier. Even more interesting, both experiments reported the same value of the energy barrier at 1.44 GPa, although this does not prove that the value is reliable.

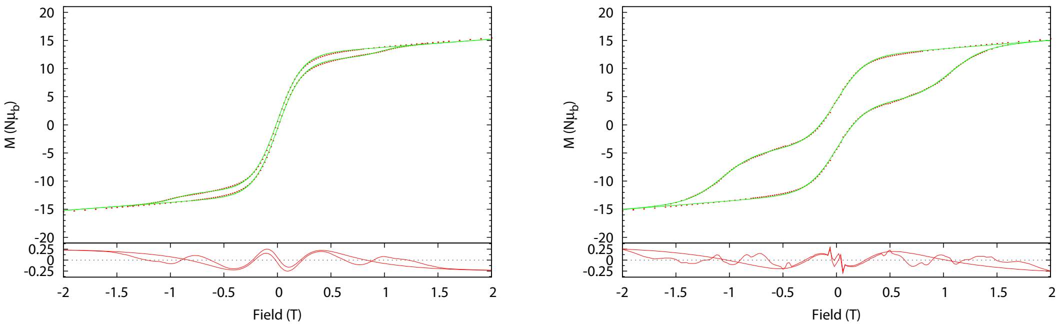

(a) ambient pressure (b) 0.47 GPa

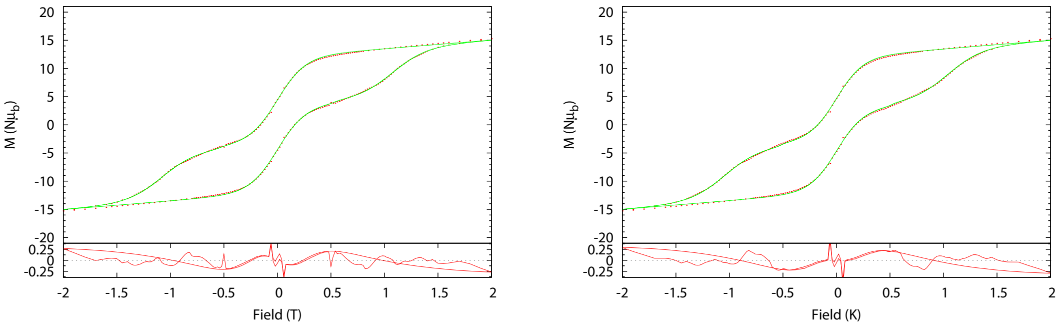

(c) 0.82 GPa (d) 1.12 GPa

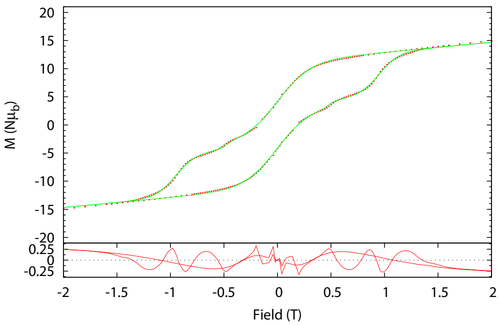

(e) 1.44 GPa

Figure 3.8: Hysteresis loop of **2a** at different pressures. In the top part of each graph, red points are the experimental data after removal of the background and the straight line is the best fit using Equation 2.10. The bottom section of each graph is the difference between the experimental data and the model. The ambient pressure hysteresis loop reported here was collected outside the pressure cell.

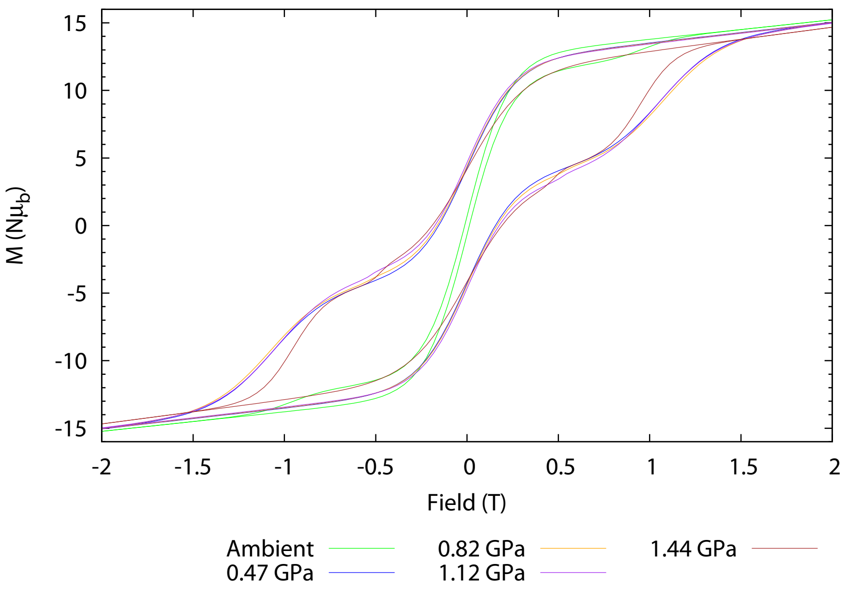

Figure 3.9: Evolution of the hysteresis loops of **2a** from ambient pressure to 1.45 GPa, the straight line is the best fit using Equation 2.10.

Table 3.6: Step parameters on the hysteresis loops of **2a**. M_s^i is the height of a given step. The curvature is the slope at the inflexion point. H_0 is the coercive field at which the step occurred. H_0 is calculated from Equation 2.10 from the fitting parameter D.

0.47 GPa		
M_s^i M ($N\mu_B$)	Curvature	H_0 T
7.70	3.75	0.00
0	7.36	0.53
4.29	3.20	1.06
D = 0.68 K		

0.82 GPa		
M_s^i M ($N\mu_B$)	Curvature	H_0 T
7.52	3.80	0.00
0.10	21.03	0.54
4.32	3.13	1.08
D = 0.69 K		

1.12 GPa		
M_s^i M ($N\mu_B$)	Curvature	H_0 T
7.21	3.99	0.00
0.14	27.08	0.52
4.53	3.08	1.04
D = 0.66 K		

1.44 GPa		
M_s^i M ($N\mu_B$)	Curvature	H_0 T
6.96	3.23	0.00
0.43	20.06	0.48
3.74	5.43	0.95
D = 0.61 K		

Table 3.7: Energy barrier comparison on complex **2a**

Pressure GPa	Ac measurements K	Hysteresis loop fit K
0.47	63	68
0.82	63	69
1.12	64	67
1.44	60	61

3.1.5 High-Pressure Crystallography

A sphere of data was collected as explained in Section 2.2. The final conventional R-factor was 0.0525 at ambient pressure (Table 3.8). The R-factors for the pressure data are between 10 % and 11 %. These values are quite reasonable given the relatively modest level of modelling that is possible with such low completeness data. Listings of crystal and refinement data are given in Table 3.8.

Table 3.8: Crystallographic data for the single crystal diffraction study of **2a** at increasing pressure.

Pressure (GPa)	Ambient	1.5	2.5
Formula	$[Mn_{12}O_{12}(O_2CCH_2Bu^t)_{16}(H_2O)_4]\cdot xMeNO_2\cdot yCH_2Cl_2$		
x, y	1, 1	0.75, 0.5	0, 0
Space group	$P-1$	$P-1$	$P-1$
a (Å)	15.8368(4)	15.3530(11)	15.0148(19)
b (Å)	16.4179(5)	15.5310(11)	15.1418(19)
c (Å)	27.3955(7)	26.7020(12)	26.7583(19)
α	76.817(2)	76.669(5)	76.184(9)
β	78.161(1)	76.441(5)	76.208(8)
γ	78.264(2)	78.069(5)	79.415(8)
Volume (Å^3)	6695.5(3)	5943.8(7)	5685.1(11)
Radiation type	Mo Kα	Synchrotron	Synchrotron
λ (Å)	0.71073	0.4780	0.4780
Refinement	$\|F\|^2$	$\|F\|^2$	$\|F\|^2$
Z	2	2	2
R^a, $wR2^b$, S^c	0.052, 0.145, 1.04	0.109, 0.250, 1.04	0.105, 0.256, 1.03
Reflections	26597	4842	3438
Parameters	1442	776	776

$^aR = \sum \left| |F_o| - |F_c| \right| / \sum |F_o|$

$^bwR2 = \sum w\left(F_o^2 - F_c^2\right)^2 / \sum w\left(F_o^2\right)^2$

$^cS = \sqrt{\sum w\left({F^o_{hkl}}^2 - {F^c_{hkl}}^2\right) / (n-p)}$

Results and Discussion

The structure of 2a at ambient pressure The molecule has the same $[Mn_{12}O_{12}]$ core as Mn_{12} acetate[12] and consists of a central $[Mn_4^{IV}O_4]^{8+}$ cubane held within a non-planar ring of eight Mn^{III} atoms, linked by eight $\mu_3 - O^{2-}$ ions. Peripheral ligation differs from the classical Mn_{12} acetate by using $Bu^tCH_2COO^-$ groups instead of acetate. The Mn_{12} acetate lies on a S_4 axis whereas there is no symmetry operator on **2a**. Four H_2O ligands are also present as in the Mn_{12} acetate complex (Figure 3.10). However, in the Mn_{12} acetate, the four H_2O ligands are symmetry equivalents around the S_4 axis. Whereas in complex **2a**, two H_2O ligands are on Mn12 and forming the two Jahn-Teller elongated bonds. The two remaining H_2O ligands are on Mn10 and Mn6 atoms. **2a** crystallised with one nitromethane solvent molecule and one dichloromethane solvent molecule. There is one ordered molecule of $MeNO_2$ and a dichloromethane molecule disordered over two sites at 150 K.[26]

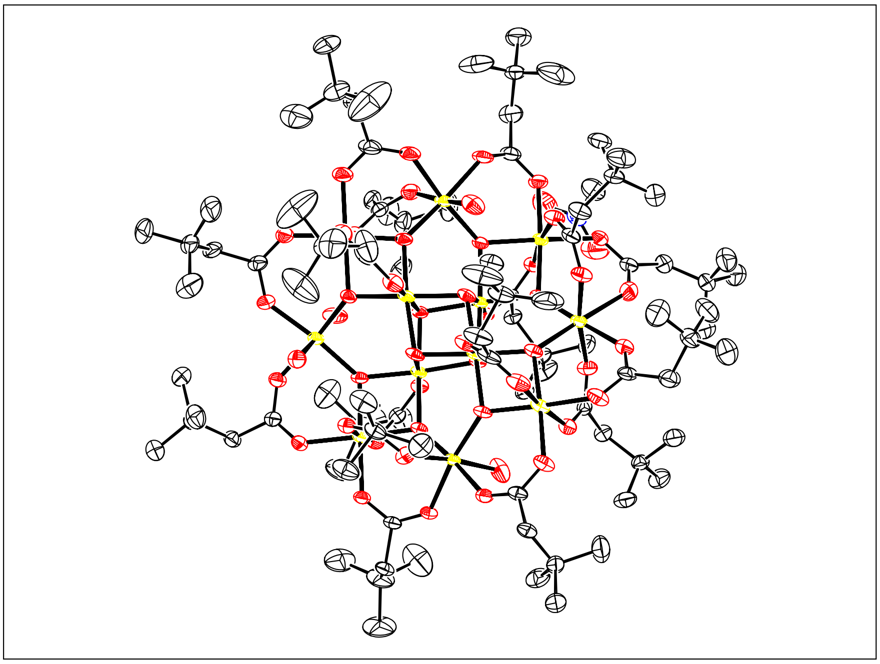

Figure 3.10: Ortep drawing at ambient pressure of **2a**. Hydrogen atoms are omitted for clarity. Mn are in yellow, O in red and C in white. Solvent molecules omitted.

While all the elongated Jahn-Teller axes in Mn_{12} acetate are pointing in the same direction, **2a** has seven "vertical" Jahn-Teller axis and one "horizontal" Jahn-Teller axis at 150 K. The horizontal Jahn-Teller axis is located on Mn8, (Figure 3.11) and Mn–O bond lengths are reported in Table 3.9 (numbers in bold are the Jahn-Teller elongated bond lengths). This behaviour is the key to the magnetic properties of the complex as the molecule with a tilted Jahn-Teller axis is the LT species and the molecule with all the Jahn-Teller axes "vertical" is the HT species. At room temperature the Mn8–O distances span

1.930(4)-2.025(4) Å; the lack of a clear Jahn–Teller axis suggests disorder. The molecules interact via van der Waals interactions between ^{t}Bu groups.

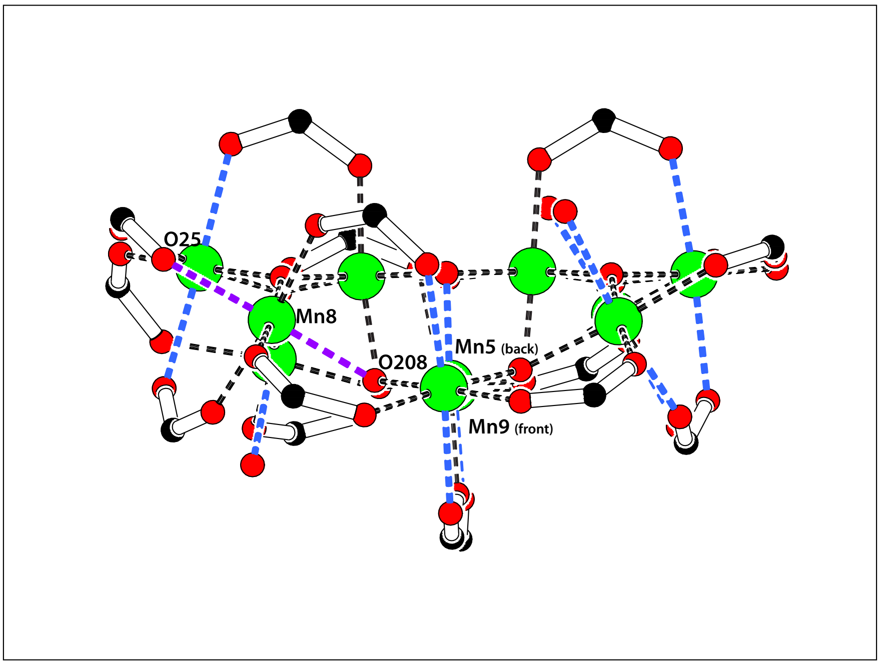

Figure 3.11: Highlight of the elongated Jahn-Teller axis on **2a** at ambient pressure. The "vertical" elongated Jahn-Teller axes are coloured in blue, the horizontal elongated Jahn-Teller axis is coloured in purple. Hydrogen and CH_2Bu^t groups are omitted for clarity. Mn are in green, O in red and C in black and solvent molecules are omitted. The projection is along the Mn9 and Mn5 ions.

The structure of 2a at 1.5 GPa Between ambient pressure and 1.5 GPa, **2a** reveals no general trend on the Mn(III)–O bonds length. On focusing on the elongated Jahn-Teller axis, a similar behaviour is noticed. Two elongated Jahn-Teller axis increase in length: Mn5–O212 increases by 0.09(2) Å from 2.209(3) Å to 2.30(2) Å and Mn6–O6 increases by 0.07(2) Å from 2.253(3) Å to 2.32(2) Å (Figure 3.12). However, elongated Jahn-Teller axes on Mn5 and Mn6 decrease in length. Mn5–O19 is decreasing by 0.02(2) Å from 2.181(3) Å to 2.161(18) Å and Mn6–O29 is decreasing by 0.07(2) Å from 2.111(3) Å to 2.044(19) Å (Figure 3.12). As a result the elongated Jahn-Teller axes on these Mn(III) ions are asymmetric. The other elongated Jahn-Teller axes on Mn7, Mn9, Mn10, Mn11 and Mn12 all decrease by about 0.02 Å in average.

The Jahn-Teller distorted Mn8 centre shows the most interesting result: four Mn8–O bonds are increasing and two are decreasing. At ambient pressure, the elongated Jahn-Teller bonds were Mn8–O25 and Mn8–O208, however at 1.5 GPa, this is no longer the case. There is no clear elongated Jahn-Teller axis as four bonds are above 2 Å. The longest bond is Mn8–O14 with 2.117(19) Å, then there are two bonds Mn8–O13 and Mn8–O26

Table 3.9: Mn–O bonds length of the eight Mn^{3+} ions from complex **2a**. The tilting of the Jahn-Teller axis is on Mn8. Bold values are the elongated Jahn-Teller axis.

Bond	Ambient pressure – 150 K	1.5 GPa – RT	2.5 GPa – RT
Mn5–O19	**2.181(3)**	**2.161(18)**	**2.10(2)**
Mn5–O110	1.949(3)	1.97(2)	1.99(3)
Mn5–O211	1.936(3)	1.90(3)	1.89(3)
Mn5–O212	**2.209(3)**	**2.30(2)**	**2.16(3)**
Mn5–O405	1.917(2)	1.97(2)	1.98(3)
Mn5–O406	1.861(3)	1.82(2)	1.81(3)
Mn6–O6	**2.253(3)**	**2.32(2)**	**2.34(3)**
Mn6–O18	1.929(3)	1.95(2)	1.88(2)
Mn6–O29	**2.111(3)**	**2.044(19)**	**2.18(2)**
Mn6–O107	1.899(2)	1.921(18)	1.90(2)
Mn6–O210	1.959(3)	1.96(2)	1.93(3)
Mn6–O406	1.864(2)	1.90(2)	1.87(3)
Mn7–O15	1.921(3)	1.97(2)	1.94(3)
Mn7–O16	**2.199(3)**	**2.129(15)**	**2.08(2)**
Mn7–O27	**2.193(2)**	**2.190(14)**	**2.15(2)**
Mn7–O28	1.960(3)	1.90(2)	1.98(3)
Mn7–O107	1.915(3)	1.90(2)	1.93(3)
Mn7–O108	1.893(2)	1.870(19)	1.90(3)
Mn8–O13	1.963(3)	**2.03(3)**	1.84(3)
Mn8–O14	1.961(2)	**2.117(19)**	**2.15(2)**
Mn8–O25	**2.145(3)**	2.01(2)	2.01(3)
Mn8–O26	1.956(3)	**2.03(2)**	**2.22(3)**
Mn8–O108	1.893(3)	1.958(19)	1.89(3)
Mn8–O208	**2.049(3)**	1.94(2)	1.88(3)
Mn9–O23	1.953(3)	1.97(2)	1.95(3)
Mn9–O24	**2.208(2)**	**2.169(14)**	**2.098(18)**
Mn9–O114	1.958(3)	1.962(18)	1.92(2)
Mn9–O208	1.859(3)	1.87(2)	1.86(3)
Mn9–O209	1.894(3)	1.92(2)	1.92(3)
Mn9–O215	**2.195(3)**	**2.151(17)**	**2.21(2)**
Mn10–O10	**2.261(3)**	**2.26(2)**	**2.28(3)**
Mn10–O116	**2.103(3)**	**2.08(2)**	**2.19(3)**
Mn10–O117	1.958(2)	1.942(19)	1.95(3)
Mn10–O209	1.886(2)	1.891(19)	1.88(2)
Mn10–O214	1.941(3)	1.909(16)	1.97(2)
Mn10–O310	1.886(3)	1.91(2)	1.81(3)
Mn11–O213	1.948(3)	1.968(19)	1.97(3)
Mn11–O216	**2.184(2)**	**2.141(18)**	**2.13(2)**
Mn11–O217	1.930(3)	1.871(19)	1.87(2)
Mn11–O218	**2.201(2)**	**2.18(2)**	**2.22(3)**
Mn11–O310	1.894(2)	1.93(2)	1.94(3)
Mn11–O311	1.892(2)	1.89(2)	1.83(3)
Mn12–O111	1.941(3)	1.99(2)	1.99(3)
Mn12–O113	1.945(3)	1.922(19)	1.87(3)
Mn12–O120	**2.257(3)**	**2.27(3)**	**2.24(4)**
Mn12–O121	**2.218(3)**	**2.12(2)**	**2.12(3)**
Mn12–O311	1.860(3)	1.87(2)	1.91(3)
Mn12–O405	1.884(2)	1.879(19)	1.89(3)

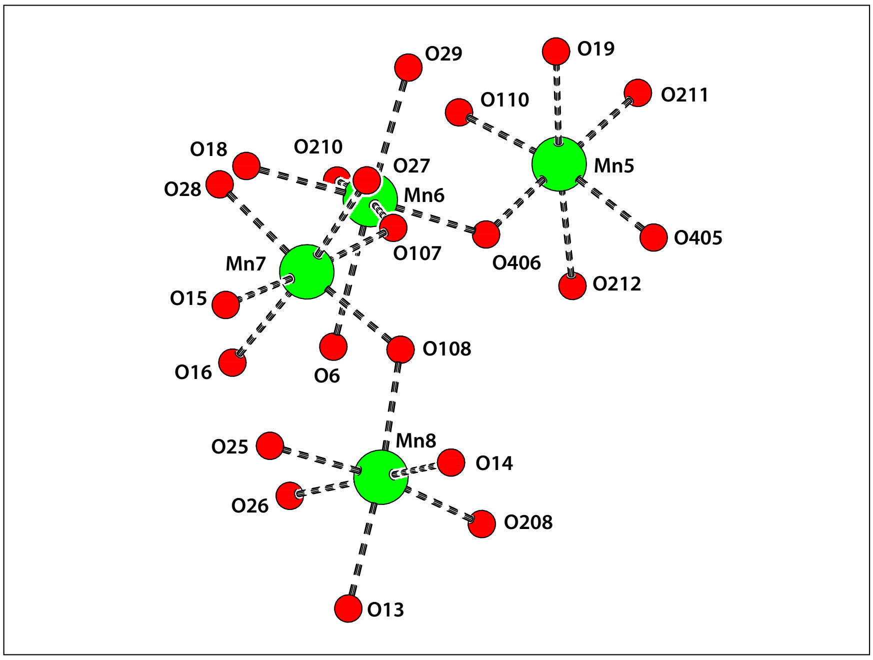

Figure 3.12: Mn5, Mn6, Mn7 and Mn8 coordination sphere. Mn are in green and O in red.

with the same bond length 2.03(3) Å (Table 3.9 and Figure 3.12).

At 1.5 GPa the occupancies of the solvent model best with a combined total of 1.25 molecules per formula unit.

The structure of 2a at 2.5 GPa At 2.5 GPa, the behaviour of the elongated Jahn-Teller axes on Mn8 is now clear. From ambient pressure, the "horizontal" elongated Jahn-Teller axis along Mn8–O25 and Mn8–O208 tilts to a "vertical" elongated Jahn-Teller axis along Mn8–O14 and Mn8–O26 (Figure 3.13).

Between 1.5 GPa and 2.5 GPa, most of the elongated Jahn-Teller axes on the remaining centres do not change given their standard deviation. Release of pressure re-establishes the coordination seen at ambient pressure. The solvent was removed altogether in modelling the 2.5 GPa dataset. Models of partially occupied solvent can be subjected to reinterpretation even with fully complete diffraction data. At high pressure, where data are incomplete because of the pressure cell, the situation is yet more uncertain. However, the data suggest that the solvent is released into the hydrostatic medium on compression, and reabsorbed on decompression (Table 3.8). Conversion from fast-relaxing to slow-relaxing Mn_{12} species can be affected by solvent loss, and our high pressure data appear to be consistent with this theory.[26]

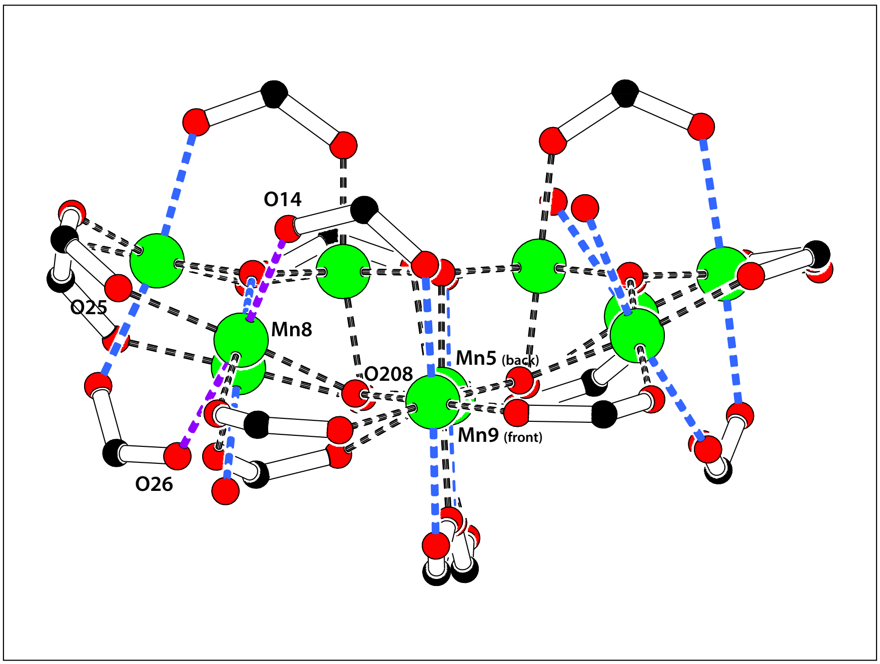

Figure 3.13: Highlight of the elongated Jahn-Teller axes on **2a** at 2.5 GPa. Hydrogen and CH_2Bu^t groups are omitted for clarity. Mn are in green, O in red and C in black. The projection is along the Mn9 and Mn5 ions.

3.2 $[Mn_{12}O_{12}(MeCO_2)_{16}(H_2O)_4] \cdot 2\,CH_3COOH \cdot 4\,H_2O$

3.2.1 Synthesis

A 40 mL solution 60 % of CH_3CO_2H by volume in water is prepared.

1. 1 g of $KMnO_4$ is dissolved in 25 mL of the previous solution. The solution is stirred for 1 h to assure complete dissolution.
2. A second solution is prepared with 4.2 g of $Mn(O_2CCH_3)_2 \cdot 4\,H_2O$ in the remaining 15 mL of the 60 % CH_3CO_2H solution. The solution is stirred for 1 h until complete dissolution.
3. Solution 1) was quickly added to solution 2) and stirred for 2 minutes, no more. The resulting solution is left undisturbed overnight in a closed Erlenmeyer flask. Black needle crystals (Figure 3.14) of $[Mn_{12}O_{12}(MeCO_2)_{16}(H_2O)_4] \cdot 2\,CH_3COOH \cdot 4\,H_2O$ (**1**) are collected by filtration and washed with acetone to remove any excess CH_3CO_2H. Crystallisation at low temperature (0-5° C) gives slightly bigger crystals but takes longer. The yield is 50 % on average for ambient temperature crystallisation and around 30 % for low temperature crystallisation.

Anal. Calcd: C, 20.99; H, 3.52. Found: C, 20.84; H, 3.45.

Figure 3.14: Black needle crystals of **1**.

3.2.2 Data collection

Two different samples of $[Mn_{12}O_{12}(MeCO_2)_{16}(H_2O)_4] \cdot 2\,CH_3COOH \cdot 4\,H_2O$ (**1**) have been used. One experiment has been done on single crystals in the MPMS at the university of Glasgow which is going to be referred as "single crystals" and one experiment has been done on a powdered sample in the PPMS at the university of Edinburgh by Javier Sanchez-Benitez which is going to be referred as "powder".

Table 3.10: Dataset of the pseudo aligned crystals of Mn_{12} acetate (Glasgow sample). T_c is the superconducting transition of the pressure calibrant (tin).

Dataset	T_c (Sn) K	Pressure GPa
HP0	3.68	0
HP1	3.58	0.33
HP2	3.45	0.60
HP3	3.23	1.10
HP4	3.08	1.45

Table 3.11: Dataset of the powder sample of Mn_{12} acetate (Edinburgh)

Dataset	Pressure GPa
HP0	0
HP1	0.66
HP2	1.10
HP3	1.50

Five datasets of the single crystals sample (Glasgow) from ambient pressure to 1.45 GPa were collected on five pseudo-aligned single crystals in the NiCrAl cell using the MPMS

(Table 3.10). The experiment was also performed on the PPMS at CSEC in Edinburgh on a ground powdered sample in another NiCrAl cell. Four datasets of the powder sample (Edinburgh) were collected from ambient pressure to 1.5 GPa (Table 3.11).

3.2.3 Ac susceptibility

The AC susceptibility of the pseudo aligned single crystals sample was measured down to 1.8 K at different frequencies between 0.1 Hz and 50 Hz. The powder sample (Edinburgh) was measured down to 3 or 2 K at different frequencies between 0.1 and 130 Hz. Data from single crystals sample are composed of about 90 data points (one data point per temperature) for each frequency whereas the powder data have been measured with 20 data points or less for each frequency which, makes the fitting more reliable on the single crystals data (Figure 3.15 and Figure 3.16).

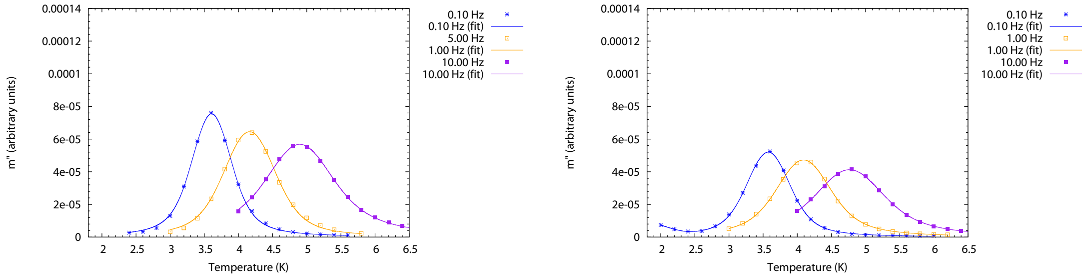

(a) ambient pressure

(b) 0.66 GPa

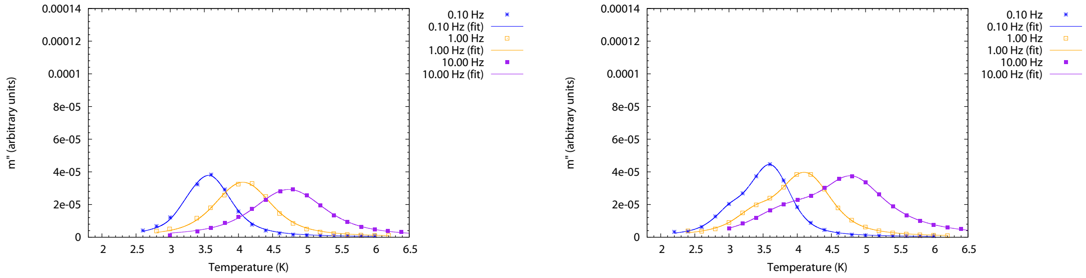

(c) 1.10 GPa

(d) 1.50 GPa

Figure 3.15: AC susceptibility data for **1** from powder sample at various frequencies and pressures. Lines are the best fit from equation 2.4. Raw data have been corrected with their respective background so all the curves lie on the same baseline.

The AC susceptibility results from complex **1** are much more complicated than from complex **2a**. The shape of the peaks of complex **1** suggest a splitting of the peaks at the highest pressure dataset (1.45-1.50 GPa) for the HT species on both samples (Figure 3.17). As one curve indicates one species, using two curves implies the presence of

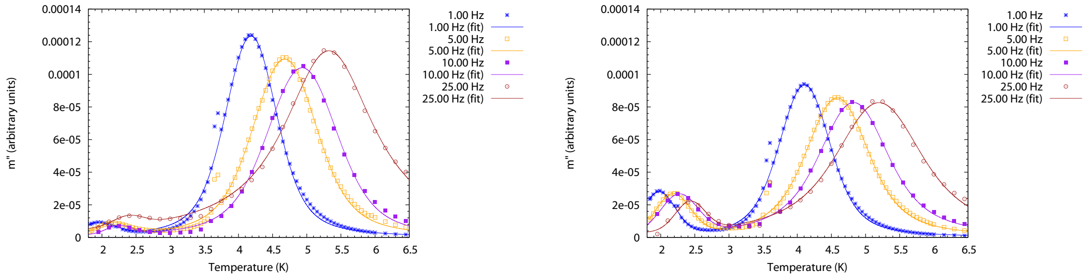

(a) ambient pressure

(b) 0.33 GPa

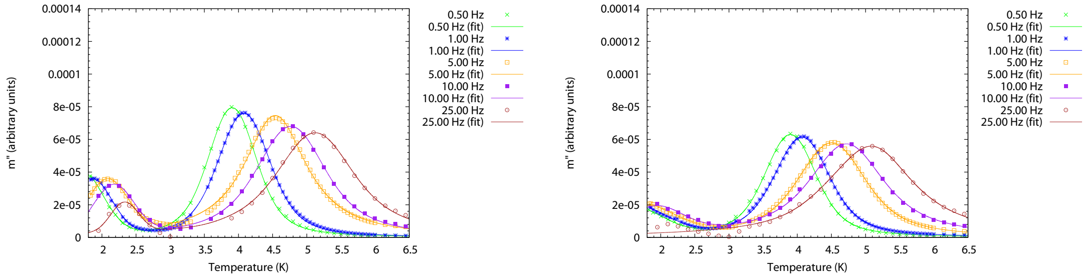

(c) 0.60 GPa

(d) 1.10 GPa

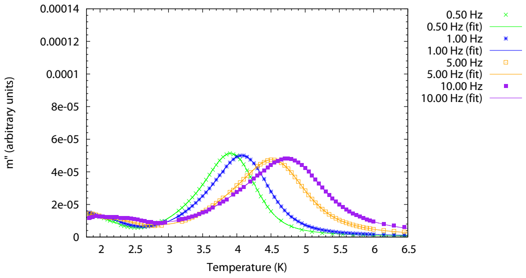

(e) 1.45 GPa

Figure 3.16: AC susceptibility data for **1** from pseudo-aligned single crystals (MPMS) at various frequencies and pressures. Lines are the best fit from equation 2.4. Raw data have been corrected with their respective background so all the curves lie on the same baseline.

two species. The presence of a second species can have a significant influence on the energy barrier calculation as both peaks are not resolved which implies a non-optimal fit of the two peaks. Two Voigt profiles have been used for the fitting at 1.45-1.50 GPa in order to take account of the shoulder.

The LT species have a similar behaviour at 1.45 GPa, the peak splits into two unresolved peaks. This haapened only on single crystals measurements (Figure 3.18), as the powder data were not measured to 1.8 K. The main problem is the lack of data at low temperature which makes the fitting very difficult. The peak position of the first LT peak is between 1.6 and 1.8 K at 0.5 Hz and 5 Hz and because our data do not go below 1.8 K, again, the result of the fit of the LT species is not optimal. A successful fit has been made up to 0.82 GPa.

The evolution of the temperature of the position of the peak as a function of pressure at a given frequency reveals a decrease in the temperature at all frequencies for the HT species in both pseudo aligned crystals (Figure 3.19) and powdered samples. This suggests a decrease in the energy barrier. Concerning the LT species, it is not possible to conclude on an increase or a decrease in the peak temperature.

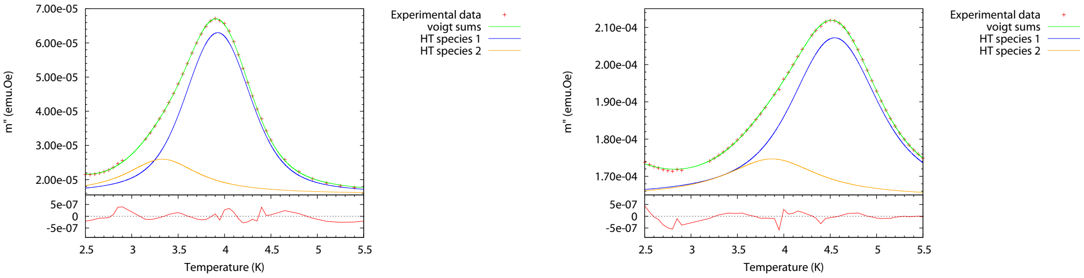

(a) 0.50 Hz, pseudo aligned crystals

(b) 5.00 Hz, pseudo aligned crystals

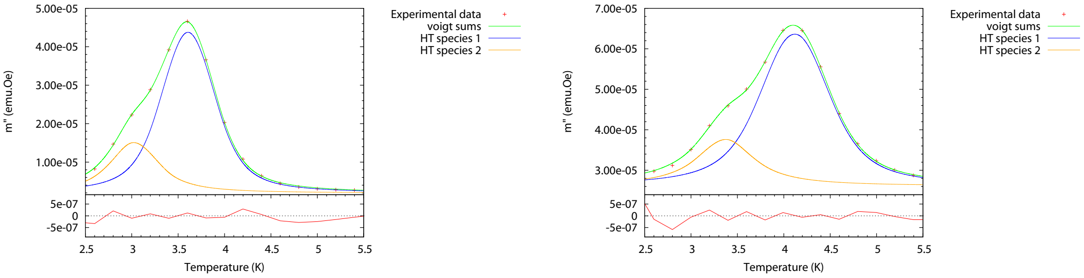

(c) 0.10 Hz, powdered samples

(d) 1.00 Hz, powdered samples

Figure 3.17: Details of the shoulder of the HT species of complex **1** at 1.50 GPa on pseudo aligned crystals and powdered samples. Unfortunately, no common frequencies are present. The lower graphic is the difference between the experimental data and the model.

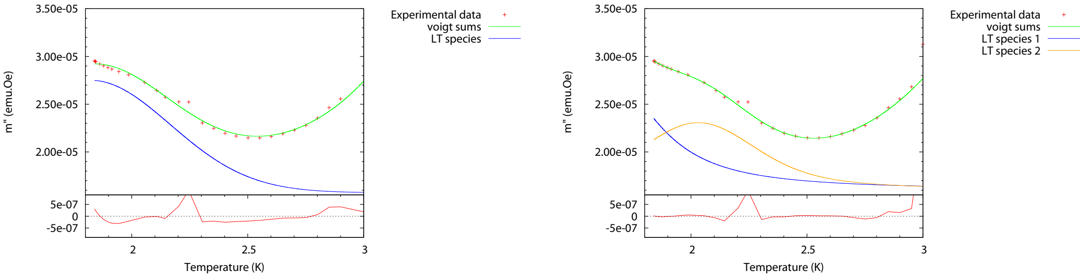

(a) 0.50 Hz, one curve fit

(b) 0.50 Hz, two curve fit

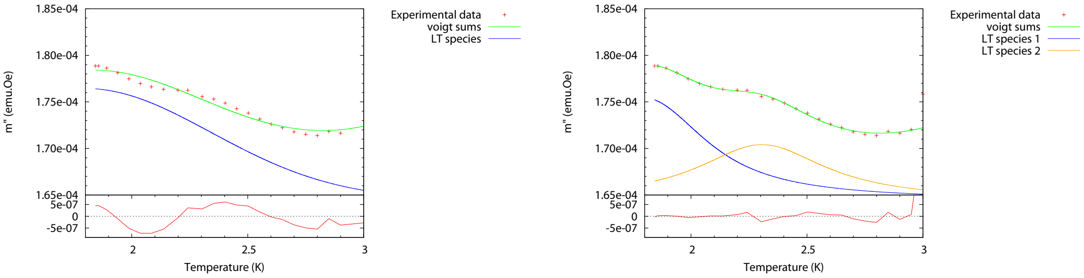

(c) 5.00 Hz, one curve fit

(d) 5.00 Hz, two curve fit

Figure 3.18: Details of the shoulder of the LT species of complex **1** at 1.45 GPa on pseudo aligned crystals sample. The lower graphic is the difference between the experimental data and the model.

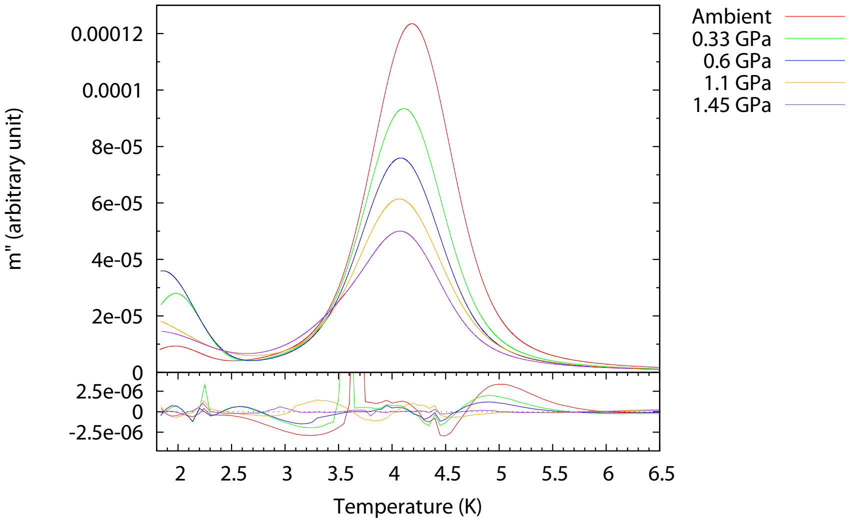

Figure 3.19: Evolution of the out of phase Ac susceptibility peak of **1** from pseudo aligned crystals sample under pressure at 1.00 Hz. Lines are the best fit from Equation 2.4. The lower graphic is the difference between the experimental data and the model. Raw data have been corrected with their respective background so all the curves lie on the same baseline.

Evolution of the energy barrier of the HT species

In Table 3.12 the peak positions obtained by least-squares fitting the out-of phase AC susceptibility peaks with Voigt profiles are listed for all pressures of the crystals.

Between ambient pressure and 0.60 GPa, the out of phase AC susceptibility peaks move to lower temperature on both single crystals and powder samples which suggests a decrease in the energy barrier. At higher pressure, it is not very clear. The shoulder appearing on the peak could explain the inconsistency. We do not know how many Voigt profiles have to be used for the peaks, usually, one peak is one species and thus one Voigt profile. But if one Voigt profile is used instead of two or more, it can lead to a wrong estimation of the true peak positions. Consequently, the decrease of the peak position could be due to a decrease in the energy barrier or the increase of the contribution of hidden peaks.

The natural logarithm of the relaxation time as a function of the inverse temperature is shown in Figure 3.20. The energy barrier and relaxation time obtained from the least squares fit are summarised in Table 3.13.

According to these results (Table 3.13), the energy barrier is increasing from 63 K at ambient pressure to 67-68 K at 1.4-1.5 GPa.

Table 3.12: Out-of-phase AC susceptibility results at different pressures of pseudo-aligned crystals of **1** (Glasgow sample).

AC freq Hz	peak temp K	$\ln(\tau)$	(peak temp)$^{-1}$ K^{-1}
	Ambient pressure		
1	4.188	−1.838	0.239
5	4.678	−3.447	0.214
10	4.936	−4.140	0.203
25	5.323	−5.057	0.188
	0.33 GPa		
1	4.109	−1.838	0.243
5	4.586	−3.447	0.218
10	4.825	−4.140	0.207
25	5.197	−5.057	0.192
	0.60 GPa		
0.5	3.908	−1.145	0.256
1	4.080	−1.838	0.245
5	4.538	−3.447	0.220
10	4.767	−4.140	0.210
25	5.123	−5.057	0.195
	1.10 GPa		
0.5	3.942	−1.145	0.254
1	4.109	−1.838	0.243
5	4.587	−3.447	0.218
10	4.822	−4.140	0.207
25	5.128	−5.057	0.195
	1.45 GPa		
0.5	3.927	−1.145	0.255
1	4.100	−1.838	0.244
5	4.531	−3.447	0.221
20	5.002	−4.834	0.200

Table 3.13: Evolution of the energy barrier and the relaxation of the LT peak of complex **1** as a function of pressure

Pressure GPa	U Gla K	U Ed K	τ_0 Gla s	τ_0 Ed s
Ambient	63	63	4.3×10^{-8}	4.7×10^{-8}
0.33	63	–	3.2×10^{-8}	–
0.60 (Edinbugh: 0.66)	65	66	2.1×10^{-8}	2.1×10^{-8}
1.10	66	66	1.9×10^{-8}	1.4×10^{-8}
1.45 (Edinbugh: 1.50)	67	68	1.1×10^{-8}	1.0×10^{-8}

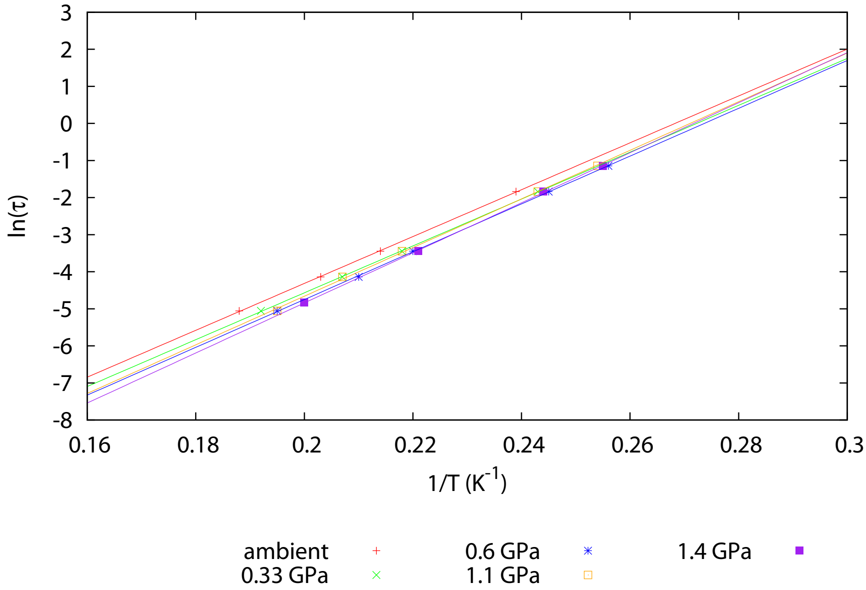

(a) Pseudo aligned single crystals sample

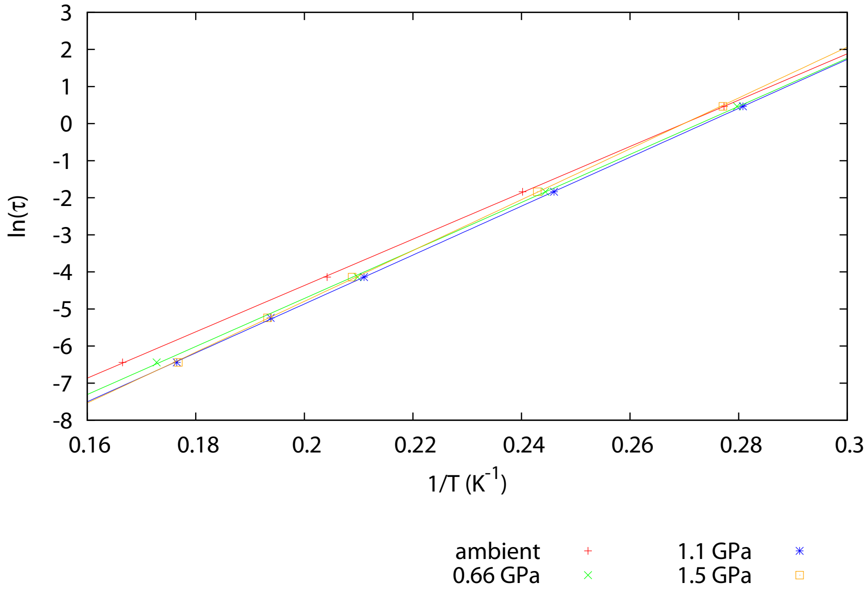

(b) Powdered sample

Figure 3.20: $\ln(\tau)$ vs $1/T$ at different pressures for the LT species. τ is given by $1/(2\pi\nu)$, with ν being the frequency at which the field was oscillating. The straight lines are the best fits to an Arhenius law, eq 2.5.

Novak *et al.*[77] reported an energy barrier of 64.1(7) K calculated from AC susceptibility data on complex **1** at ambient pressure. This is in agreement with our result. Murata *et al.*[74] reported an increase from 56.6 K to 58.5 K of the energy barrier between ambient pressure and 1 GPa. The energy barrier was estimated from the step at 0.9 GPa of the the hysteresis loop. Sieber *et al.*[78] also reported an increase of 2.1 % in the energy barrier up to 1.1 GPa using inelastic neutron scattering. Our data up to 1.1 GPa show a similar trend with a 4 % increase on both datasets.

However, the increase in the energy barrier is in conflict with the decrease of the out of phase peak temperatures. It is the same problem found on complex **2a** (Section 3.1.3) where changes in the energy barrier were not consistent with the changes in the out of phase AC susceptibility peaks temperature. For complex **2a**, changes were too small to conclude whether the energy barrier is decreasing or increasing. In this case, the temperature shift is significant (> 0.1°). The shoulder at 1.45 GPa clearly indicates the presence of a second HT species which compromises all the fitting at all pressures as this species could be present at lower pressure as well and not seen. The second HT species, even though not visible, can induce a shift in the temperature peak of the main HT species obtained from the fit.

The τ_0 value is decreasing for both pseudo aligned crystals and powdered experiments from 4×10^{-8} s-5×10^{-8} s at ambient pressure to 1×10^{-8} si at 1.4-1.5 GPa. Novak *et al.*[77] reported a value of $2.6(4)\times10^{-7}$ s using out of phase AC susceptibility measurements. Sessoli *et al.*[79] also reported a value of 2.1×10^{-7} s. Results on the τ_0 value are not consistent with the reported values. This may be caused by the low number of frequencies used for the fit.

Evolution of the energy barrier of the LT species

Interestingly, the height of the LT peaks is increasing from ambient pressure to 0.60 GPa (the height is almost four times more important at 0.60 GPa) while the height of the HT peak is decreasing (Figure 3.16). This suggests a conversion from the HT species to the LT species. This could be a tilting of the Jahn-Teller axis, a “vertical” elongated Jahn-Teller axis flipping to a “horizontal” elongated Jahn-Teller axis. Above 0.60 GPa, the LT peaks are disappearing. They are either going to lower temperature (and therefore not visible) or to higher temperature, which could explain the appearance of the second HT feature as a shoulder of the main HT peak.

In Table 3.14 the peak positions obtained by least-squares fitting the out-of-phase AC susceptibility peaks with Voigt profiles are listed for all pressures for the pseudo aligned crystals experiment.

Table 3.14: Out-of-phase Ac susceptibility results at different pressures of pseudo-aligned crystals of **1**

ac freq Hz	peak temp K	ln (τ) s	(peak temp)$^{-1}$ K^{-1}
	Ambient pressure		
1	1.958	−1.839	0.511
5	2.165	−3.447	0.462
10	2.251	−4.140	0.444
25	2.387	−5.057	0.419
	0.33 GPa		
1	1.976	−1.839	0.506
5	2.181	−3.447	0.458
10	2.270	−4.140	0.440
25	2.433	−5.057	0.411
	0.82 GPa		
1	1.854	−1.839	0.540
5	2.079	−3.447	0.481
10	2.173	−4.140	0.460
25	2.332	−5.057	0.429

Between ambient pressure and 0.33 GPa the peaks are shifted to higher temperature while at 0.82 GPa the peaks are shifted to lower temperature. This suggests an increase of the the energy barrier followed by a decrease of the energy barrier. The natural logarithm of the relaxation time as a function of the inverse temperature is shown in Figure 3.21. The energy barrier and relaxation time obtained from the least squares fit are summarised in Table 3.15.

Table 3.15: Evolution of the energy barrier and the relaxation of complex **1** from the pseudo aligned crystals experiment as a function of pressure

Pressure GPa	U K	τ_0 s
ambient	35	2.8×10^{-9}
0.33	34	5.0×10^{-9}
0.82	29	2.4×10^{-8}

Between ambient pressure and 0.82 GPa, the energy barrier decreases from 35 K to 29 K. However, this is not consistent with the out of phase AC susceptibility temperature peak position. Again, the lack of data points for the fitting of the energy barrier could be the

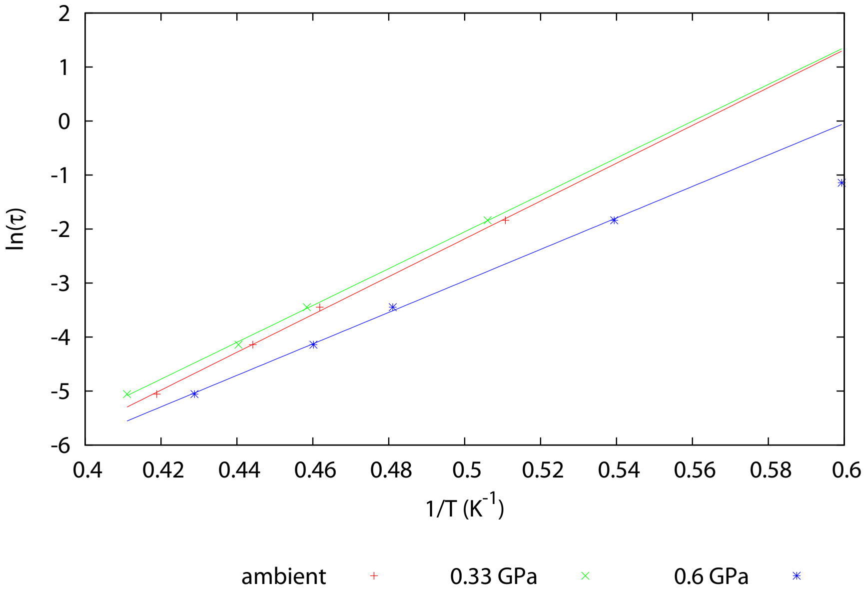

Figure 3.21: $\ln(\tau)$ vs $1/T$ at different pressures for the LT species. τ is given by $1/(2\pi\nu)$, with ν being the frequency at which the field was oscillating. The straight lines are the best fits to an Arhenius law, eq 2.5.

cause of the problem. In addition, the lack of data below 1.8 K is not favourable for a good estimation of the peak position.

Sieber *et al.*[78] reported the anisotropy of the fast relaxing species determined by inelastic neutron scattering with a value of 36.0 μeV at ambient pressure and 36.5 μeV at 0.5 GPa. However, no standard deviation on these values are available. Assuming a spin ground state of 10 (Hill *et al.*[70], Sieber *et al.*[78]), this gives an energy barrier of 41.8 K and 42.3 K respectively. They also reported an increase in the abundance of the fast relaxing species from 3.8 % to 11.1 %.

The increase in abundance of the LT species is consistent with the increase of the height of the peak in the out of phase AC susceptibility measurement in the same pressure range. However, changes in the energy barrier are in the opposite direction to our results. As both studies suffer from precision and inaccuracy, both are inconclusive about the changes in the energy barrier as a function of pressure.

The τ_0 value increases from 2.8×10^{-9} s to 2.4×10^{-8} s. No reference is available in the literature for high pressure experiments and taking into account the discussion on the energy barrier, these results should be used with care.

3.2.4 Hysteresis loop

The data have been collected and subtracted from their background as explained previously (Section 2.3.2). The resulting background is shown in Figure 3.22.

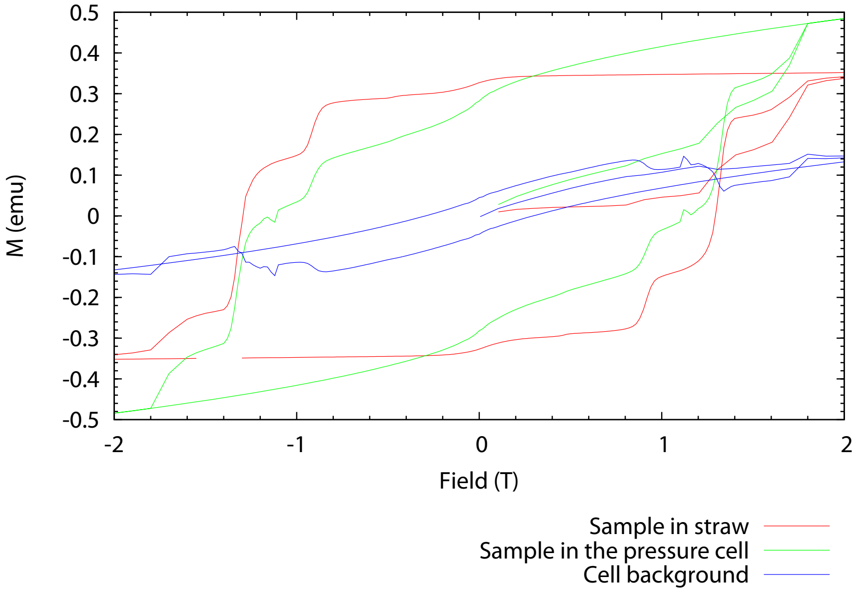

Figure 3.22: Hysteresis loop from raw data of **1** at ambient pressure outside and inside the pressure cell with the calculated background. Sample used was from Glasgow and composed of pseudo-aligned single crystals.

The fittings of all datasets are not very good using Equation 2.10 with the worst case at 1.45 GPa (Figure 3.23). Strong constraints on the slope A_i have been used: $[8, +\infty]$ and D has been restrained to values between 0.4 K and 0.7 K. The main problem is the spaces between the steps which are not equal. This indicates that the Hamiltonian used is not suitable and higher order terms need to be included. Cornia *et al.*[69] have confirmed the necessity of using the second and fourth-order terms in simulation of HF-EPR spectra. Unfortunately, using these parameters here is not possible as the model will become over parametrised.

As a consequence, the anisotropy has not been included in the model and only the coercive fields have been fitted using equation 2.12.

The background is very different from the background calculated for complex **2a**, see Figure 3.7. Even if the pressure cell is different, they should have a similar curves and sharp transitions are unlikely to happen (blue curve between 1 to 1.8 T in Figure 3.7). However, the background is relatively small compared to the signal from the sample which minimizes the impact.

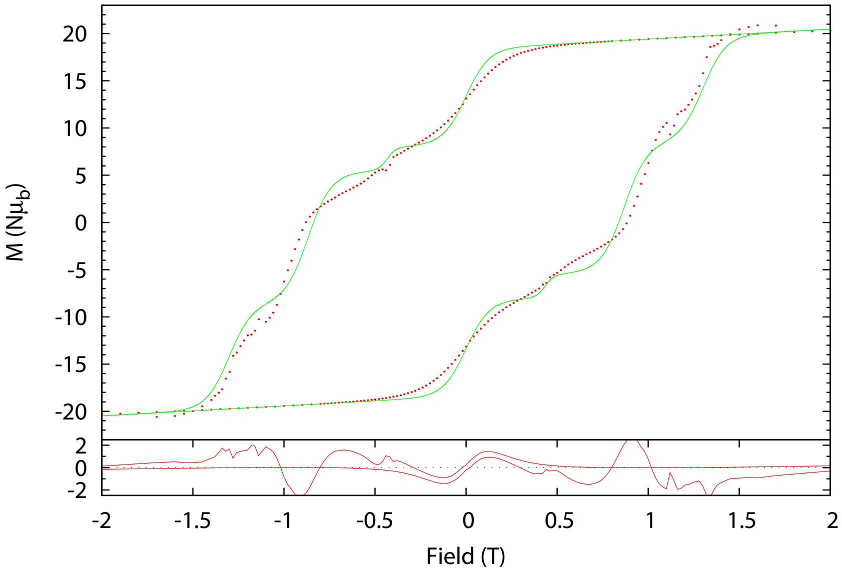

Figure 3.23: Hysteresis loop of **1** at 1.45 GPa and 2 K with the fit using equation 2.10 fit. Red dots are experimental data; the straight line is the fit. M is the molar magnetisation. The graph below is the difference between the data and the model.

The result of the fitting of hysteresis data at different pressures is reported in Table 3.16 and plotted in Figure 3.24 and Figure 3.25.

Under pressure, the four steps at 0, 0.45, 0.9 and 1.3 T are visible. The first step ($m + m' = 0$) coercive field decreases from 0.04 T to 0.00 T. Data acquisition at extremely low field is difficult to achieve and as the background removal involves three curves this means a standard deviation multiplied by three. Consequently, this deviation from 0 T can arise.

From ambient pressure to 1.45 GPa, coercive fields are 0.43, 0.54, 0.52, 0.44 and 0.46 T for the second step ($m + m' = -1$) which demonstrate no correlation with pressure. This could be due to the small contribution of this step to the curve *ie* in the order of magnitude of the noise, which makes the fitting extremely difficult.

The third step ($m + m' = -2$) increases from 0.92 T to 0.96 T (4 %) between ambient pressure and 1.45 GPa. By using equation 2.9 with $g = 1.9$,[11,74–76] an estimate of D has been made. At ambient pressure, $D = -0.587$ K and at 1.45 GPa, $D = -0.613$ K.

Murata *et al.*[74] reported a similar study on **1** under pressure up to 1.0 GPa using hysteresis loops at 2.4 K whereas our study was at 2 K. They used about ten single crystals manually oriented and fixed with a glue in a Teflon® capsule. The pressure cell was a CuBe pressure cell. They reported a small dependence on the step at 0.9 T with an increase of 3.5 %

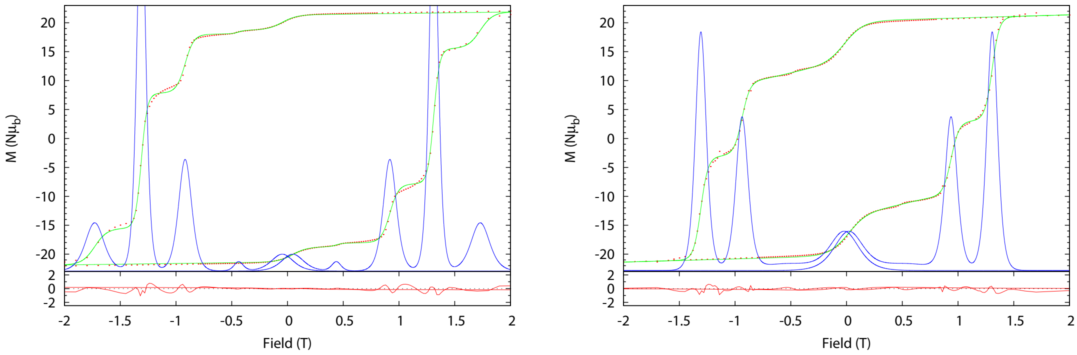

(a) ambient pressure

(b) 0.47 GPa

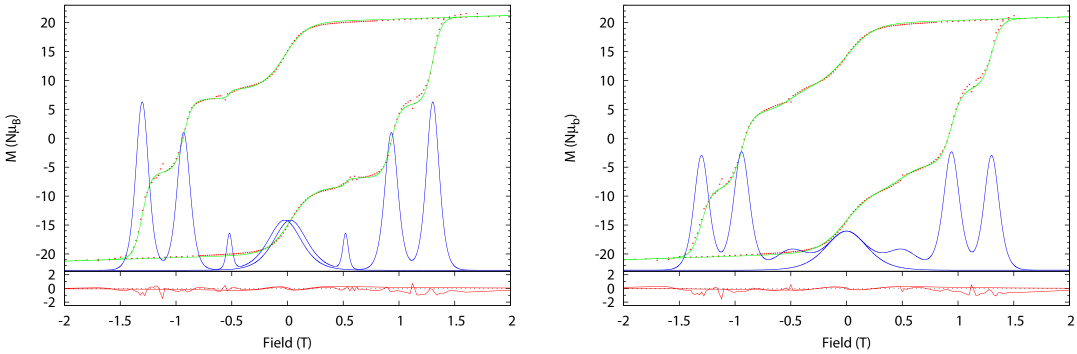

(c) 0.82 GPa

(d) 1.12 GPa

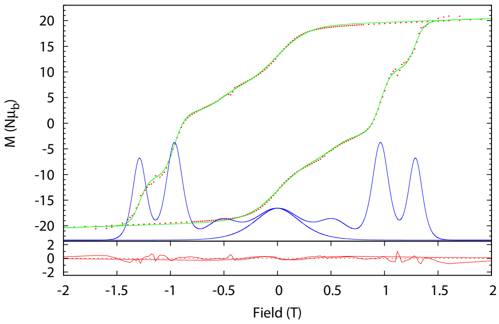

(e) 1.44 GPa

Figure 3.24: Hysteresis loop for **1** at 2 K and different pressures (pseudo aligned crystals sample). The green line is the best fit using Equation 2.12; the blue line is the derivative of the fit and the red dots are the experimental data. The ambient pressure hysteresis loop reported here was collected outside the pressure cell. The graph below is the difference between the model and the experimental data.

Table 3.16: Step parameters on the hysteresis loops of **1**. M_s^i is the height of a given step. The curvature is the slope at the inflexion point. H_0 is the coercive field at which the step occurred. H_0 is calculated from Equation 2.12.

Ambient pressure		
M_s^i M ($N\mu_B$)	Curvature	H_0 T
0.90	11.84	0.04
0	15.09	0.43
4.90	10.05	0.92
12.68	12.29	1.31
2.43	13.08	1.73

0.33 GPa		
M_s^i M ($N\mu_B$)	Curvature	H_0 T
4.08	5.50	0.03
0.72	6.72	0.54
6.56	13.28	0.94
8.92	15.40	1.31

0.6 GPa		
M_s^i M ($N\mu_B$)	Curvature	H_0 T
5.72	5.04	0.02
0.67	30.48	0.52
6.22	12.75	0.93
7.42	13.06	1.30

1.1 GPa		
M_s^i M ($N\mu_B$)	Curvature	H_0 T
5.39	4.14	0.00
2.03	5.33	0.50
6.44	10.51	0.94
5.89	11.19	1.30

1.45 GPa		
M_s^i M ($N\mu_B$)	Curvature	H_0 T
5.88	3.49	0.00
2.26	5.24	0.52
6.29	9.98	0.96
4.52	11.70	1.29

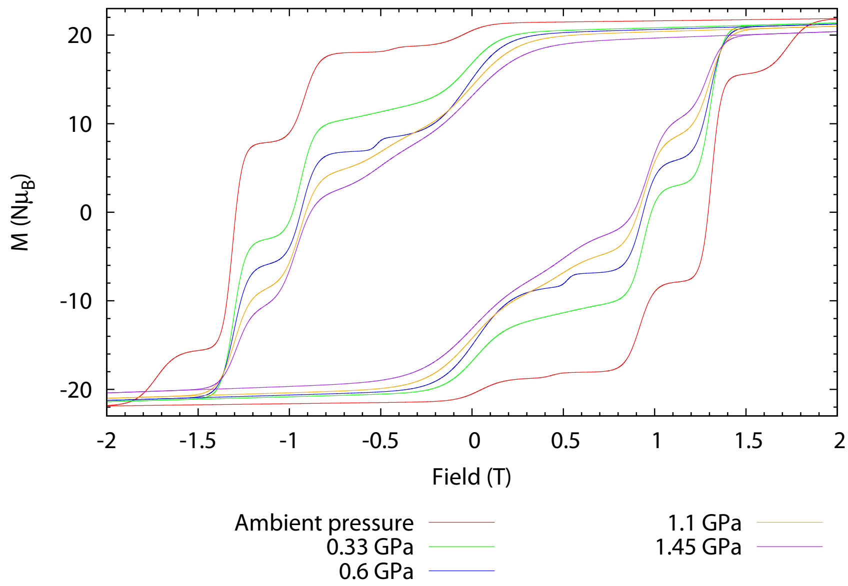

(a) Hysteresis loops

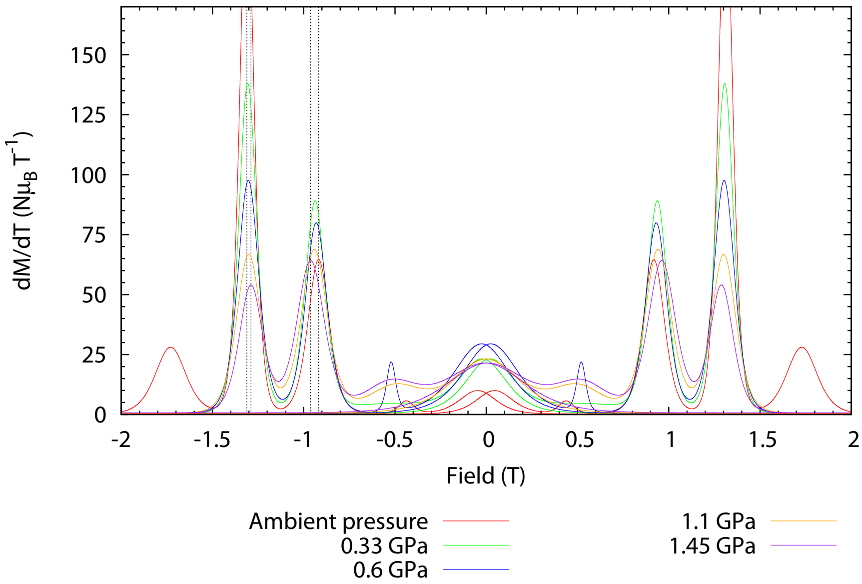

(b) Derivatives of the fit of the hysteresis loops. Vertical lines are the peaks position at ambient pressure and 145 GPa.

Figure 3.25: Fit of the hysteresis loops of **1** (pseudo aligned crystals) at 2 K using equation 2.12 and their derivatives between ambient pressure and 1.45 GPa.

in the coercive field which implies a increase in D from -0.566 K to -0.585 K (g = 1.9). Sieber *et al.*[78] also reported on **1** an increase of 2 % for D from $-0.0570(2)$ eV (-0.661 K) at ambient pressure to $-0.0582(4)$ eV (-0.675 K) at 1.2 GPa on the same complex using inelastic neutron scattering.

Our data in the same range of pressure (up to 1.1 GPa), show an increase of 2 % at 2 K in the coercive field (from 0.92 T to 0.94 T). The corresponding anisotropy increases from -0.587 K to -0.600 K. Because the temperature is not the same in both experiments, direct comparison is impossible (steps are temperature dependent[80]) but the trends are the same in the three studies.

The last step ($m + m' = -3$) decreases from 1.31 T to 1.29 T between ambient pressure and 1.45 GPa. Using Equation 2.9 with $g = 1.9$, -0.557 K was found for D at ambient pressure and -0.549 K at 1.45 GPa. This result is not consistent with the results from the third step at 0.9 T. As the anisotropy is an intrinsic property of the molecule, different values of D depending on the coercive field are not possible, thus Equation 2.9 is not suitable to extract D. Higher order terms of the Hamiltonian have been neglected and non equal spaces between the steps clearly indicate their necessity.[81,82] Changes between the steps suggest that higher orders could be pressure dependent. We also assumed that g is pressure independent as the value of g at high pressure is unknown. As a result it is not possible to conclude on the changes in the anisotropy.

3.2.5 High-Pressure Crystallography

The crystal structure of $[Mn_{12}O_{12}(MeCO_2)_{16}(H_2O)_4]\cdot 2\,CH_3COOH\cdot 4\,H_2O$ (**1**) was first determined by Lis[12] at ambient pressure and room temperature, and found to crystallise in the tetragonal space group I-4 (a = 17.319(9) Å and c = 12.388(7) Å). The unit cell contains two $[Mn_{12}O_{12}(MeCO_2)_{16}(H_2O)_4]$ molecules and each molecule has four solvent water molecules and two disordered acetic acid molecules of solvent. Cornia *et al.*[66] have also determined the structure at 83 K by single crystal X-ray diffraction. They found that the S_4 axis is disrupted by the disorder of the acetic acid over two sites (figure 3.26). As a result, six different isomers depending on the orientation of the acetic acid solvent molecules are possible[69] (Figure 3.27).

High pressure crystallography up to 2 GPa at ambient temperature revealed some modifications on the Jahn-Teller axis.[83] The projection angle of the single-ion anisotropy Mn(III) axis on the S_4 axis of Mn_{12} acetate decreases at higher pressures (Table 3.17 and

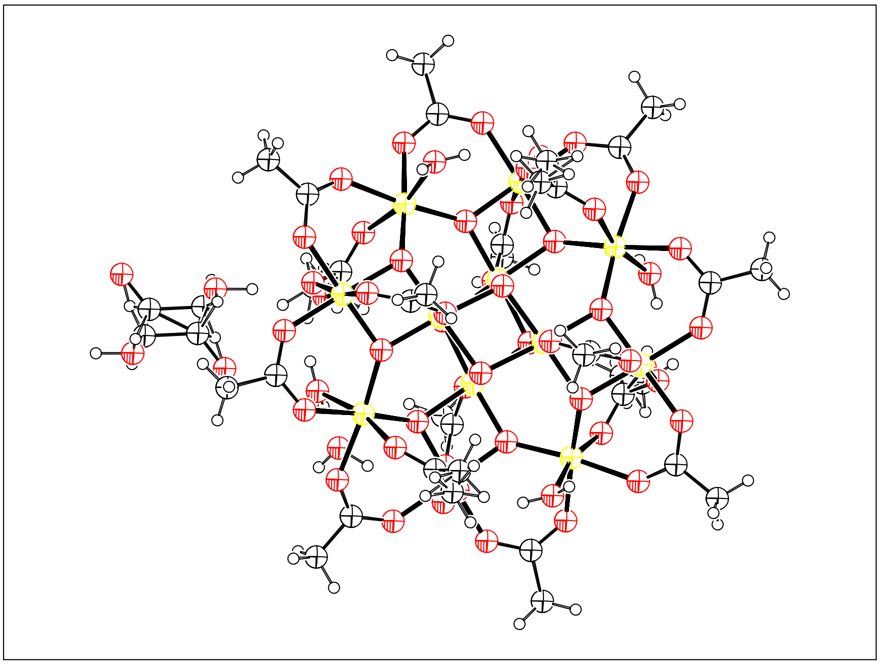

Figure 3.26: Ortep drawing of **1** at 83 K and ambient pressure.[66] The disordered acetic acid molecules are superimposed on the left. Mn are in yellow, O in red, C in white ellipsoids and H in white circles.

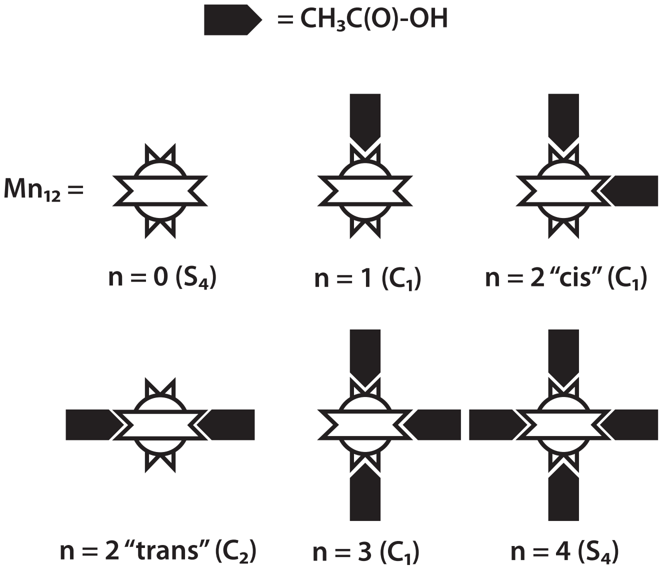

Figure 3.27: The six isomers of Mn_{12} acetate depending of the position of the acetic acid molecule. *n* is the number of acetic molecules making a hydrogen bond with the Mn_{12} molecule. Credits: Cornia *et al.*[69].

Figure 3.28). The decrease of the projection angle is consistent with an increase of the anisotropy.

Table 3.17: Projection angle of the single-ion anisotropy Mn(III) axes of **1** on the S_4 axis.

Pressure (GPa)	Site 1 Mn(2)	Site 2 Mn(1) H_2O ligand
0 (Lis)	11.602(6)°	35.835(7)°
0.05	10.918(60)°	35.753(65)°
0.25	10.739(67)°	35.814(86)°
1.25	9.160(57)°	36.279(73)°
2.06	9.166(77)°	34.992(117)°

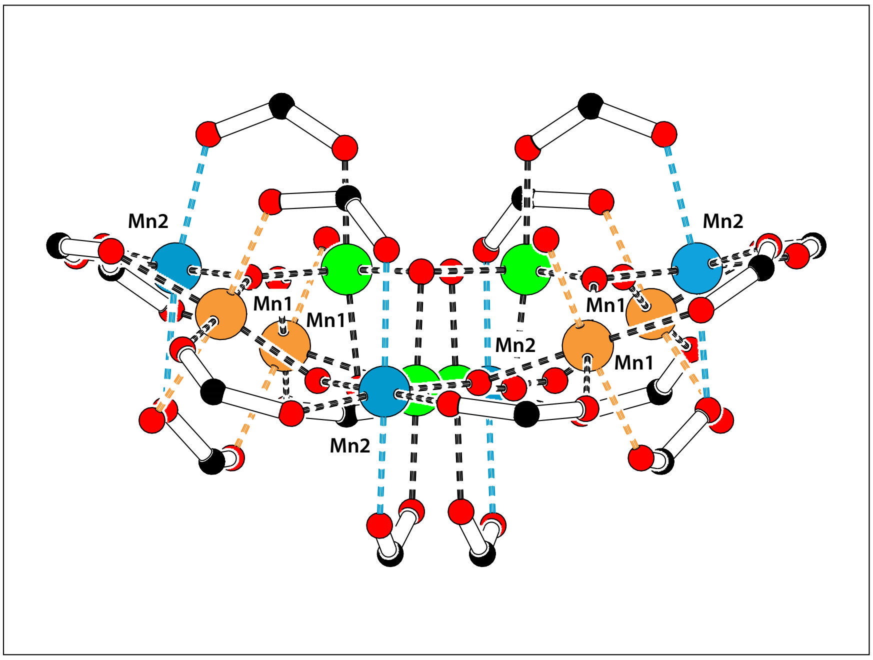

Figure 3.28: Highlight of the two Mn(III) sites of complex **1**. In blue, site 1 on Mn2; in orange, site 2 on Mn1. Mn(IV) are in green. O are in red and C in black. View along *a* axis.

3.3 Conclusion

Two Mn_{12} analogues have been studied, both revealed inconclusive results and interesting results. The pressure cell used for the magnetic experiments did not allow us to use frequencies higher than 20-30 Hz for the out of phase AC susceptibility measurements. The maximum pressure that can achieved is also rather low compared to the diamond Anvil cell used for crystallography.

On application of pressure on $[\mathrm{Mn_{12}O_{12}(O_2CCH_2Bu^t)_{16}(H_2O)_4}] \cdot \mathrm{MeNO_2} \cdot \mathrm{CH_2Cl_2}$ (**2a**), the main structural changes within the cluster occur at the Mn(III) centres. At 2.5 GPa, the elongated Jahn-Teller bonds at Mn8 switches to vertical Jahn-Teller bonds on Mn8-O14 and Mn8-O26. Between 1.5 and 2.5 GPa, most of the Jahn-Teller bonds on the remaining centres do not change significantly. Release of pressure re-establishes the coordination seen at ambient pressure. The difference of pressure obtained between the two experiments is not surprising as magnetic measurements were made below 10 K and the crystallography at ambient temperature.

At ambient pressure the formula unit contains $\mathrm{MeNO_2}$ and $\mathrm{CH_2Cl_2}$ of solvation. At 1.5 GPa the occupancies of the solvent model best with a combined total of 1.25 molecules per formula unit; the solvent was removed altogether in modelling the 2.5 GPa dataset. It appears that the solvent molecules are released into the fluid medium with pressure.

The AC susceptibility of **2a** was measured from ambient pressure to 1.44 GPa and the estimation of the energy barrier from the fit of the natural logarithm of the relaxation time as a function of the inverse temperature did not give reliable results except for the LT species of complex **2a**. Increasing the numbers of frequencies used might help increase the quality of the fit but a wider range range of frequency would be necessary to improve the quality of the fit.

However, AC susceptibility also shows conversion from the fast-relaxing to the slow-relaxing species. The ambient pressure data reveal only one peak at low temperature due to the fast-relaxing species. Between 0.47 GPa and 1.12 GPa the low temperature peak shifts to higher temperature with a significant decrease in its intensity. At the same time a broader peak appears at around 4 K. On reaching 1.44 GPa there is no low temperature peak, and only the high temperature peak is observed due to the exclusive presence of the slow-relaxing species. The hysteresis loops also show a conversion from the fast-relaxing to the slow-relaxing species with the opening of the hysteresis loop on application of pressure. The AC data and hysteresis loops data are in excellent agreement with the single-crystal X-ray diffraction study, where we have shown that the molecule becomes more axial with increasing pressure as the misaligned Jahn-Teller axis flips from horizontal to vertical. The pressure regime to see the full switch is slightly different between the two measurements, probably due to the diffraction study being carried out at ambient temperature whereas the magnetic study is carried out below 10 K.

Complex $[\mathrm{Mn_{12}O_{12}(MeCO_2)_{16}(H_2O)_4}] \cdot 2\,\mathrm{CH_3COOH} \cdot 4\,\mathrm{H_2O}$ (**1**) is more complicated.

At ambient pressure, the energy barrier calculates from the fit of the natural logarithm of the relaxation time as a function of the inverse temperature is in agreement with the literature[77] with a value of 63 K. At high pressure, a second LT species and a second HT species is clearly present making the calculation of the energy barrier difficult. On the HT species we reported an increase of the energy barrier from 63 K to 67 K which, is in the same order of magnitude from those reported.[74,78] Finally, the hysteresis loops revealed a pressure dependence of the quantum tunnelling steps at 0.9 T and 1.3 T. On the 0.9 T steps our results show the same trend as previous studies, with an increase of the *D* parameter.[74,78]

Chapter 4

1D-chains

The previous chapter was about molecular clusters. Their magnetic properties are very complex although the high magnetic response easily overcomes the pressure cell background. Chains have also a strong magnetic response when the magnetic centres are magnetically coupled along the chain. However, modelling their magnetic properties is easier with the Heisenberg model.

Chains and single-chain magnets appear to be a good compromise between complicated molecular clusters with a strong magnetic response and small molecules, which are easy to model but have a very weak magnetic response.

Two chains have been chosen: $[Gd(PhCOO)_3(DMF)]n$ and $[VO(salpropane)]_n$.

4.1 $[Gd(PhCOO)_3(DMF)]_n$

4.1.1 Synthesis

Benzoic acid (6 mmol) and NaOH (6 mmol) in methanol (15 mL) were stirred at room temperature for 30 min and a solution of $Gd(NO_3)_3 \cdot 6\,H_2O$ (2 mmol) in methanol (5 mL) was added. After 4 hours stirring at ambient temperature, the white precipitate was filtered and washed with methanol. The product was dissolved in hot dimethylformamide; colourless single crystals of $[Gd(PhCOO)_3(DMF)]_n$ (**3**) were obtained after a few days (Figure 4.1).

Figure 4.1: [Gd(PhCOO)$_3$(DMF)]$_n$ crystals.

4.1.2 High-Pressure Crystallography

High-pressure experiments were carried out as explained in Section 2.2. The conventional origin choice of the structure was moved from the centre of inversion to the −4 site, in order to compare the low and high pressure phases. The final conventional R-factor was 0.024 for 7016 reflections at ambient pressure (Table 4.1). Data were collected from 0.9 GPa up to a final pressure of 6.1 GPa. The numbering scheme used is the same as CSD refcode LUSCOR.[84] Listings of crystal and refinement data are given in Table 4.1.

4.1.3 Results and Discussion

The structure of 3 at ambient pressure

The crystal structure of **3** was first determined by Lam *et al.*[84], and found to crystallise in the tetragonal space group $P42/n$ (a = 22.583(1) Å and c = 9.2090(7) Å). The unit cell consists of four 1D chains oriented along the c-axis. Each chain comprises two crystallographically independent 8-coordinate Gd^{3+} centres bridged by benzoate ligands in either 1,3 or 1,1',3-modes, with one DMF molecule completing each coordination sphere.

Along the polymer chain, the distance between Gd centres alternates, the first distance (5.332 Å) is referred to here as the A-repeat, and corresponds to the distance between Gd centres bound between two 1,3-bridging benzoate ligands only (figure 4.2). The second repeat distance is much shorter (3.914 Å): the Gd centres are bridged by two 1,3-bridging

Table 4.1: Crystallographic data for single crystal diffraction study of **3** at increasing pressure.

Phase	Phase I	Phase I	Phase I	Phase I	Phase I
Pressure (GPa)	Ambient	0.10	0.55	1.18	1.67
Chemical formula	$C_{24}H_{22}GdNO_7$				
Space group	$P4_2/n$	$P4_2/n$	$P4_2/n$	$P4_2/n$	$P4_2/n$
T (K)	293	293	293	293	293
a (Å)	22.4915(6)	22.4953(9)	22.0678(4)	21.5853(2)	21.3751(2)
c (Å)	9.1640(3)	9.1830(6)	9.1203(3)	9.0434(1)	9.0087(1)
V (Å^3)	4635.77	4646.95	4441.47	4213.55	4116.03
Radiation type	Mo Kα	Synchrotron	Synchrotron	Synchrotron	Synchrotron
λ (Å)	0.71073	0.4767	0.4767	0.4767	0.4767
Refinement	$\lvert F\rvert^2$	$\lvert F\rvert^2$	$\lvert F\rvert^2$	$\lvert F\rvert^2$	$\lvert F\rvert^2$
Z, Z'	4, 0.5	4, 0.5	4, 0.5	4, 0.5	4, 0.5
R^a, $wR2^b$, S^c	0.024, 0.067, 1.05	0.054, 0.084, 0.93	0.073, 0.096, 1.03	0.057, 0.074, 1.02	0.046, 0.069, 0.93
No. of reflections	7016	2769	2805	2954	2827
No. of parameters	298	298	298	298	298

Phase	Phase I	Phase I	Phase I	Phase II	Phase II
Pressure (GPa)	2.65	3.20	3.73	5.01	6.10
Chemical formula	$C_{24}H_{22}GdNO_7$				
Space group	$P4_2/n$	$P4_2/n$	$P4_2/n$	$P-4$	$P-4$
T (K)	293	293	293	293	293
a (Å)	21.0414(2)	20.8918(2)	20.7490(3)	20.0734(2)	19.4090(8)
c (Å)	8.9513(1)	8.9248(2)	8.8988(2)	9.1385(1)	9.3837(3)
V (Å^3)	3963.1	3895.38	3831.12	3682.28	3534.94
Radiation type	Synchrotron	Synchrotron	Synchrotron	Synchrotron	Synchrotron
λ (Å)	0.4767	0.4767	0.4767	0.4767	0.4767
Refinement	$\lvert F\rvert^2$	$\lvert F\rvert^2$	$\lvert F\rvert^2$	$\lvert F\rvert^2$	$\lvert F\rvert^2$
Z, Z'	4, 0.5	4, 0.5	4, 0.5	4, 1	4, 1
R, $wR2$, S	0.036, 0.054, 0.93	0.039, 0.057, 0.91	0.032, 0.048, 1.12	0.051, 0.083, 0.95	–, – –
No. of reflections	2767	3017	2646	5867	–
No. of parameters	298	298	298	276	–

---

[a] $R = \sum \left| \lvert F_o\rvert - \lvert F_c\rvert \right| / \sum \lvert F_o\rvert$

[b] $wR2 = \sum w\left(F_o^2 - F_c^2\right)^2 / \sum w\left(F_o^2\right)^2$

[c] $S = \sqrt{\sum w\left({F_{hkl}^{o}}^2 - {F_{hkl}^{c}}^2\right) / (n-p)}$

and two 1,1',3-bridging benzoate ligands and this distance is referred to here as the B-repeat.

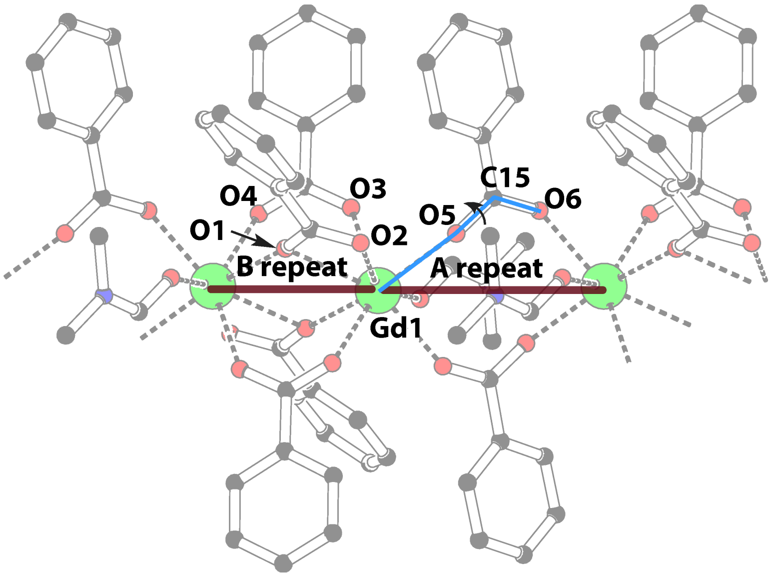

Figure 4.2: Gd environment. Gd are in green, O in red, N in blue and C in black.

Apart from Van der Waals forces, there are no intermolecular interactions; the shortest distance between polymer chains is between a methyl H-atom from the DMF ligand, and an adjacent phenyl group (D···A = 2.325 Å). The possibility for $\pi\cdots\pi$ interactions would seem probable from the number of benzoate ligands. However, the shortest distance between the centroids of the phenyl groups measures 4.890(2) Å and the dihedral angle between the two phenyls is 55.48(19)° under ambient conditions (Figure 4.3). Another possible interaction including aromatic rings is the CH···π interactions; however none of them are present below 3 Å. The five shortest interactions appearing under pressure are between 3.01 Å and 3.32 Å at ambient pressure. The shortest distance is between C14–H141 and Cg3* (Cg3* is the centroid of the C16* to C21* benzene ring; Figure 4.4). On increasing pressure, the structure of [Gd(PhCOO)$_3$(DMF)]$_n$ was found to be stable to 3.7 GPa. Above this pressure, the compound undergoes a single-crystal to single-crystal phase transition to a previously unknown high-pressure phase which we have designated [Gd(PhCOO)$_3$(DMF)]$_n$-II, referring to the previous phase as [Gd(PhCOO)$_3$(DMF)]$_n$-I. Plots showing changes in cell dimensions with increasing pressure are shown in Figure 4.5.

The response of [Gd(PhCOO)$_3$(DMF)]n–I to 3.7 GPa

On increasing pressure to 3.7 GPa, the greatest compression in the structure occurs within the *ab*-face, with an 8.1 % decrease in the length of the *a* and *b*-unit cell dimen-

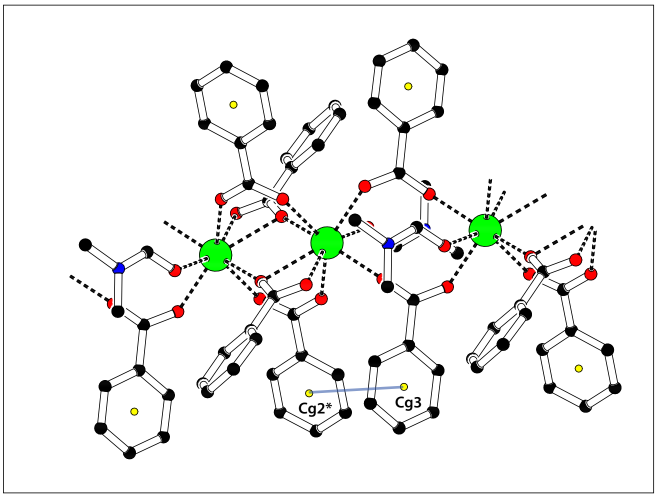

Figure 4.3: Shortest $\pi \cdots \pi$ distance on **3** at ambient pressure. Gd are in green, O in red, N in blue and C in black. View along *a*.

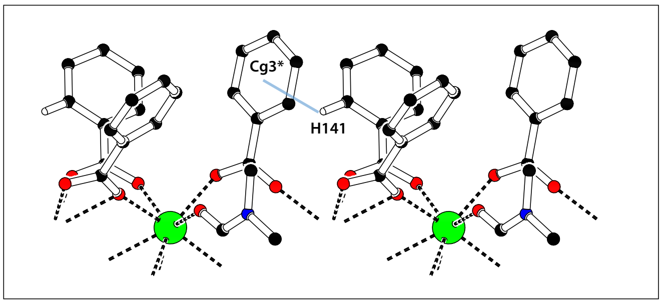

Figure 4.4: Shortest CH$\cdots\pi$ distance on **3** at ambient pressure. Gd are in green, O in red, N in blue and C in black. View along *a*

sions, while the c-axis reduces by only 3.4 %. A more substantial decrease in the length of the a and b-unit cell dimensions over c is unsurprising, as this results in the compression of weak intermolecular interactions (*e.g.* Van der Waals and CH$\cdots\pi$ interactions) which interact between the polymer chains, while any decrease in the length of the c-axis would result in a shortening of the polymer along its chemical backbone. Nevertheless, a decrease along the c-axis does occur, and is clearly represented by a decrease in distance between Gd centres along the c-axis, with the A and B-repeat Gd$\cdots$Gd distances decreasing by 0.185 and 0.047 Å respectively.

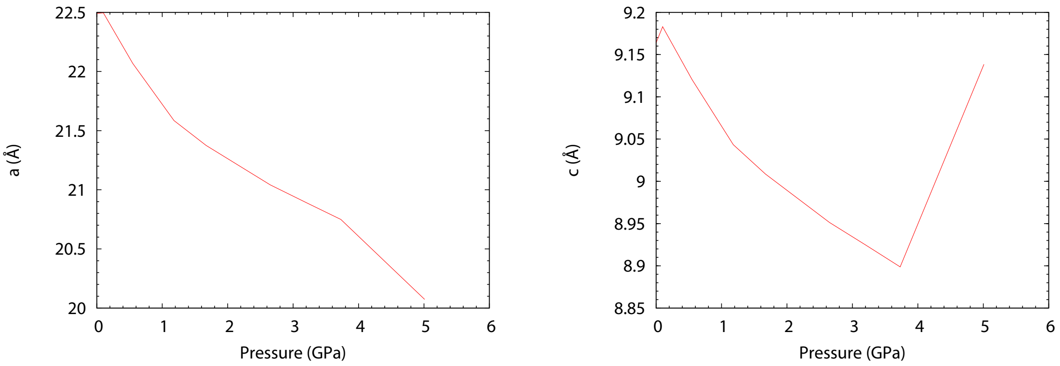

(a) a-axis (b) c-axis

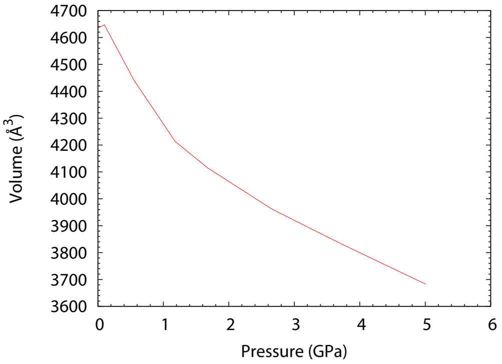

(c) Volume

Figure 4.5: Evolution of the cell parameters from ambient pressure to 5.1 GPa.

Effect of pressure on the intramolecular geometry During refinement of the single-crystal high-pressure data, all 1,2 and 1,3 distances on the benzoate and DMF ligands were restrained to their ambient pressure values. These restraints were applied, as bond lengths and angles of covalently bonded systems remain relatively unchanged within the pressure regime used here, while all torsion angles (which are much more susceptible to pressure) were allowed to refine freely.

These restraints, however, do not apply to metal-ligand bonds within metal organic com-

Table 4.2: Gd–O bond distances

Ambient pressure			3.7 GPa			5.4 GPa		
Atom1	Atom2	Å	Atom1	Atom2	Å	Atom1	Atom2	Å
Gd1	O1	2.318	Gd1	O1	2.298(3)	Gd1	O1	2.516(5)
Gd1	O1*	2.56	Gd1	O1*	2.436(3)	Gd1	O10	2.336(6)
Gd1	O2	2.485	Gd1	O2	2.509(4)	Gd1	O2	2.462(7)
Gd1	O3	2.386	Gd1	O3	2.367(3)	Gd1	O3	2.284(7)
Gd1	O4	2.36	Gd1	O4	2.372(3)	Gd1	O30	2.309(7)
Gd1	O5	2.337	Gd1	O5	2.307(3)	Gd1	O6	2.265(6)
Gd1	O6	2.289	Gd1	O6	2.259(3)	Gd1	O60	2.273(6)
Gd1	O7	2.402	Gd1	O7	2.371(3)	Gd1	O70	2.357(7)
–	–	–	–	–	–	Gd2	O1	2.293(5)
–	–	–	–	–	–	Gd2	O10	2.507(6)
–	–	–	–	–	–	Gd2	O20	2.501(7)
–	–	–	–	–	–	Gd2	O4	2.444(7)
–	–	–	–	–	–	Gd2	O40	2.343(7)
–	–	–	–	–	–	Gd2	O5	2.268(6)
–	–	–	–	–	–	Gd2	O50	2.294(6)
–	–	–	–	–	–	Gd2	O7	2.375(7)

plexes, as these have been previously observed using spectroscopic techniques to decrease or even increase with pressure within this pressure range. In this study, all metal-ligand bond distances and angles were therefore allowed to refine freely. On application of pressure to 3.7 GPa, statistically significant changes within the coordination sphere of the Gd^{3+} ion were observed, with the greatest change occurring along the Gd1–O1 bond which reduced in length by 0.124 Å (Table 4.2). This bond is between the metal ion and a carboxylate O-atom, which bridges the B-repeat. The oxygen atom O1 bridges two Gd centres and therefore forms a second Gd1–O1* bond which reduces by 0.020 Å and 0.12 Å respectively (Table 4.2). Of the two Gd1–O1/O1* bonds, it is the longer of the two that shows the greatest reduction in length. Counterintuitively, the Gd1–O2 bond between the metal ion and the other carboxylate O-atom from the same group actually increases by 0.024 Å.

On comparing the compressibility of the Gd1–O3 and Gd1–O4 bonds (the O-atoms from the 1,3 carboxylate bridging the B-repeat), Gd1–O3 decreases by only 0.019 Å while Gd1–O4 actually increases by 0.012 Å. It would appear that the small compression within the B-repeat (0.047 Å overall) is driven by the reduction in length of the Gd1–O1/O1* bonds.

A search of the CSD database using a Gd(III) ion, coordinated by eight O-atoms, gives 126 hits excluding powder diffraction data, disordered structures and all structures with a R-factor > 7.5 %. Refcode FITJAU gives the smallest Gd–O distance of the search with 2.219(7) Å, however the O-atom in this structure is linked to a phosphonate ligand. The next shortest distance is given by Refcode ZIRHUD with a value of 2.235 Å. This time, the oxygen involved is connected to a chloro-pyridine ligand. The frequency of occurence of Gd–O bonds as a function of distance drops off drastically below 2.26 Å with only seven hits. The minimum Gd–O distance in our complex at ambient pressure is Gd1–O6 (2.289 Å), which reduces to 2.259(3) Å at 3.7 GPa and remains the shortest Gd1–O bond. 2.26 Å appears to be a limit for this kind of bond in our structure as, in phase II, this bond increases to 2.265 Å. The other bonds remain in the average Gd–O bond length region around 2.40 ± 0.1 Å.

The second and third largest changes in the coordination environment of the Gd^{3+} ion occur along Gd1–O5 and Gd1–O6, the two bonds bridging the A-repeat, which both decrease by 0.036 Å and 0.032 Å respectively (Figure 4.2). The reduction in length of these bonds does not, however, explain the overall reduction in the distance between Gd centres along the A-repeat by 0.185 Å on increasing pressure to 3.7 GPa. On closer inspection, however, the ligand carboxylate group twists, resulting in a change in the Gd1–O5–C15–O6 torsion angle through the carboxylate group, which decreases, from −38.79° to −40.01° (Figure 4.2). Although this decrease is subtle, it allows the Gd centres along the A-repeat to move closer together. This twisting effect is responsible for the majority of the compression along the A-repeat, and indeed the *c*-axis, and allows the compression of the chain along its chemical backbone while preventing the decrease in length of the Gd1–O5 and Gd1–O6 bonds, which significantly are close to the shortest Gd–O bond lengths found in the CSD database.

Effect of pressure on the intermolecular geometry As mentioned previously, no classical H-bonding interactions can be observed between the polymer chains; however, several weak CH$\cdots\pi$ interactions are present (distances below the sum of Van der Waals radii plus 0.2 Å) which did not exist at ambient pressure. Six interactions are present at 3.7 GPa (Table 4.3 and Figure 4.6), ranging from 2.51 Å to 2.93 Å. These distances were between 3.01 Å and 3.32 Å at ambient pressure, giving a maximum difference of 0.5 Å. The previous $\pi\cdots\pi$ distance (Figure 4.3) reported above decreased to 4.504(2) Å.

A close intermolecular H–H contact appears between two carboxylate groups C3–H31$\cdots$H61*–C6*: the distance drops from 2.449 Å to 2.050 Å (Figure 4.7). This is the first limit to the compressibility of the structure. A search of the CSD for structures with a similar interaction between a hydrogen in the *meta* position of an aromatic carboxylate and a second hydrogen in the *ortho* position of an aromatic carboxylate results in 25 hits. In

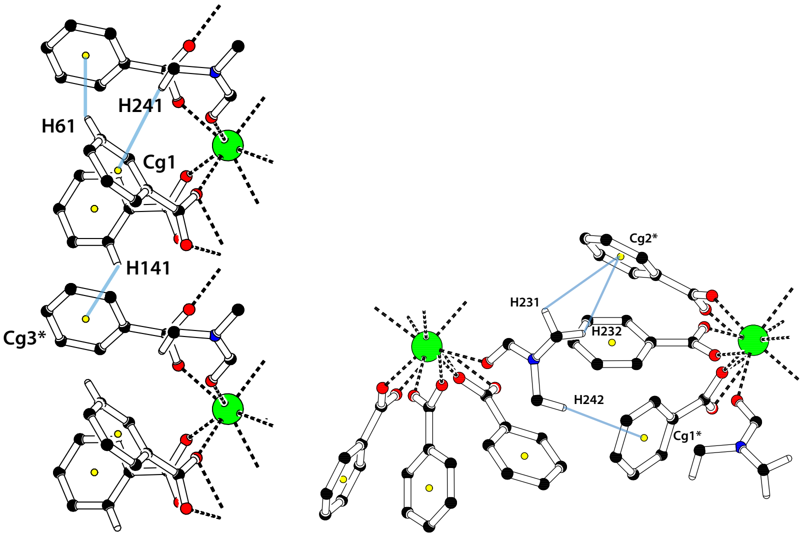

(a) View along *a* (b) View along *c*

Figure 4.6: CH···π interactions of **3** at 3.7 GPa. Gd are in green, O in red, N in blue and C in black.

Table 4.3: CH···π interactions at 3.7 GPa and the corresponding distances at ambient pressure. Cg is the centroid of the benzene ring. Cg1: C2→C7, Cg2: C9→C14, Cg3: C16→C21

Ambient pressure		3.7 GPa	
CH···Cg	Å	CH···Cg	Å
C14–H141···Cg3 (x, y, $-1+z$)	3.01	C14–H141···Cg3 (x,y,-1+z)	2.51
C6–H61···Cg3	3.22	C6–H61···Cg3	2.76
C23–H232···Cg2 (${}^{1}/_{2}+y$, ${}^{3}/_{2}-x$, ${}^{1}/_{2}+z$)	3.28	C23–H232···Cg2 (${}^{1}/_{2}+y$, ${}^{3}/_{2}-x$, ${}^{1}/_{2}+z$)	2.82
C24–H241···Cg1	3.32	C24–H241···Cg1	2.85
C24–H242···Cg1 (${}^{1}/_{2}+y$, ${}^{3}/_{2}-x$, ${}^{1}/_{2}+z$)	3.29	C24–H242···Cg1 (${}^{1}/_{2}+y$, ${}^{3}/_{2}-x$, ${}^{1}/_{2}+z$)	2.85
C23–H231···Cg2 (${}^{1}/_{2}+y$, ${}^{3}/_{2}-x$, ${}^{1}/_{2}+z$)	3.32	C23–H231···Cg2 (${}^{1}/_{2}+y$, ${}^{3}/_{2}-x$, ${}^{1}/_{2}+z$)	2.93

this search, the H–H distance has been constrained below the sum of the Van der Waals radii. Structures with disorder, errors, data from powder diffraction and structures with a R-factor above 5 % have been discarded. The minimum distances reported are 2.107 Å (CSD refcode: JIPMIF) and 2.200 Å (CSD refcode: PHOXSP). Hence, the $H_{ortho}\cdots H_{meta}$ distance of 2.107 Å is the smallest observed distance for this kind of interaction at ambient pressure. The JIPMIF structure is also a Gd(III) benzoate polymer, the only difference is the absence of a DMF ligand binding the Gd(III). Wood *et al.*[85] found that H···H distances do not compress below 1.7 Å and the frequency of H···H contacts as a function of distance drops off drastically between 1.9 Å and 1.7 Å. Hence, the single crystal to single crystal phase transition at higher pressure could be due to the short H31···H61* close contact (Figure 4.7), as this distance increases after the phase change.

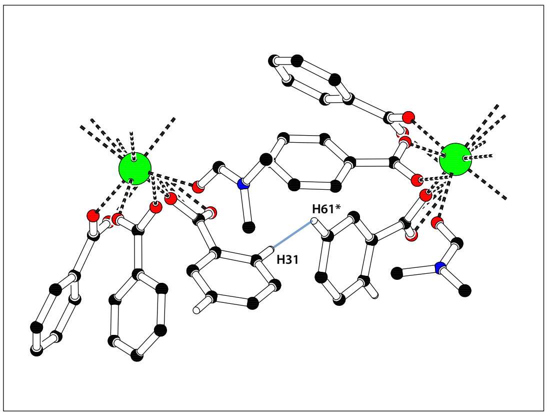

Figure 4.7: H31···H61* close contact of **3** at 3.7 GPa. Gd are in green, O in red, N in blue and C in black. View along *c*.

The structure of 3–II at 5.0 GPa

Between 3.7 GPa and 5.0 GPa, the crystal underwent a single-crystal to single-crystal phase transition from $P4_2/n$ to P-4 which we have designated $[Gd(PhCOO)_3(DMF)]_n$–II.

The cell parameter *a* decreased from 20.7490(3) Å to 20.0734(2) Å, and the cell volume from 3831.12(12) Å^3 to 3682.28(7) Å^3. However, the *c* parameter increased from 8.8988(2) Å to 9.1385(1) Å. The increase in the *c*-axis and the packing modification allows a better interpenetration of the chains and thus allows a higher packing density (see Figure 4.8).

The main change during the phase transition is the twisting of the ligand carboxylate group, resulting in a change in the Gd1–O50–C150–O60 torsion angle through the

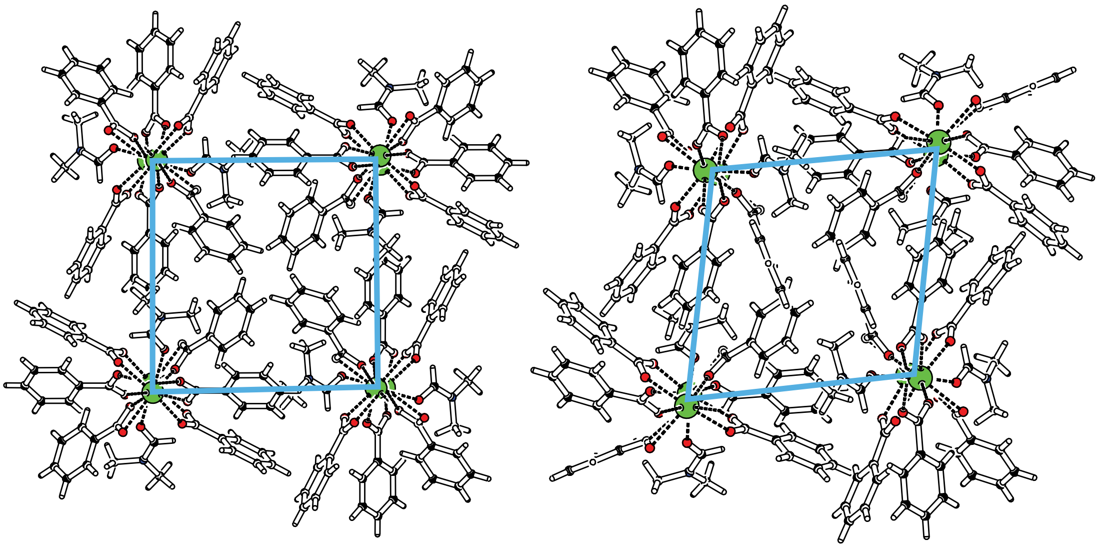

Figure 4.8: Evolution of the packing with pressure. Gd are in green, O in red, N in blue, C in black and H in white. View along the *c* axis.

carboxyl group which increases from −40.01° before the phase change to −7.84°. As a result, the interaction between the aromatic ring C102→C107 and C102*→C107* undergoes a transition from an edge to edge interaction (Figure 4.9) to an offset $\pi \cdots \pi$ stacking interaction (Figure 4.9). Hunter *et al.*[86] studied $\pi \cdots \pi$ interactions found in high resolution crystals structures of proteins from the protein structural relational database. He also calculated the energy of the interaction using three methods: the Allinger MM3 approach, his home made π-electron point charge model and the total energy of interaction from the sum of electrostatic energy and a Van der Waals' term. He found that face to face and edge to edge geometries are repulsive and were not observed in his population of crystal structures. Gould *et al.*[87] also studied $\pi \cdots \pi$ interactions present in phenylalanine structures from the CCDC database. They reported the frequency distribution of the interplanar angle, the distance between the two planes and the projection of distance between the centroids. They found a prominent result in the distribution. This result corresponds to parallel phenyl groups (interplanar angle below 5°), the distance between the phenyl groups is between 3.1 Å and 3.4 Å and the distance between the projection on the plane of the centroids centres are between 3.6 and 4.3 Å. The aromatic ring interaction between C102→C107 and C102*→C107* in our structure of $[Gd(PhCOO)_3(DMF)]_n$ at 5.0 GPa revealed an angle of 5° between the planes and a distance between the planes of 3.1 Å which is in agreement with the results observed by Gould *et al.*[87]. However the distance between the projection of the centroids is 2.1 Å in our structure compared to the 3.6-4.3 Å range in the Gould *et al.*[87] results.

Although the phase transition introduces a new attractive interaction, four close contacts (sum of the Van der Waals Radii minus 0.2 Å) are now present. Three of them are

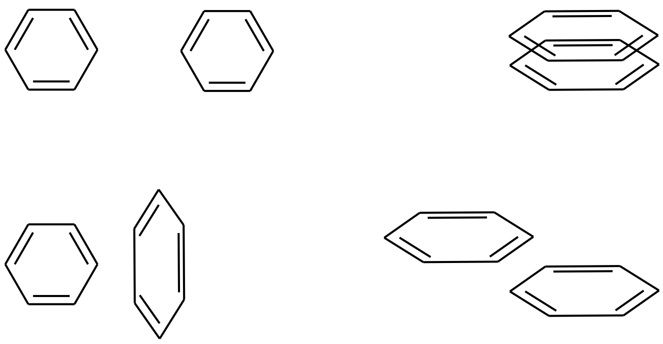

Figure 4.9: From left to right and top to bottom: edge to edge interaction, $\pi\cdots\pi$ stacking interaction, T-shaped interaction and offset $\pi\cdots\pi$ stacking interaction.

repulsive edge to edge aromatic interactions (Figure 4.9) with distances from 2.06 Å to 2.15 Å. The fourth one is between a hydrogen atom from a DMF ligand (H233) and an aromatic hydrogen (H2001) with a distance of 2.18 Å. Moreover, several CH$\cdots\pi$ interactions appeared, from six interactions at 3.7 GPa to ten interactions below 3 Å at 5.4 GPa (Table 4.4). The shortest interaction is now between H2303 and the phenyl group defined by C2* to C7* at 2.38 Å. Four other interactions are between a DMF molecule and a phenyl group. T-shaped aromatic interactions (Figure 4.9) are present with H31, H61, H141, H1301 and H1401. A search of the CSD database using two aromatic rings constrained by a distance between a hydrogen atom and the centroid of another phenyl group below 3 Å has been carried out. Structures with errors, disorder, powder diffraction data and structures with an R-factor above 5 % have been discarded. The search resulted in about 27000 hits. Excluding suspicious structures (FIWVOW, CIVMOJ10, FEBHAV...) the minimum distance is around 2.37 Å. Less than 50 of these hits have a CH$\cdots\pi$ interaction below 2.5 Å. Despite the high pressure, the T-shaped aromatic interactions found in $[Gd(PhCOO)_3(DMF)]_n$–II are all above 2.5 Å.

Table 4.4: CH···π interactions at 5.4 GPa. Cg is the centroïd of the benzene ring. Cg1: C2→C7, Cg2: C9→C14, Cg3: C16→C21, Cg4: C90→C140, Cg5: C102→C107, Cg6: C160→C210.

5.4 GPa CH···Cg	Å
C230–H2303···Cg1 ($-y, x, -1-z$)	2.38
C140–H1401···Cg6 ($x, y, 1+z$)	2.44
C6–H61···Cg3 ($x, y, 1+z$)	2.51
C14–H141···Cg3	2.69
C24–H242···Cg5 ($1-y, x, -z$)	2.73
C130–H1301···Cg4 ($y, 1-x, -z$)	2.83
C23–H232···Cg4 ($1-y, x, -z$)	2.86
C240–H2401···Cg2 ($-y, x, -1-z$)	2.88
C240–H2403···Cg2 ($-y, x, -1-z$)	2.90
C3–H31···Cg6 ($1-y, x, -1-z$)	2.97

4.2 [VO(salpropane)]$_n$

4.2.1 Synthesis

1,3-bis(N-salicylideneamino)propane

The tetradentate Schiff base ligand, 1,3-bis(N-salicylideneamino)propane abbreviated H_2salpropane (figure 4.10), was derived from salicylaldehyde (3.6 mL, 32 mmol) and 1,3–diaminopropane (16 mmol, 2 mL) in ethanol (50 mL).[88] A solution of salicylaldehyde (3.6 mL, 32 mmol) in ethanol (50 mL) was heated until the dissolution of the salicylaldehyde. Then, 1,3–diaminopropane (8 mmol, 1 mL) was added to the solution. The mixture was refluxed for half an hour and filtered while the solution is still hot. The solution was then concentrated in vacuo to a volume of about 10 mL. A large amount of diethyl-ether was added to the concentrated solution in order to improve the yield of the precipitation of the ligand. The ligand was recovered by filtration and dried in air. The ligand was used without any further purification.

Yield over 80 %. ^{1}**H NMR** (400 MHz, DMSO): 2.03 (t, 2H, CH_2) ; 3.69 (t, 4H, CH_2–N) ; 6.90 (t, 4H, $H_{aromatic}$) ; 7.33 (m, 2H, $H_{aromatic}$) ; 7.44 (m, 2H, $H_{aromatic}$) ; 8.59 (s, 2H, HC=N) ; 13.52 (s, 2H, OH). NMR spectra were recorded using a Bruker AV400 FT or DPX/400 spectrometer.

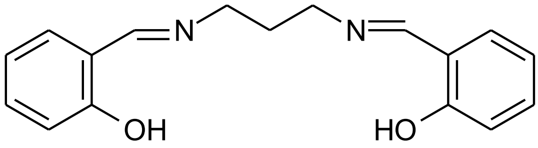

Figure 4.10: Salpropane ligand.

[VO(salpropane)]$_n$

[VO(salpropane)]$_n$ (**4**) (Figure 4.11) was prepared using the synthesis from Hughes *et al.*[89]. the VO(acac)$_2$ was analytical pure grade, purchased from Aldrich. VO(acac)$_2$ (430 mg, 1.6 mmol) was added to 50mL of acetonitrile. The mixture was heated to reflux for complete dissolution. The ligand was then added to the solution which was refluxed for 30 mins and then cooled to ambient temperature. A brown powder quickly precipitated. This was collected by filtration and the solid dissolved in a minimum volume of hot DMF. The solution was cooled very slowly and orange crystals (Figure 4.12) appeared in a few hours. Crystals were also obtained from a hot DMSO solution but the monomer [VO(salpropane)(DMSO)] was obtained instead of the polymer.[90]

Anal. Calcd: C, 58.80; H, 4.64; N, 8.01. Found: C, 58.35; H, 4.55; N, 8.12.

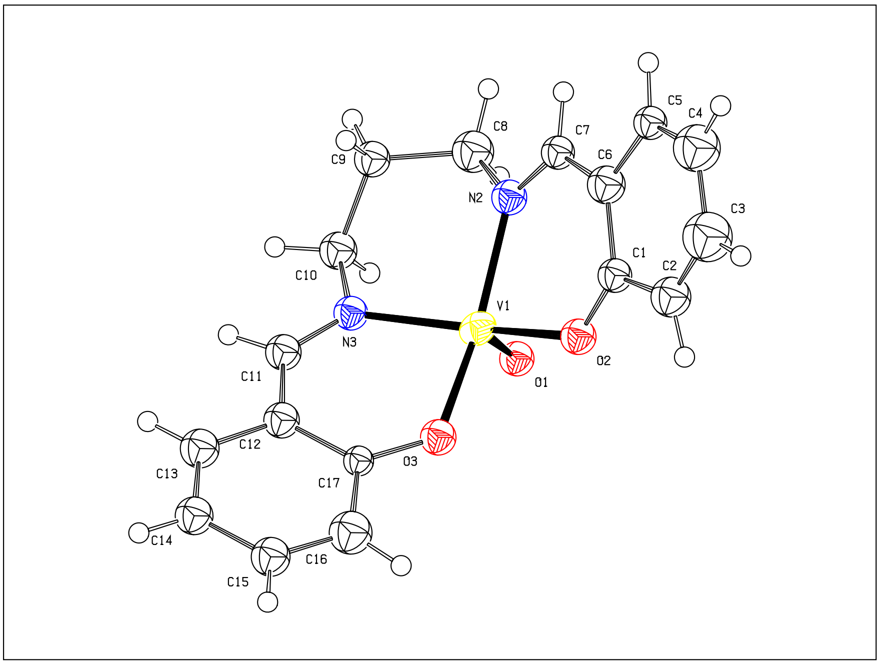

Figure 4.11: ORTEP drawing of **4** at 0.8 GPa. V is in yellow, O in red, N in blue, C in white ellipsoids and H in white circles.

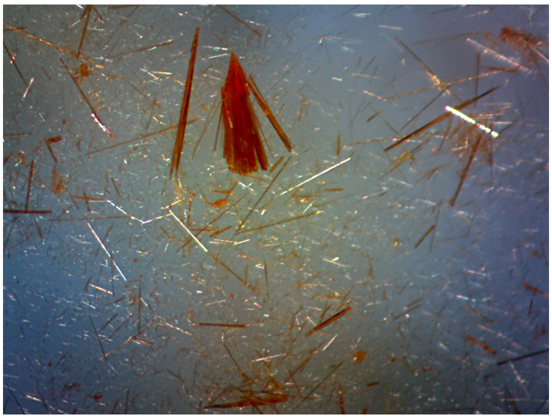

Figure 4.12: [VO(salpropane)]$_n$ crystals.

4.2.2 High-Pressure Crystallography

General Procedures

High-pressure experiments were carried out as explained in Section 2.2. The final conventional R-factor was 0.077 for 3080 reflections at ambient pressure (table 4.5). Data were collected from 0.8 GPa up to a final pressure of 4.6 GPa.

4.2.3 Results and Discussion

The structure of [VO(salpropane)]$_n$ at ambient pressure

The crystal structure of [VO(salpropane)]$_n$ was first determined by Mathew *et al.*[91], and found to crystallise in the orthorhombic space group $P\,2_12_12_1$. Although the $P\,2_12_12_1$ space group is a chiral space group, the structure is not chiral. The unit cell consists of two 1D chains oriented along the a-axis. The chains are formed by an alternation between a vanadium cation and an oxoanion. The chains are sited along a two fold screw axis. The vanadium is coordinated by two nitrogens and two oxygens from the ligand perpendicular to the axis of chain. One remaining coordination site is filled by an oxoanion (figure 4.11). The last remaining site is filled by an oxanion from the next asymmetric unit, thus creating the chain.

Along the polymer chain, the distance between the V centres is 3.7576(11) Å. The two axial V–O distances are 1.620(2) Å and 2.205(2) Å. The angles along the chains are

Table 4.5: Evolution of the parameters of **4** as a function of pressure.

Pressure (GPa)	ambient	0.8	1.4	2.1	2.5
Formula	$C_{17}H_{16}N_2O_3V$				
Space group	$P2_12_12_1$	$P2_12_12_1$	$P2_12_12_1$	$P2_12_12_1$	$P2_12_12_1$
T (K)	293	293	293	293	293
a (Å)	7.4925(3)	7.4631(8)	7.4577(4)	7.4386(11)	7.423(2)
b (Å)	11.7794(5)	11.496(4)	11.3902(15)	11.125(4)	10.945(16)
c (Å)	17.0517(7)	16.752(3)	16.6858(13)	16.496(3)	16.341(10)
Volume (Å^3)	1504.94(11)	1437.3(6)	1417.4(2)	1365.1(6)	1328(2)
Radiation type	Mo Kα	Synchrotron	Synchrotron	Synchrotron	Synchrotron
λ (Å)	0.71073	0.4767	0.4767	0.4767	0.4767
Refinement	$\|F\|^2$	$\|F\|^2$	$\|F\|^2$	$\|F\|^2$	$\|F\|^2$
Z	4	4	4	4	4
R^a, $wR2^b$, S^c	0.077, 0.045, 1.10	0.0715, 0.1979, 1.00	0.056, 0.137, 0.92	0.062, 0.153, 1.01	0.0585, 0.1250, 1.03
Reflections	3080	750	762	747	649
Parameters	209	99	99	99	99

Pressure (GPa)	3.2	3.4	3.8	4.6
Formula	$C_{17}H_{16}N_2O_3V$			
Space group	$P2_12_12_1$	$P2_12_12_1$	$P2_12_12_1$	$P2_12_12_1$
T (K)	293	293	293	293
a (Å)	7.396(5)	7.4015(16)	7.390(2)	7.3922(4)
b (Å)	10.74(2)	10.605(5)	10.579(7)	10.5146(14)
c (Å)	16.171(14)	16.125(5)	16.042(5)	16.0007(12)
Volume (Å^3)	1285(3)	1265.7(8)	1254.1(10)	1243.7(2)
Radiation type	Synchrotron	Synchrotron	Synchrotron	Synchrotron
λ (Å)	0.4767	0.4767	0.4767	0.4767
Refinement	$\|F\|^2$	$\|F\|^2$	$\|F\|^2$	$\|F\|^2$
Z	4	4	4	4
R, $wR2$, S	0.052, 0.117, 0.98	0.052, 0.106, 0.91	0.057, 0.106, 1.02	0.048, 0.108, 0.96
Reflections	621	681	645	686
Parameters	99	99	99	98

---

[a] $R = \sum \left| |F_o| - |F_c| \right| / \sum |F_o|$

[b] $wR2 = \sum w \left(F_o^2 - F_c^2\right)^2 / \sum w \left(F_o^2\right)^2$

[c] $S = \sqrt{\sum w \left({F_{hkl}^{o}}^2 - {F_{hkl}^{c}}^2\right) / (n - p)}$

formed by O1–V1–O1* with 167.75(14)° and V1–O1–V1* with 158.30(19)° which makes the chain slightly distorted (figure 4.13).

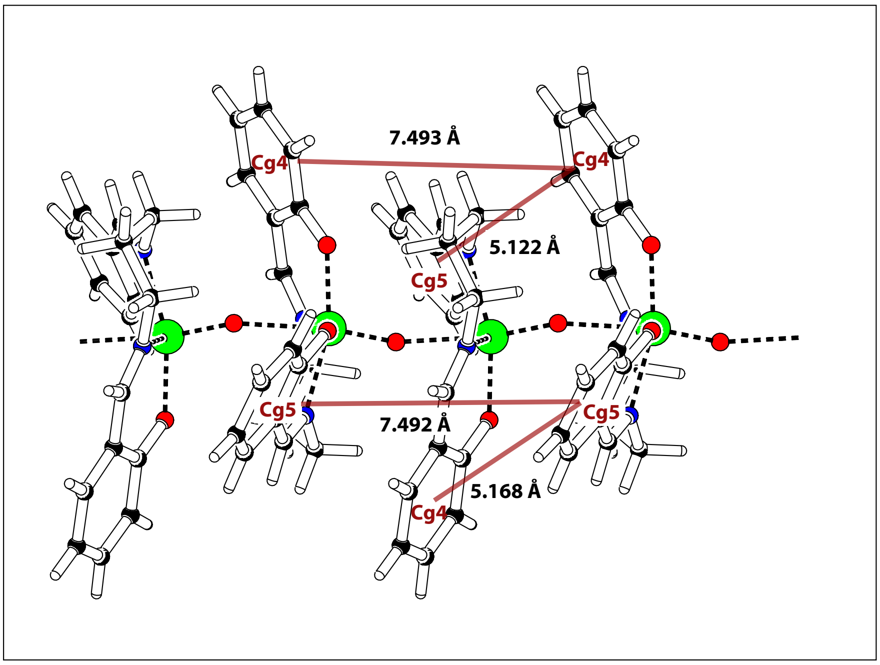

Figure 4.13: The chain of [VO(salpropane)]$_n$ at ambient pressure. Cg4 is the centroid from C1→C6 and Cg5 the centroid from C12→C17. V are in green, O in red, N in blue, C in black and H in white.

Apart from Van der Waals forces, there are no intermolecular interactions; the possibility for $\pi - \pi$ interactions would seem probable from the ligands but the shortest distance is 5.122(3) Å between Cg4 (C1→C6 centroid) and Cg5* (C12→C17 centroid). The phenyl groups from the ligand do not overlap with the next asymmetric unit but with the one after, which causes very long distances between aligned phenyl groups (figure 4.14).

The shortest interaction between polymer chains is between one phenyl hydrogen and one alkane hydrogen: H91···H51, 2.37 Å.

On increasing pressure, the structure of [VO(salpropane)]$_n$ was found to be stable to 4.6 GPa. Plots showing changes in cell dimensions with increasing pressure are shown in figure 4.15.

The response of [VO(salpropane)]$_n$ to 4.6 GPa

On increasing pressure to 4.6 GPa, the greatest compression in the structure occurs within the bc-face, with a 8.5 % decrease in the length of the b-unit cell dimensions

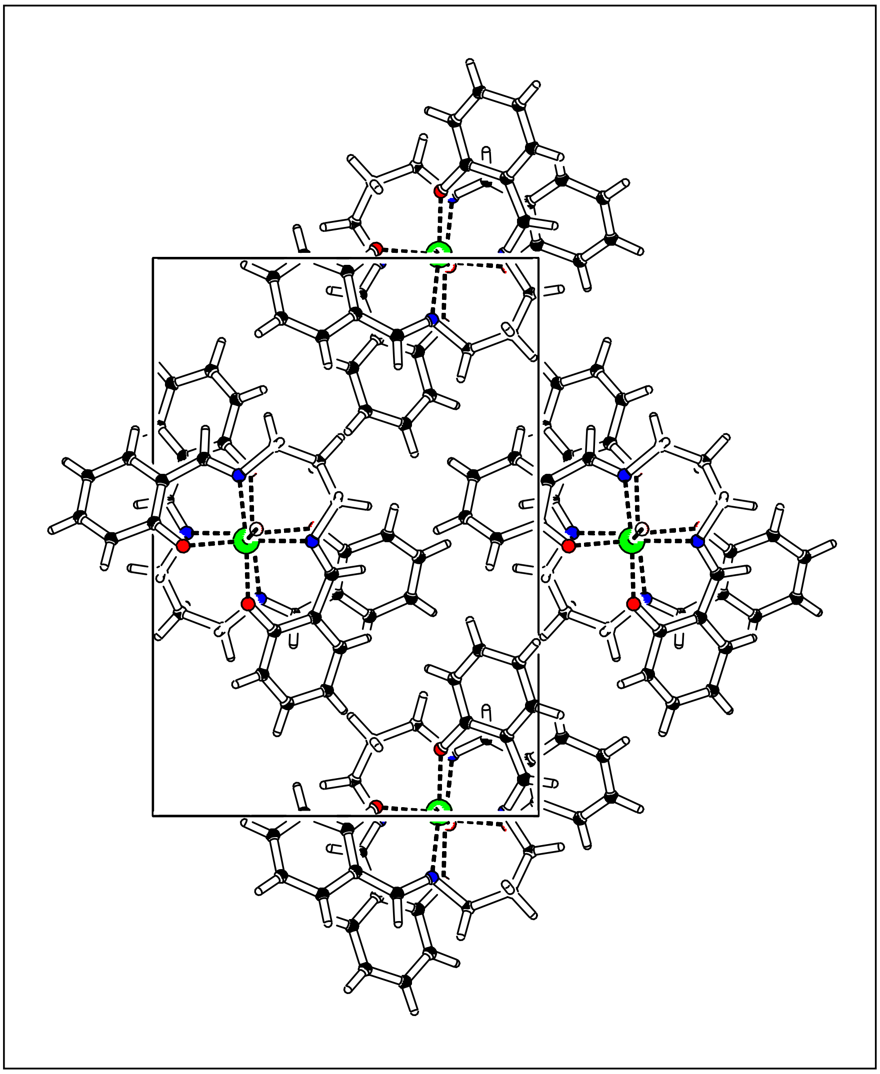

Figure 4.14: Packing of $[VO(salpropane)]_n$ within the *bc* face. V are in green, O in red, N in blue, C in black and H in white.

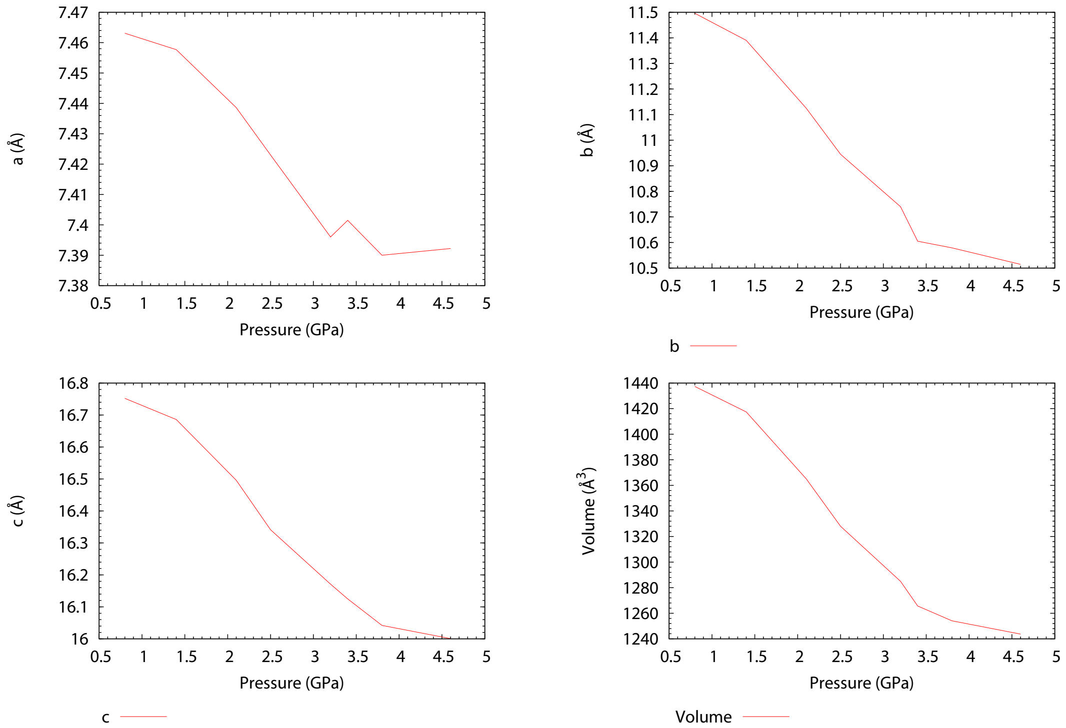

Figure 4.15: Evolution of cell parameters of **4** as a funtion of pressure.

and 4.5 % in the *c*-unit cell dimensions, while the *a*-axis reduces by only 1.3 % (see figure 4.15). A more substantial decrease in the length of the *b* and *c*-unit cell dimensions over *a* is unsurprising, as this results in the compression of weak intermolecular interactions (e.g. Van der Waals and $CH\cdots\pi$ interactions) between the polymer chains, while any decrease in the length of the *a*-axis would result in a shortening of the polymer along its chemical backbone. Nevertheless, a small decrease along the *a*-axis does occur, and is clearly represented by a decrease in distance between V centres along the *a*-axis, with the V···V* distance decreasing by 0.041(3) Å. The remaining reduction is observed on the V1–O1* long distance with a decrease from 2.205(2) Å at ambient pressure to 2.162 Å at 4.6 GPa. Surprisingly, the V1–O1 bond length has a small increase from 1.620(2) Å to 1.634(6) Å. The reduction in the *a* parameter is also consistent with a small decrease in the O1–V1–O* angle (1.7 %) and the V1-O1*–V1* angle (1.2 %).

Effect of pressure on the intermolecular geometry

As mentioned previously, no classical H-bonding interactions can be observed between the polymer chains; however, some weak $\pi\cdots\pi$ interactions inside the chains are present at ambient pressure. On increasing pressure, the distance between two adjacent centroids along the chains (Cg5···Cg4*) is increasing from 5.122(3) Å at ambient pressure to

5.278(5) Å at 4.6 GPa while the the other (Cg4···Cg5*) is decreasing from 5.168(3) Å at ambient pressure to 5.079(5) Å at 4.6 GPa (table 4.6 and figure 4.13).

Table 4.6: Evolution of the distance between the six membered rings in **4** as a function of pressure. Cg4 = C1→C6, Cg5 = C12→C17.

$\pi\cdots\pi$ distances	ambient pressure Å	4.6 GPa Å
Cg5···Cg4* ($^1/_2 + x$, $^{-3}/_2 - y$, $-1 - z$)	5.168(3)	5.079(5)
Cg4···Cg5* ($^1/_2 + x$, $^{-3}/_2 - y$, $-1 - z$)	5.122(3)	5.278(5)

On increasing pressure, the chains are close enough to generate H–H short contacts. Four of them are present at 4.6 GPa from 1.97 Å to 2.03 Å. The shortest distance is between H51 and H81* with a distance of 2.593 Å at ambient pressure to 1.97 Å at 4.6 GPa. The three other interactions between H31–H101*, H161–H131* and H31–H21* have a decrease in distance of 17.3 %, 18.3 % and 24.7 %, respectively. The values highlight the high compressibility of intermolecular voids compared to intra-molecular interactions.

4.3 Conclusion

The crystallographic study of $[Gd(PhCOO)_3(DMF)]_n$ as a function of pressure revealed a phase change via the twisting of a phenyl group. A short H···H contact between two phenyl groups of the chains induces the phase change. As a result, an inversion centre is lost and the space group goes from $P4_2/n$ to $P-4$. This could be the reason why no shorter contacts than the ambient pressure short contacts found in the CCDC database were seen.[40,92,93] The crystal would prefer to undergo major changes to avoid such contacts. However, the number of short contacts are more important in high pressure structures with four more of these in the $[Gd(PhCOO)_3(DMF)]_n$ complex and the $[VO(salpropane)]_n$ complex than in ambient pressure structures. In both complexes, there are only minor changes in the structure of backbone and this would produce very little change in the magnetic properties.

Therefore, a new approach could be investigated on a zigzag chain[15] for example $[Co(hfac)_2(NITPhOMe)]$ (hfac = hexafluoroacetylacetonate and NITPhOMe = 4'-methoxy-phenyl-4,4,5,5-tetramethylimidazoline-1-oxyl-3-oxide).[94] The zigzag chain would be more sensitive to high pressure.

Another approach is a polymerisation induced by pressure. Moggach *et al.*[95] reported a conversion of long intermolecular interactions into covalent bonds on [GuH][Cu_2(OH)(cit)$(Gu)_2$] (H_4cit = citric acid, Gu = guanidine and GuH = guanidinium cation). This should produce a significant change in the magnetic properties.

Chapter 5

Iron salen and iron chloride oxo-bridged complexes

Small molecules with two coupled metallic centres have several advantages. The magnetic properties are easier to model compare to the Mn_{12} acetate family. Any changes in the crystallography under pressure should be easier to correlate with the magnetic properties. This is because we can focus more easily on the bridging groups transmitting the magnetic interaction.

The magnetic properties of exchange coupled dinuclear complexes of transition metal ions are known to depend on the particular metal ions, the chemical nature of the bridging ligand, and the bridging geometries. However the situation is unclear and conflicting conclusions have been reported. Weihe and Güdel[96] published a magneto-structural correlation study of 32 μ-oxo-bridged iron(III) dimers. They conclude that there is a the dependence of the anti-ferromagnetic exchange parameter J on the Fe–O–Fe angle and the Fe–O distances. Mukherjee *et al.*[97] reported a slow decrease of J as the Fe–O–Fe angle decreases on the (μ-oxo)bis[trichloroferrate(III)] dianion. Gerloch *et al.*[98] expected a rapid decrease of J on the Fe–O–Fe angle decrease. On the contrary, it has also been reported that there is no correlation between J and the bridging angle.[99,100] The various number of molecules present in these studies make it difficult to attribute any change in the J value to purely structural factors when the chemical environment is different for every molecule.

As a result, we chose one oxo-bridged binuclear iron(III) Schiff-base complex and two (μ-oxo)bis[trichloroferrate(III)] complexes to follow the structural changes of the oxo-bridged iron(III) as a function of pressure.

5.1 $[N(PhCH_2)(CH_2CH_3)_3]_2[Fe_2OCl_6]$

5.1.1 Synthesis

A solution of $NaOCH_3$ (540 mg, 10 mmol in 60 mL of CH_3OH) was added dropwise over a period of 1 h to a solution of 1.62 g of $FeCl_3$ (10 mmol) in 40 mL of CH_3OH with rapid stirring. During the addition the reaction mixture changed from a light yellow color to deep brown. After the addition was complete, 0.5 mL of water was added and the reaction mixture was stirred for 1 h. The $(PhCH_2)(Et)_3NCl$ salt (2.3 g, 10 mmol) was then added to the mixture and stirred for half an hour.

The CH_3OH was removed using a rotary evaporator (the heating bath was maintained below 60° C) until a thick slurry was obtained. It is important not to take the mixture completely to dryness, a step that markedly decreases the final yield. To the slurry of crude product was added 80 mL of CH_3CN. The resulting cloudy brown suspension was stirred for 15 min and filtered. The filtrate was concentrated under vacuum to a volume of 5-10 mL and filtered again.

Red crystals of **5** (Figure 5.1) were obtained by vapour diffusion of diethyl ether into the previous CH_3CN solution. Yield above 60 %. IR spectroscopy (cm^{-1}; s = strong; m = medium; w = weak): 704 (s, cation); 752(s, cation); 864 (s, Fe–O–Fe); 1007 (m, cation); 1155 (m, cation); 1389 (m, cation); 1478 (m, cation); 2991 (w, impurity).

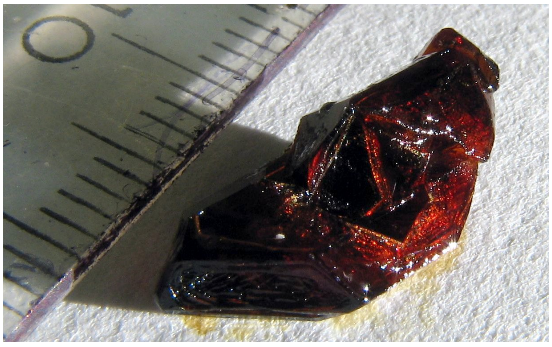

Figure 5.1: Crystals of **5**.

5.1.2 High-Pressure Crystallography

The final conventional R-factor was 0.036 (table 5.1). Data were collected from 0.46 GPa up to a final pressure of 5.06 GPa. Listings of crystal and refinement data are given in Table 5.1.

Table 5.1: Crystallographic data of **5** as a function of pressure.

Phase Pressure (GPa)	Phase I ambient	Phase I 0.46	Phase II 1.66	Phase III 2.82	Phase III 3.89	Phase III 5.06
Formula	$[N(CH_2Ph)(CH_2CH_3)_3]_2[Fe_2OCl_6]$					
Space group	*Pbca*	*Pbca*	*Pbca*	*Pbca*	*Pbca*	*Pbca*
T (K)	293	293	293	293	293	293
a (Å)	14.9893(8)	15.3136(3)	15.6466(6)	15.5622(8)	15.4651(5)	15.3416(13)
b (Å)	16.0245(8)	15.6327(6)	15.2793(11)	14.9921(12)	14.7987(9)	14.5791(17)
c (Å)	29.4593(15)	28.4228(10)	25.3429(18)	24.618(2)	24.2234(16)	23.788(3)
Volume (Å^3)	7076.0(6)	6804.2(4)	6058.7(7)	5743.6(7)	5543.9(5)	5320.6(10)
Radiation type	Mo Kα	Synchrotron	Synchrotron	Synchrotron	Synchrotron	Synchrotron
λ (Å)	0.71073	0.4767	0.4767	0.4767	0.4767	0.4767
Refinement	$\|F\|^2$	$\|F\|^2$	$\|F\|^2$	$\|F\|^2$	$\|F\|^2$	$\|F\|^2$
Z	8	8	8	8	8	8
R^a, $wR2^b$, S^c	0.036, 0.135, 1.00	0.040, 0.100, 0.96	0.049, 0.135, 0.96	0.047, 0.136, 0.90	0.050, 0.143, 1.00	0.054, 0.155 0.96
Reflections	9018	5696	4976	4647	4554	3911
Parameters	334	334	334	334	334	334

$^aR = \sum \big| |F_o| - |F_c| \big| / \sum |F_o|$

$^bwR2 = \sum w \left(F_o^2 - F_c^2\right)^2 / \sum w \left(F_o^2\right)^2$

$^cS = \sqrt{\sum w \left({F_{hkl}^{o}}^2 - {F_{hkl}^{c}}^2\right) / (n-p)}$

5.1.3 Results and Discussion

The structure of $[N(CH_2Ph)(CH_2CH_3)_3]_2[Fe_2OCl_6]$ at ambient pressure

The crystal structure of $[N(CH_2Ph)(CH_2CH_3)_3]_2[Fe_2OCl_6]$ (**5**) was first determined by Haselhorst *et al.* [101], and found to crystallise in the orthorhombic space group *Pbca*. The unit cell consists of one $[Fe_2OCl_6]^{2-}$ anion with two $[N(CH_2Ph)(CH_2CH_3)_3]^+$ cations (Figure 5.2). The two iron centres are tetrahedral and bridged together by an oxo ligand, the remaining coordination sites are filled with chloride ligands.

Apart from Van der Waals forces, the only intermolecular interaction involving the $[Fe_2OCl_6]^{2-}$ anion is a short Cl···H contact between H212 and Cl12 with a distance of 2.740 Å. Two $\pi\cdots\pi$ stacking interactions are present between the cations with a distance between 5.395(4) Å and 5.568(4) Å (Figure 5.3). There is also a CH···π interaction

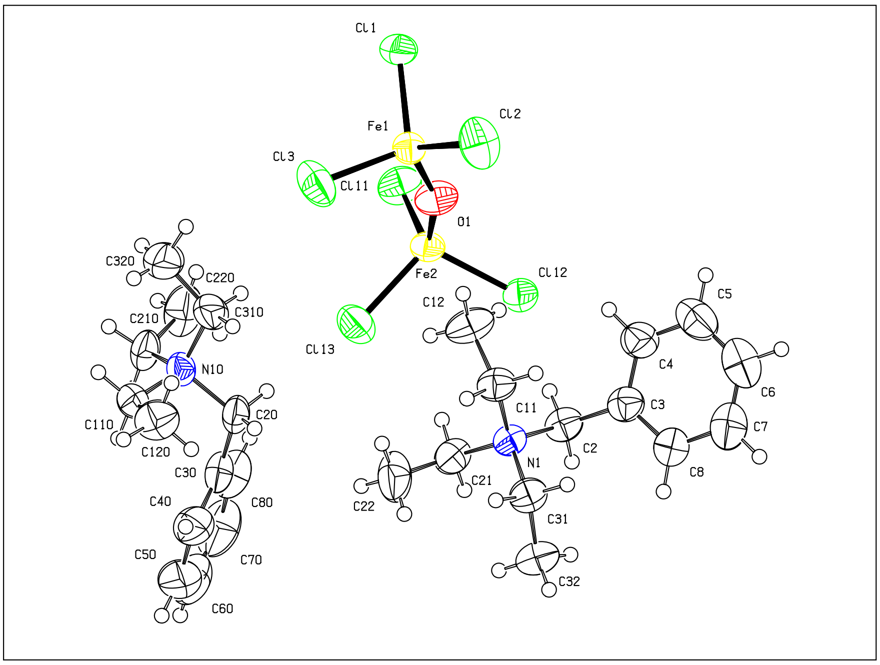

Figure 5.2: ORTEP drawing of **5** at ambient pressure. Fe are in yellow, Cl in green, O in red, N in blue, C in white ellipsoids and H in white circles.

between H701* (x, $3/2 - y$, $-1/2 + z$) and cg2 (C30→C80). The angle between the two plane cg1 (C3→C8) and cg2* is 79.1(3)° and the CH$\cdots\pi$ distance is 3.021 Å (Figure 5.3).

On increasing pressure, the structure of **5** was found to be stable to 0.46 GPa. Above this pressure, the compound underwent a single-crystal to single-crystal phase transition to a previously unknown high-pressure phase which we have designated $[N(CH_2Ph)(CH_2CH_3)_3]_2[Fe_2OCl_6]$–II, referring to the previous phase as $[N(CH_2Ph)(CH_2CH_3)_3]_2[Fe_2OCl_6]$–I. Above 1.66 GPa, **5**–II underwent a single-crystal to single-crystal phase transition to a previously unknown high-pressure phase which we have designated $[N(CH_2Ph)(CH_2CH_3)_3]_2[Fe_2OCl_6]$–III. The evolution of the cell parameters on increasing pressure is shown in Figure 5.4.

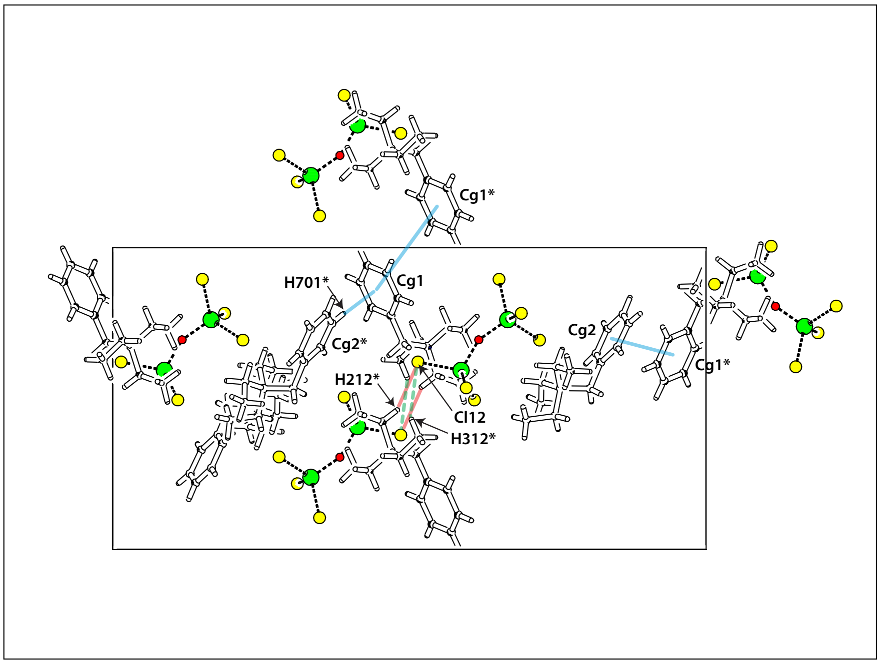

Figure 5.3: $\pi \cdots \pi$, CH$\cdots\pi$ and Cl$\cdots$H interactions of **5** at ambient pressure (blue and red lines) and at 0.46 GPa (straight lines and dashed lines). Fe are in green, Cl in yellow, O in red, N in blue, C in black and H in white. View along *b*-axis.

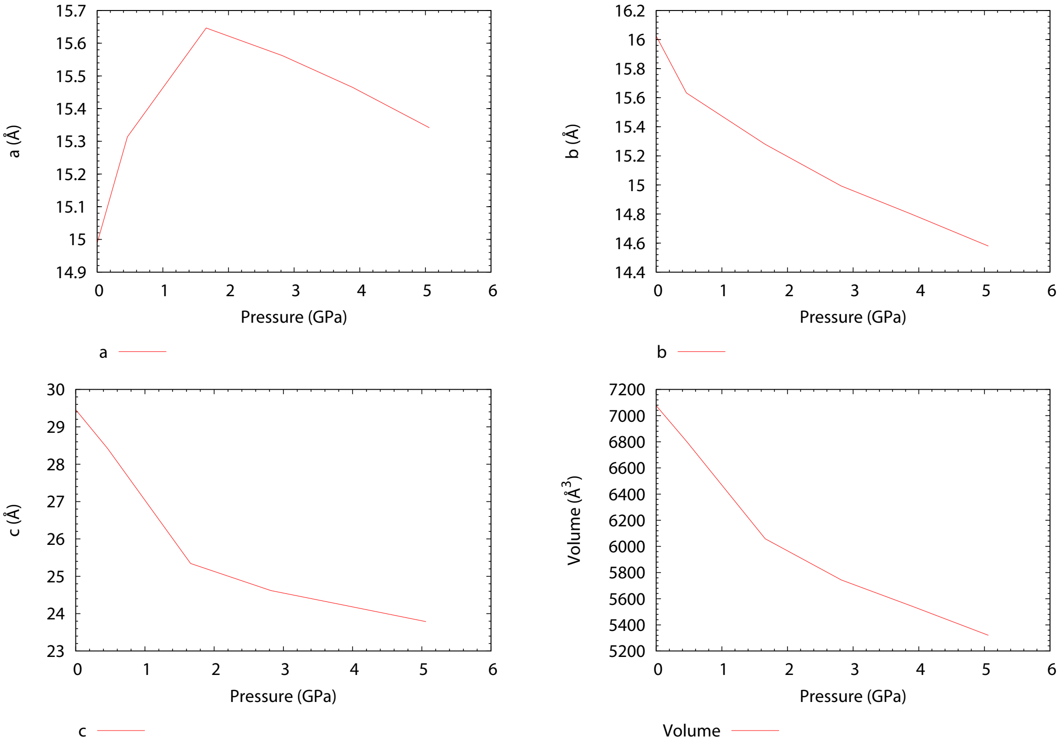

Figure 5.4: Evolution of cell parameters of **5** as a function of pressure.

The response of $[N(CH_2Ph)(CH_2CH_3)_3]_2[Fe_2OCl_6]$-I to 0.46 GPa.

On increasing pressure to 0.46 GPa, the greatest compression in the structure occurs within the *bc*-face, with a 2.4 % decrease and a 3.5 % decrease in the length of the *b* and *c*-unit cell dimensions respectively, while, surprisingly, the *a*-axis increases by 2.2 % (Figure 5.4).

The bond lengths do not change very much in this pressure range, the biggest change is the Fe2−Cl13 bond which increases from 2.2262(17) Å to 2.2399(14) Å (0.6 % increase). The change is very small but statistically significant. Fe1−Cl3 also increases from 2.2038(19) Å to 2.2121(15) Å (0.4 % increase). All remaining bonds do not change significantly (Table 5.2). However the Fe1−*O*−Fe2 angle increases from 154.8(2)° to 162.65(19)°. This is an important change which is likely modify the magnetic properties (Section 5.4).

Table 5.2: Evolution of selected bonds length of **5** as a function of pressure.

Phase Pressure (GPa)	Phase I ambient Å	Phase I 0.46 GPa Å	Phase II 1.66 GPa Å	Phase III 2.82 GPa Å	Phase III 3.89 GPa Å	Phase III 5.06 GPa Å
Fe1−O1	1.753(3)	1.751(3)	1.760(4)	1.754(4)	1.769(4)	1.754(5)
Fe2−O1	1.754(3)	1.751(3)	1.757(4)	1.763(4)	1.748(4)	1.755(5)
Fe1−Cl1	2.2210(16)	2.2232(15)	2.221(2)	2.216(2)	2.218(2)	2.216(2)
Fe1−Cl2	2.2108(17)	2.2128(13)	2.2196(17)	2.2193(17)	2.2153(17)	2.213(2)
Fe1−Cl3	2.2038(19)	2.2121(15)	2.201(2)	2.199(2)	2.205(2)	2.200(2)
Fe2−Cl11	2.2059(16)	2.2088(15)	2.209(2)	2.2063(18)	2.204(2)	2.195(2)
Fe2−Cl12	2.2290(13)	2.2258(13)	2.223(2)	2.220(2)	2.217(2)	2.218(2)
Fe2−Cl13	2.2262(17)	2.2399(14)	2.211(2)	2.2083(18)	2.202(2)	2.196(2)

In terms of inter-molecular interactions, two close contacts are present between the iron dimer and the cation: H212···Cl12, which has been also reported at ambient pressure (Section 5.1.3) and H312···Cl12 with distances of 2.710 Å and 2.700 Å, respectively. The CH···π interaction between H701 and the centroid of C3→C8 decreases to a distance of 2.87 Å. $\pi \cdots \pi$ stacking interactions are still present (Figure 5.3), one of them has decreased as we would expect under pressure, but the second increases from 5.395 Å to 5.603 Å (Cg1···Cg1* with Cg1 the benzene ring defined by C3→C8). The increase in the *a* parameter can be explained by the increase of the $\pi \cdots \pi$ stacking interactions between Cg1 and Cg1* $(2 - x, 1 - y, 1 - z)$, as they all lie along the *a*-axis.

The structure of $[N(CH_2Ph)(CH_2CH_3)_3]_2[Fe_2OCl_6]$–II at 1.66 GPa

Between 0.46 GPa and 1.66 GPa, **5**–I underwent a single-crystal to single-crystal phase transition. The space group stays the same: *Pbca*. The *b* and *c* parameters continue to decrease with a 2.3 % and 10.8 % decrease, respectively. The *a* parameter is still increasing (by 2.2 %). The huge drop in the *c* parameter is the first consequence of the phase change.

Bonds lengths still remain similar, within the standard deviation, but the Fe1–*O*–Fe2 angle is decreasing from 162.65(19)° at 0.46 GPa to 159.0(3)° at 1.66 GPa following a previous increase from 154.8(2)° to 162.65(19)° (Table 5.3).

Table 5.3: Evolution of selected angles of **5** as a function of pressure.

Phase Angle	Phase I ambient	Phase I 0.46 GPa	Phase II 1.66 GPa	Phase III 2.82 GPa	Phase III 3.89 GPa	Phase III 5.06 GPa
Fe1–O1–Fe2	154.8(2)	162.65(19)	159.0(3)	159.0(3)	159.2(3)	159.9(3)

There is also a change in the configuration of the chloride ligands. At ambient pressure, the chlorides were not totally eclipsed when viewed along Fe1–Fe2. However, at 1.66 GPa, two of the chlorides are fully eclipsed as shown in Figure 5.5.

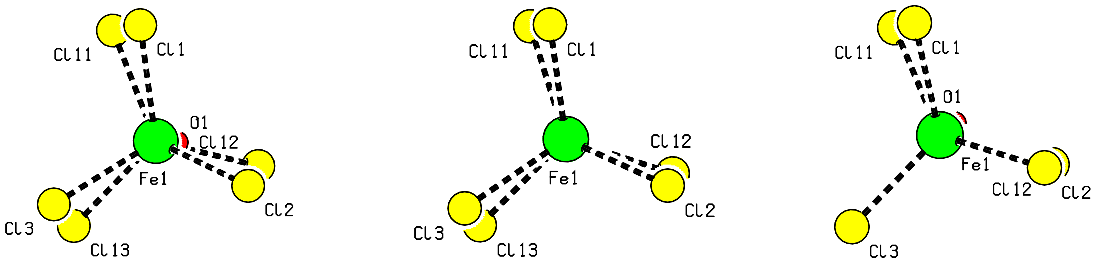

(a) Ambient pressure (b) 0.46 GPa (c) 1.66 GPa

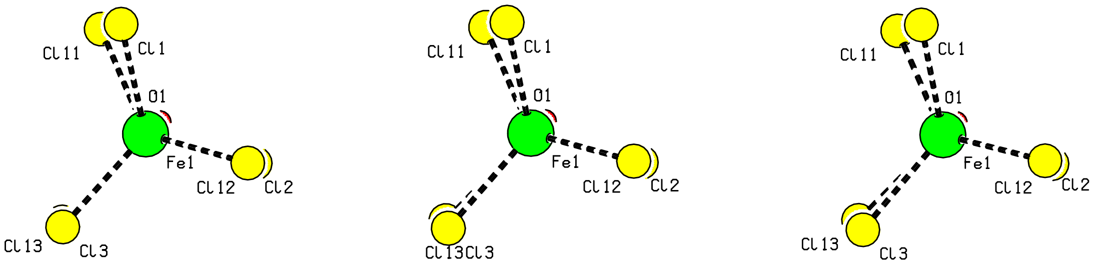

(d) 2.82 GPa (e) 3.89 GPa (f) 5.06 GPa

Figure 5.5: Projection along Fe1–Fe2 of **5** as a function of pressure.

The phase change results from a rotation of the two cations in the unit cell, which allows a higher packing along *c* (Figure 5.6). As a result of the phase change, the Cg1···Cg1* (2−*x*,

$1-y, 1-z$) distance drops from 5.603 Å to 5.068 Å and the Cg2···Cg1* interaction drops from 5.498(3) Å to 4.277(4) Å (22.2 % decrease). The CH···π interaction between H701* ($x, 3/2-y, -1/2+z$) and cg2 (C30→C80) previously reported no longer exists at 1.66 GPa, due to the rotation of the cations and is replaced by a $\pi\cdots\pi$ interaction (Figure5.7).

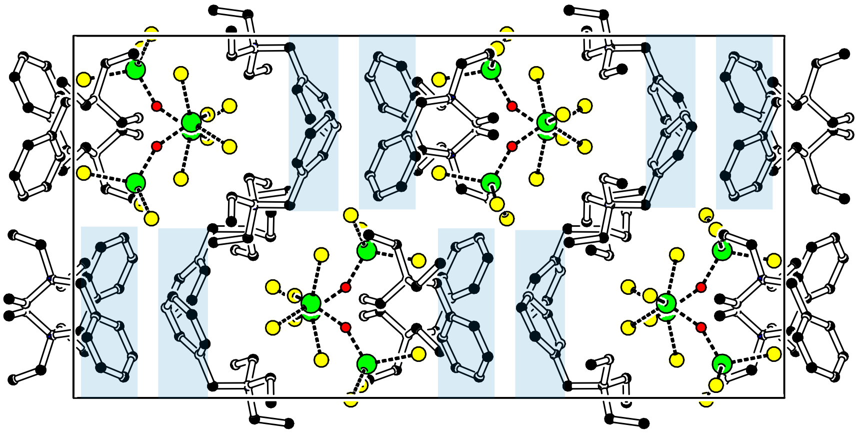

(a) Ambient pressure

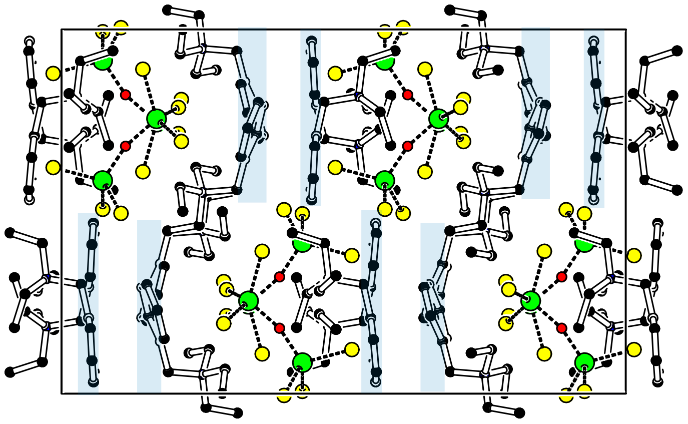

(b) 1.66 GPa

Figure 5.6: Evolution of the packing of **5** as a function of pressure. Fe are in green, Cl in yellow, O in red, N in blue, C in black and H in white. View along the b-axis.

The close contacts reported in phase I no longer exist. They were mostly along the a-axis, this could explain the increase of the a parameter. Instead, numerous other close contacts appear (H51···Cl11, H121···Cl2, H1101···Cl1, H2201···Cl3, H3101···Cl3 and H3102···Cl1) mostly along the b-axis with distances from 2.63 Å to 2.74 Å (Figure 5.8).

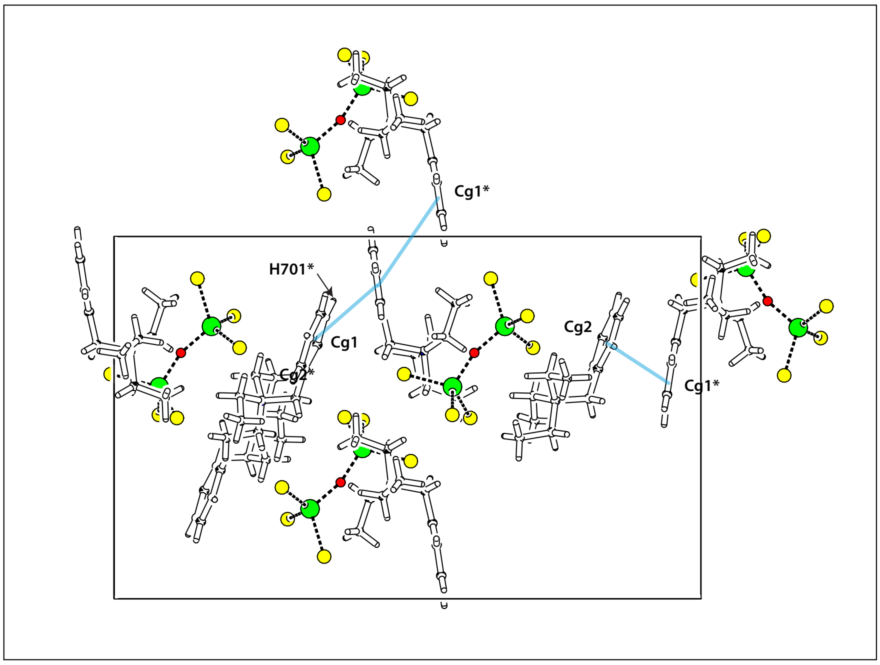

Figure 5.7: $\pi\cdots\pi$ interactions of **5** at 1.66 GPa. Fe are in green, Cl in yellow, O in red, N in blue, C in black and H in white. View along *b*-axis.

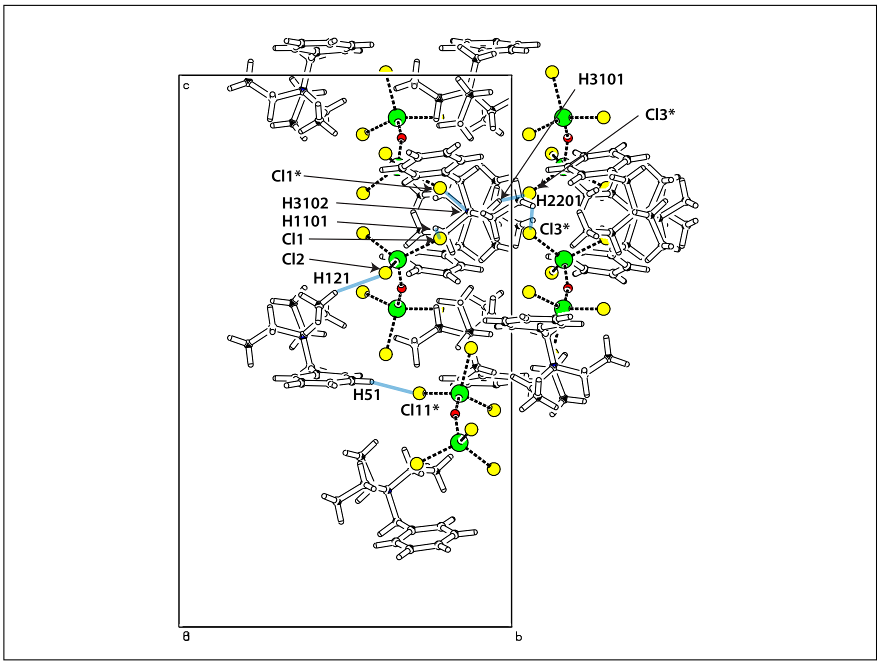

Figure 5.8: H···Cl short contacts of **5** at 1.66 GPa. Fe are in green, Cl in yellow, O in red, N in blue, C in black and H in white. View along *a*-axis.

The structure of $[N(CH_2Ph)(CH_2CH_3)_3]_2[Fe_2OCl_6]$–III at 2.82 GPa

Between 1.66 GPa and 2.82 GPa, **5** underwent a second single-crystal to single-crystal phase transition without any changes in the space group. The *b* and *c* parameters continue to decrease, with a decrease of 1.9 % and 2.9 %, respectively. The *a* parameter that previously increased up to 1.66 GPa now decreases by 0.5 %. The phase change results from the limit of the counter-intuitive increase in the *a* parameter. A further increase of the *a* parameter is no longer favourable.

Bond lengths remain similar (Table 5.2). The Fe1–*O*–Fe2 angle previously showed interesting changes but the angle at 2.82 GPa and 1.66 GPa is the same at 159.0(3)° (Table 5.3).

However, $\pi\cdots\pi$ stacking interactions continue to decrease, the Cg1···Cg1* $(2-x, 1-y, 1-z)$ distance drops from 5.068 Å to 5.007 Å, the Cg2···Cg1* $(3/2-x, 1-y, 1/2+z)$ distance drops from 4.277 Å to 4.146 Å. The structure now displays two CH···π interactions below 3 Å: H81···Cg2* (2.94 Å), H123···Cg1 (2.63 Å) and one Cl···π interaction at 3.450 Å (Cl1···Cg2). Ten short contacts are also present from 2.140 Å to 2.730 Å including a H···H contact and H···Cl contacts (Figure 5.9).

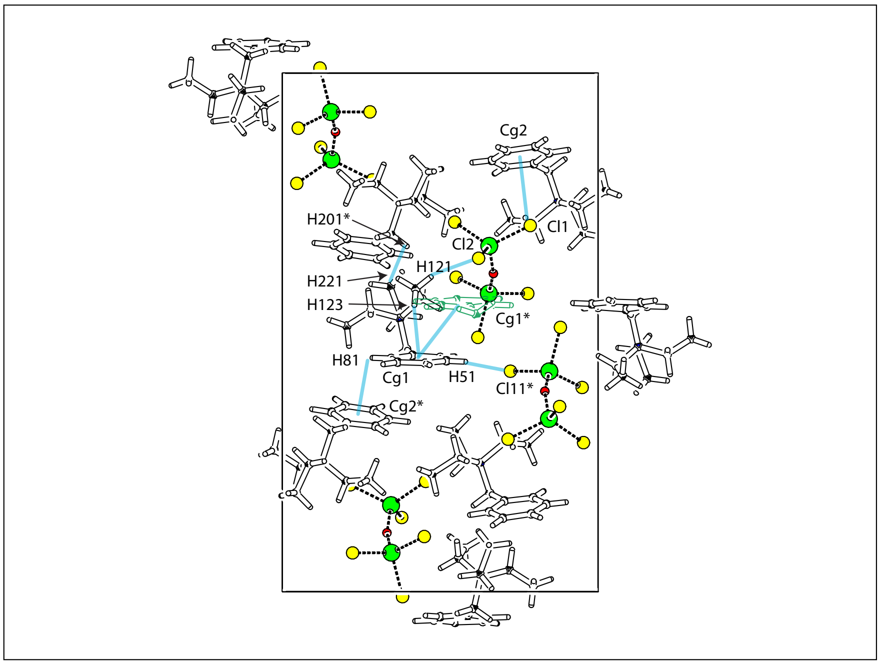

Figure 5.9: H···H short contact, H···Cl shortest contacts and $\pi\cdots\pi$ interactions of **5** at 2.82 GPa. View along *a*-axis. Only the two shortest H···Cl contacts are represented. The asymmetric unit containing Cg1* is not totally represented to avoid confusion, only the Cg1* ring in green is drawn. Fe are in green, Cl in yellow, O in red, N in blue, C in black and H in white.

The response of $[N(CH_2Ph)(CH_2CH_3)_3]_2[Fe_2OCl_6]$–III to 5.06 GPa

Between 2.82 GPa and 5.06 GPa, all the parameters decrease from 1.4 % for a, 2.7 % for b and 3.4 % for c. The greatest decrease is again along c, due to a shortening distance between the offset $\pi\cdots\pi$ stacking interactions.

Intra-molecular interactions do not change much between 2.82 GPa and 5.06 GPa. The biggest change is along Fe2–Cl13 with a 0.012(4) Å decrease in length. The Fe–O–Fe angle increases from 159.0(3)° to 159.9(3)° (Table 5.2 and Table 5.3).

Inter-molecular interactions become shorter on increasing the pressure as expected. $\pi\cdots\pi$ stacking interactions continue to decrease with a minimum distance of 4.018(4) Å for Cg2···Cg1*. No new CH···π or Cl···π interactions are present. The shortest of the three interactions previously reported, H123···Cg1, simply decrease to 2.52 Å from 2.63 Å (Figure 5.9). Numerous short contacts are present, eight H···Cl contacts and six H···H contacts. The shortest contact is between H201 and H221* (Figure 5.9) with a distance of 2.00 Å. The shortest H···Cl contact is between H51 and Cl11* (Figure 5.9) with a distance of 2.45 Å.

5.2 $[N(CH_3)_4]_2[Fe_2OCl_6] \cdot CH_3CN$

5.2.1 Synthesis

A solution of $NaOCH_3$ (540 mg, 10 mmol in 60 mL of CH_3OH) was added dropwise over a period of 1 h to a solution of 1.62 g of $FeCl_3$ in 40 mL of CH_3OH with rapid stirring. During the addition the reaction mixture changed from a light yellow colour to deep brown. After the addition was complete, 0.5 mL of water was added, the reaction mixture was stirred for 1 h. The Me_4NCl salt (1.5 g, 10 mmol) was then added to the mixture and the reaction stirred for half an hour.

The CH_3OH was removed using a rotary evaporator (the heating bath was maintained below 60° C) until a thick slurry was obtained. It is important not to take the mixture completely to dryness, a step that markedly decreases the final yield. To the slurry of crude product was added 80 mL of CH_3CN. The resulting cloudy brown suspension was stirred for 15 min and filtered. The filtrate was concentrated under vacuum to a volume of 5-10 mL and filtered again.

Red crystals of $[N(CH_3)_4]_2[Fe_2OCl_6]\cdot CH_3CN$ (Figure 5.10) were obtained by vapour diffusion of diethyl ether into the previous CH_3CN solution. Crystals are not air stable and loose solvent rapidly. IR spectroscopy (cm^{-1}; s = strong; m = medium; w = weak): 873 (s, Fe–O–Fe); 947 (s, cation); 1408 (m, cation); 1479 (s, cation); 3029 (w, impurity). Anal. Calcd (desolvated complex): C, 19.66; H, 4.95; N, 5.73. Found: C, 17.54; H, 4.33; N, 4.95. Fe titration: Fe, 22.85. Found: Fe, 20. Cl gravimetry: Cl, 43.53. Found: Cl, 42. The impurity has not been identified but has not been seen in the crystallography.

Figure 5.10: Crystals of **6**.

5.2.2 High-Pressure Crystallography

General Procedures

High-pressure experiments were carried out as explained in Section 2.2. Data were collected from 0.21 GPa up to a final pressure of 2.71 GPa. Above 2.18 GPa, the data quality depreciated rapidly and no acceptable refinement could be obtained for the final 2.71 GPa data set, and only cell-dimensions are reported here. Most probably the crystal undergoes a second phase change as shown in the rupture of the trend on the β angle and the a parameter. All atoms except carbons, nitrogens and hydrogens were refined with anisotropic thermal parameters. Listings of crystal and refinement data are given in Table 5.4.

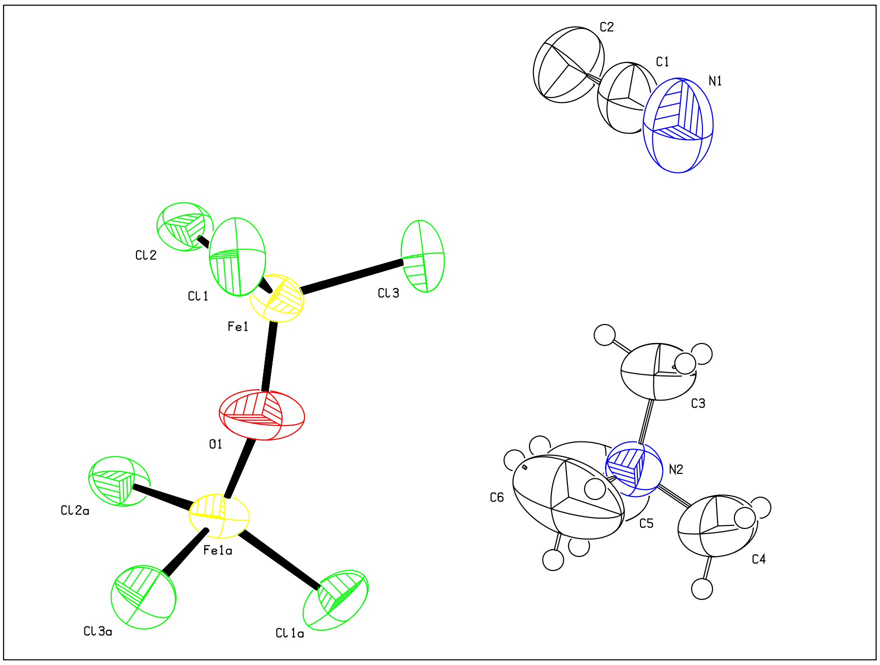

Figure 5.11: ORTEP drawing of **6** at ambient pressure, room temperature.

Table 5.4: Crystallographic data of **6** as a function of pressure.

Phase Pressure (Å)	Phase I ambient	Phase I 0.21	Phase II 0.87	Phase II 1.49	Phase II 2.18	Phase III 2.71
Formula	$[N(CH_3)_4]_2[Fe_2OCl_6] \cdot CH_3CN$					
Space group	$C2/c$	$C2/c$	Cc	Cc	Cc	Cc
T (K)	293	293	293	293	293	293
a (Å)	13.9148(16)	13.8324(6)	13.5332(12)	13.320(2)	13.221(3)	12.918
b (Å)	13.3157(15)	13.1796(5)	12.5246(9)	12.2675(18)	12.060(2)	11.927
c (Å)	14.0475(16)	13.9608(4)	13.6576(7)	13.4969(14)	13.370(2)	13.257
β	105.192(7)	105.320(3)	104.841(6)	104.600(11)	104.245(14)	104.66
Volume (Å^3)	2511.8(5)	2454.69(16)	2237.7(3)	2134.2(5)	2066.2(7)	1976
Radiation type	Mo Kα	Synchrotron	Synchrotron	Synchrotron	Synchrotron	Synchrotron
λ (Å)	0.71073	0.4792	0.4792	0.4792	0.4792	0.4792
Refinement	$\|F\|^2$	$\|F\|^2$	$\|F\|^2$	$\|F\|^2$	$\|F\|^2$	$\|F\|^2$
Z	4	4	4	4	4	4
R^a, $wR2^b$, S^c	0.087, 0.098,	0.084, 0.109,	0.084, 0.106,	0.090, 0.099,	0.110, 0.159,	–
	0.99	1.01	1.04	1.08	1.11	–
Reflections	1843	1437	2283	1472	1385	–
Parameters	102	102	200	200	135	–

$^aR = \sum \left| |F_o| - |F_c| \right| / \sum |F_o|$

$^b wR2 = \sum w \left(F_o^2 - F_c^2\right)^2 / \sum w \left(F_o^2\right)^2$

$^c S = \sqrt{\sum w \left({F^o_{hkl}}^2 - {F^c_{hkl}}^2\right) / (n - p)}$

5.2.3 Results and Discussion

The structure of $[N(CH_3)_4]_2[Fe_2OCl_6] \cdot CH_3CN$ at ambient pressure

$[N(CH_3)_4]_2[Fe_2OCl_6] \cdot CH_3CN$ (**6**) was found to crystallise in the monoclinic space group $C2/c$. The unit cell consists of one $[Fe_2OCl_6]^{2-}$ anion, two $[N(CH_3)_4]^+$ cations and an acetonitrile molecule (Figure 5.11). The two iron centres are tetrahedral and bridged by an oxide, the remaining coordinate sites are filled with chlorine ligands.

Apart from Van der Waals forces, the only possible intermolecular interactions are hydrogen bonds or H···H contacts. None of these are present at ambient pressure. On increasing pressure, the structure of **6** was found to be stable to 0.21 GPa. Above this pressure, the compound underwent a single-crystal to single-crystal phase transition to a previously unknown high-pressure phase which we have designated $[N(CH_3)_4]_2[Fe_2OCl_6] \cdot CH_3CN$–II, referring to the previous phase as $[N(CH_3)_4]_2[Fe_2OCl_6] \cdot CH_3CN$–I. The second phase was found to be stable up to 2.18 GPa. The last data set at 2.71 GPa could not be refined and only the unit cell has been reported. The evolution of the cell parameters on increasing pressure are shown in Figure 5.12.

The response of $[N(CH_3)_4]_2[Fe_2OCl_6] \cdot CH_3CN$–I to 0.21 GPa

On increasing pressure to 0.21 GPa, the a, b, c parameters are slowly decreasing by 0.6-1.0 %. However, the β angle increases by 0.13(1)°. Although the changes are statistically significant, they are very small as the decrease in volume is only 57.1(6) Å^3 (Figure 5.12).

Bonds length and angles do not show any change at this range of pressure, see Table 5.5 and Table 5.6. Inter-molecular interactions were non existent at ambient pressure and start to appear at 0.21 GPa with one short contact between H91···Cl4 with a distance of 2.75 Å.

The structure of $[N(CH_3)_4]_2[Fe_2OCl_6] \cdot CH_3CN$–II at 0.87 GPa

Between 0.21 GPa and 0.87 GPa, **6**–I underwent a single-crystal to single-crystal phase transition. The space group changes from $C2/c$ to Cc.

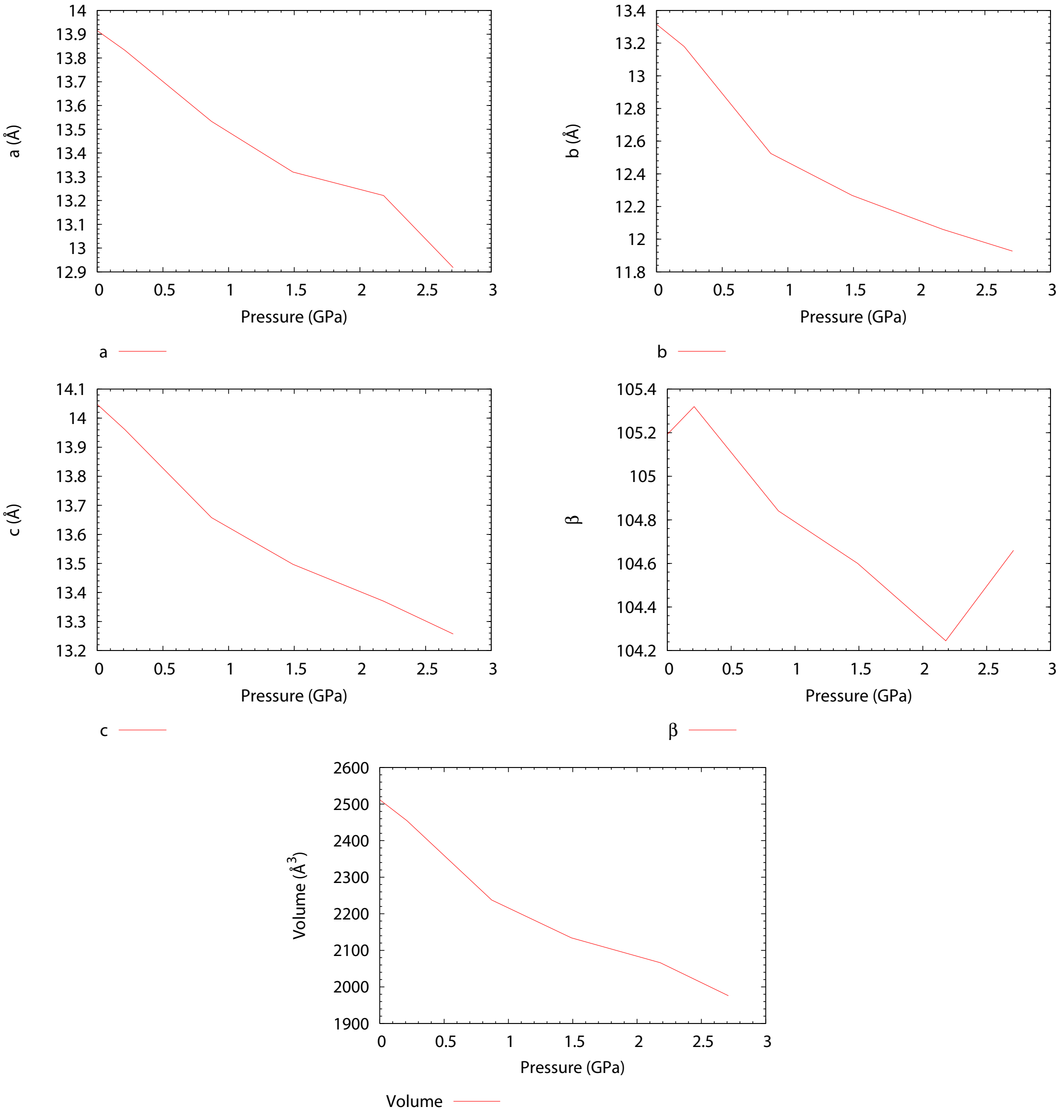

Figure 5.12: Evolution of cell parameters of **6** as a function of pressure.

Table 5.5: Evolution of selected bonds length of **6** as a function of pressure.

Phase Pressure (GPa)	phase I ambient	phase I 0.21	phase II 0.87	phase II 1.49	phase II 2.18
Fe1–O1 (Å)	1.735(2)	1.737(2)	1.767(16)	1.764(19)	1.79(3)
Fe2–O1 (Å)	–	–	1.751(15)	1.742(17)	1.74(3)
Fe1–Cl1 (Å)	2.267(2)	2.276(3)	2.297(5)	2.302(7)	2.322(8)
Fe1–Cl2 (Å)	2.267(2)	2.2745(19)	2.254(4)	2.271(6)	2.247(7)
Fe1–Cl3 (Å)	2.268(2)	2.270(2)	2.259(5)	2.258(5)	2.255(8)
Fe2–Cl4 (Å)	–	–	2.273(5)	2.264(5)	2.266(8)
Fe2–Cl5 (Å)	–	–	2.274(6)	2.266(6)	2.266(8)
Fe2–Cl6 (Å)	–	–	2.269(4)	2.272(4)	2.281(7)

Table 5.6: Evolution of selected angles of **6** as a function of pressure.

Phase Pressure (GPa)	phase I ambient	phase I 0.21	phase II 0.87	phase II 1.49	phase II 2.18
Fe1–O1–(Fe1a,Fe2)	158.3(6)	157.2(7)	146.1(8)	144.6(9)	140.1(14)

The change in the space group results in the loss of the inversion centre on the oxygen atom and the two cations are now independent. The β angle increased from ambient pressure to 0.21 GPa. It now decreases to 104.841(6). a, and c decrease by 0.3 Å while the b parameter decreases by 0.6 Å.

There is very little change in the Fe–O or Fe–Cl bond lengths. The rupture of symmetry causes the two Fe–O bonds to be different. Fe1–O1 increases by 0.03 Å while Fe2–O1 decreases by 0.14 Å. However, there is a decrease of 11° in the Fe–O–Fe angle, see table 5.6.

The phase change is due to a rotation of one the cations in the unit cell (Figure 5.13) which results in a lower symmetry space group. Five short contacts also appeared (Figure 5.14), two H···Cl contacts: H41···Cl2 (2.67 Å) and H91···Cl4 (2.73 Å); one H···H contact: H81···H53 (2.14 Å); one H···C contact: H62···C1 (2.52 Å) and one H···O contact: H82···O1 (2.50 Å).

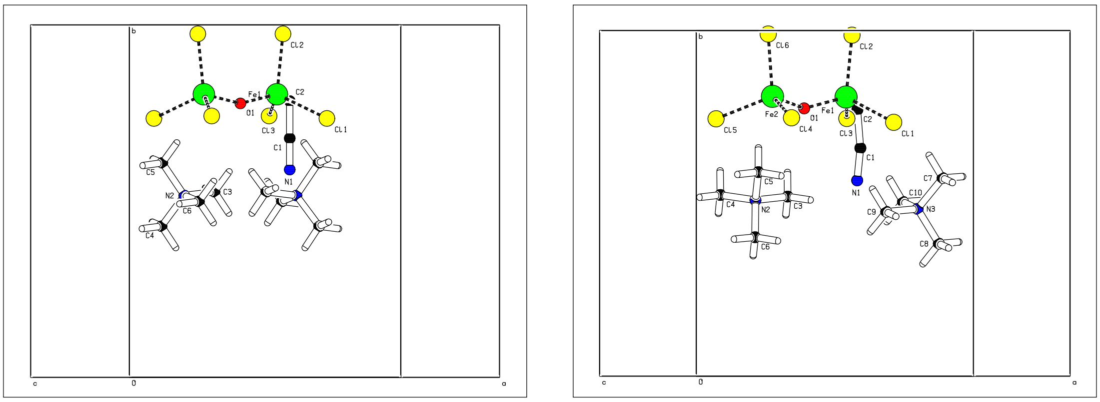

(a) 0.21 GPa. View through *bc*-face.

(b) 0.87 GPa. View along *bc*-face.

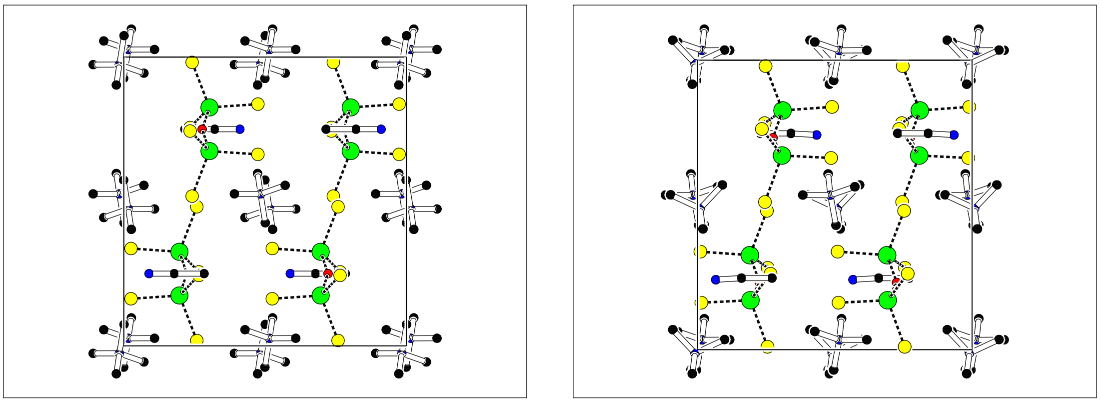

(c) 0.21 GPa. View along *a*-axis.

(d) 0.87 GPa. View along *a*-axis.

Figure 5.13: Evolution of the packing of **6** as a function of pressure. Fe are in green, Cl in yellow, O in red, N in blue, C in black and H in white.

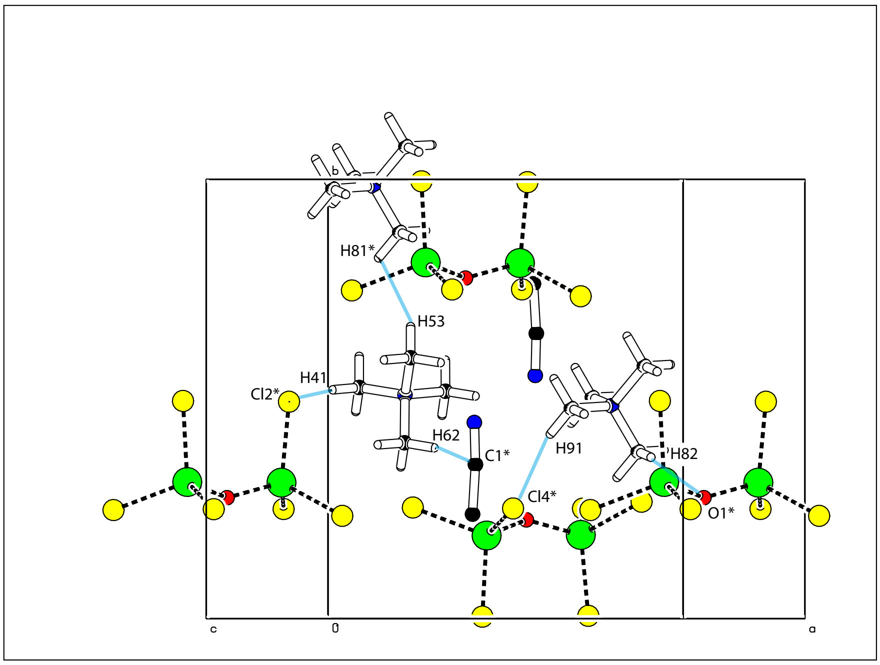

Figure 5.14: Short contacts of **6** at 0.87 GPa. Fe are in green, Cl in yellow, O in red, N in blue, C in black and H in white.

The response of $[N(CH_3)_4]_2[Fe_2OCl_6]\cdot CH_3CN$–II to 2.18 GPa

On increasing pressure to 2.18 GPa, the a, b, c parameters slowly decrease by 2.1-3.7 %. The β also decreases by 0.6°. Although the changes are statistically significant, they are very small (Figure 5.12).

Compared to the inter-molecular interactions present at 0.87 GPa, only one new interaction appears between H103 and Cl3 with a distance of 2.73 Å. All the previous interactions simply get smaller. The shortest contact is still H53···H81 with a distance of 2.11 Å. The shortest H–Cl contact is H41···Cl2* with a distance of 2.63 Å.

5.3 [Fe(salen)Cl]$_2$

5.3.1 Synthesis

[Fe(salen)Cl]$_2$* was prepared by following the synthesis from Zhou *et al.* [102]. The N,N'-bis-salicylidene-ethylenediamine ligand was analytical pure grade, purchased from Aldrich. A solution of N,N'-bis-salicylidene-ethylenediamine (salenH$_2$, 664 mg, 2.5 mmol) dissolved in acetonitrile (30 mL) was added dropwise to a solution of $FeCl_3$ (388 mg, 2.4 mmol) dissolved in methanol (20 mL) with stirring (orange to red color). The solution presented a dark red color, was stirred 0.5 h at room temperature and filtered. The filtrate was allowed to evaporate naturally at ambient temperature and black crystals of [Fe(salen)Cl]$_2$ (7) were obtained after a week. IR spectroscopy (cm^{-1}; s = strong; m = medium; w = weak): 615 (s); 755 (s); 792 (m); 864 (m); 902 (m); 982 (m); 1031 (m); 1046 (m); 1087 (m); 1123 (m); 1143 (m); 1195 (m); 1244 (m); 1268 (m); 1301 (m); 1324 (m); 1384 (m); 1443 (m); 1463 (m) 1543 (m); 1595 (m); 1626 (m).

---

* [Fe(salen)Cl]$_2$ was obtained instead of the expected [Fe(salen)]O$_2$ from Zhou *et al.* [102]

5.3.2 High-Pressure Crystallography

General Procedures

High-pressure experiments were carried out as explained in Section 2.2. Fe and Cl were refined with anisotropic thermal parameters, all other atoms were refined with isotropic thermal parameters. The numbering scheme used is the same as CSD refcode FESLED10.[103] Listings of crystal and refinement data are given in Table 5.7.

Table 5.7: Evolution of the parameters of **7** as a function of pressure.

Phase Pressure (GPa)	Phase I ambient	Phase I 0.55	Phase I 0.82	Phase I 1.45	Phase I 1.85	Phase I 2.37
Formula	[Fe(salen)Cl]$_2$					
Space group	$P21/c$	$P21/c$	$P21/c$	$P21/c$	$P21/c$	$P21/c$
T (K)	293	293	293	293	293	293
a (Å)	11.3706(5)	11.1194(4)	11.0357(3)	10.8709(5)	10.7847(3)	10.6972(3)
b (Å)	6.9141(3)	6.8181(3)	6.7852(2)	6.7169(4)	6.6776(2)	6.6349(2)
c (Å)	19.2825(8)	18.884(3)	18.7716(18)	18.482(4)	18.3683(15)	18.234(2)
β	90.164(2)	92.382(6)	93.249(4)	94.904(8)	95.845(5)	96.710(5)
Volume (Å^3)	1515.94(11)	1430.4(2)	1403.35(15)	1344.6(3)	1315.93(12)	1285.29(15)
Radiation type	Mo Kα	Synchrotron	Synchrotron	Synchrotron	Synchrotron	Synchrotron
λ (Å)	0.71073	0.4767	0.4767	0.4767	0.4767	0.4767
Refinement	$\|F\|^2$	$\|F\|^2$	$\|F\|^2$	$\|F\|^2$	$\|F\|^2$	$\|F\|^2$
Z	2	2	2	2	2	2
R^a, $wR2^b$, S^c	0.026, 0.058, 1.03	0.057, 0.156, 0.82	0.062, 0.185, 0.88	0.058, 0.153, 0.83	0.049, 0.123, 0.75	0.050, 0.133, 0.75
Reflections	3098	1156	1136	905	968	868
Parameters	199	99	99	99	99	99

Phase Pressure (GPa)	Phase I 3.09	Phase I 3.46	Phase I 3.90	Phase I 4.90	Phase I 5.54
Formula	[Fe(salen)Cl]$_2$				
Space group	$P21/c$	$P21/c$	$P21/c$	$P21/c$	$P21/c$
T (K)	293	293	293	293	293
a (Å)	10.6261(3)	10.5739(2)	10.5308(2)	10.454(4)	10.380(3)
b (Å)	6.5975(3)	6.5702(2)	6.5463(2)	6.492(2)	6.4734(16)
c (Å)	18.111(3)	18.0350(17)	17.9697(18)	17.81(2)	17.752(9)
β	97.377(6)	97.878(4)	98.281(4)	99.79(6)	99.64(4)
volume (Å^3)	1259.2(2)	1241.11(13)	1225.88(13)	1191.1(15)	1176.0(8)
Radiation type	Synchrotron	Synchrotron	Synchrotron	Synchrotron	Synchrotron
λ (Å)	0.4767	0.4767	0.4767	0.4767	0.4767
Refinement	$\|F\|^2$	$\|F\|^2$	$\|F\|^2$	$\|F\|^2$	$\|F\|^2$
Z	2	2	2	2	2
R, $wR2$, S	0.067, 0.173, 0.86	0.065, 0.162, 0.83	0.051, 0.135, 0.79	0.056, 0.109, 1.14	0.098, 0.197, 1.05
Reflections	886	878	872	619	449
Parameters	99	99	99	99	99

$^aR = \sum \big| |F_o| - |F_c| \big| / \sum |F_o|$

$^bwR2 = \sum w\left(F_o^2 - F_c^2\right)^2 / \sum w\left(F_o^2\right)^2$

$^cS = \sqrt{\sum w\left({F_{hkl}^{o}}^2 - {F_{hkl}^{c}}^2\right) / (n-p)}$

5.3.3 Results and Discussion

The structure of [Fe(salen)Cl]$_2$ at ambient pressure

The crystal structure of 7 was first determined by Gerloch and Mabbs[103], and the complex was found to crystallise in the monoclinic space group $P2_1/c$. The molecule consists of one dimer sited on an inversion centre. The asymmetric unit is composed of the salen ligand and an iron(III) cation. The ligand is formed by the condensation of two salicylaldehyde molecules and a 1,2-diaminoethane molecule resulting in a tetradentate ligand, which fills the equatorial Fe(III) sites. The two remaining coordination sites are filled by a chloride and an alkoxide group from the next salen ligand forming the bridge between the dimers (Figure 5.15).

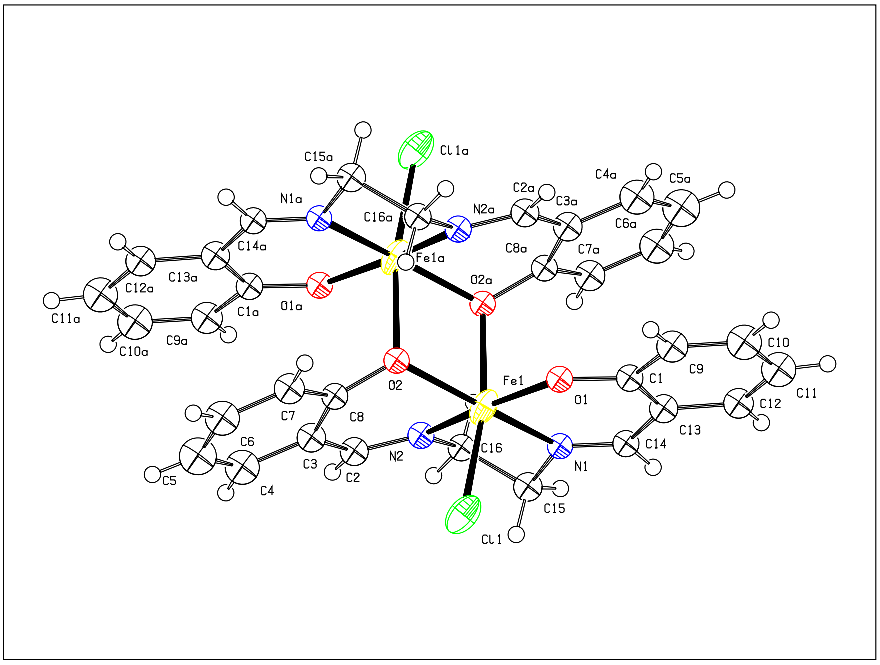

Figure 5.15: ORTEP drawing of 7 at 0.55 GPa.

The two iron(III) centres are separated by 3.3021(4) Å and the Fe–O–Fe angle is 103.76(6)°. The relatively short distance between the two metal centres causes some distortions on the ligand in order to avoid intra-molecular interactions between the two ligands. One side bends up toward the chloride while the other bends down. The result is the shortest interaction in the molecule with a distance between the two phenyl groups of 3.7806(14) Å (Figure 5.16).

There are also two inter-molecular $\pi \cdots \pi$ interactions: one between Cg5 (C1, C9, C10, C11, C12 and C13 centroid) and Cg5* $(1-x, -y, -z)$ with a distance of 5.1700(15) Å and

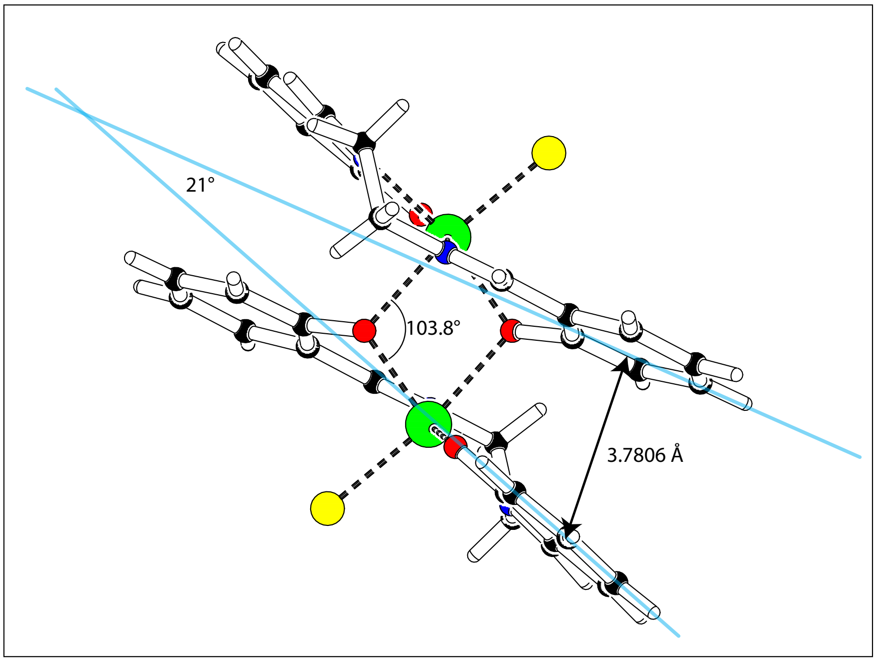

Figure 5.16: Phenyl to phenyl distance and angle on 7 at ambient pressure. Fe are in green, Cl in yellow, O in red, N in blue, C in black and H in white.

the other between Cg6 (C3→C8 centroid) and Cg6* ($-x, 1/2+y, 1/2-z$) with a distance of 5.2391(15) Å.

The response of [Fe(salen)Cl]$_2$ to 5.54 GPa

On increasing pressure to 5.54 GPa, the a, b and c parameters decrease equally (Figure 5.17) by about 7.5 % over 5.54 GPa. On the contrary, the β angle increases from 90.164(2)° to 99.64(4)° (Figure 5.17).

In terms of intra-molecular interactions, the distance between the two phenyl groups within the molecule decreases from 3.7806(14) Å at ambient pressure to 3.234(13) Å at 5.54 GPa. The two phenyl groups are almost parallel with an angle of 2.7(12)° instead of 21.12(11)° at ambient pressure (Figure 5.18). The iron-ligand bonds have little change change over 5.54 GPa, the maximum decrease is obtained on the Fe1–Cl1 bond, with a bond 0.044(18) Å shorter. The Fe1–O2* bond is a little shorter with 2.18(2) Å at 5.54 GPa compared to 2.2015(14) Å at ambient pressure. The Fe1–O2–Fe1* angle is also decreasing from 103.76(6)° to 102.6(9)°. As a result, the Fe1–Fe1* distance is shorter, decreasing from 3.3021(4) Å to 3.240(8) Å.

Consequently, the main part in the volume reduction is through compression of void

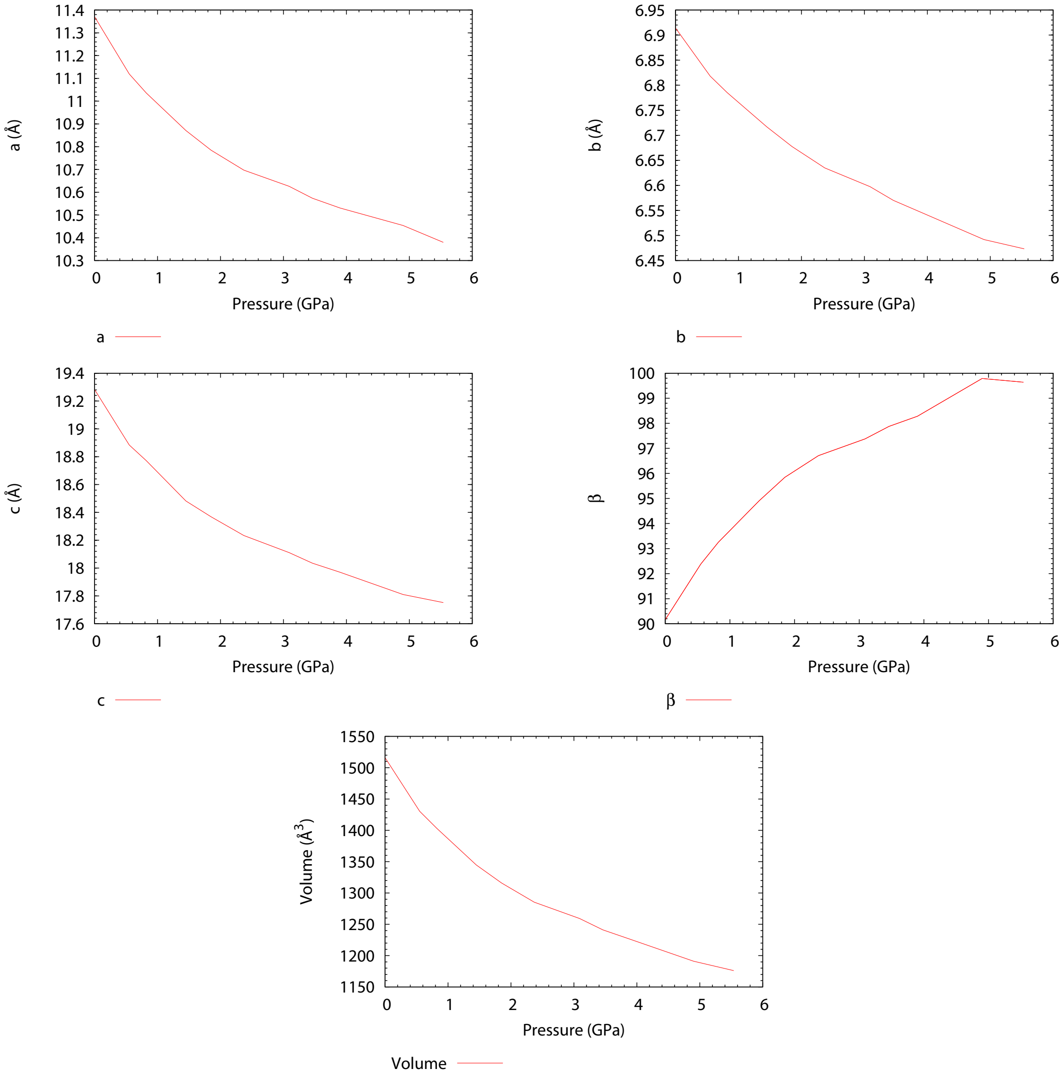

Figure 5.17: Evolution of cell parameters of 7 as a function of pressure.

Table 5.8: Fe–X bond distances of 7 at ambient pressure and 5.54 GPa

Ambient pressure			5.54 GPa		
Atom1	Atom2	Å	Atom1	Atom2	Å
Fe1	Cl1	2.3139(6)	Fe1	Cl1	2.270(17)
Fe1	O1	1.9024(14)	Fe1	O1	1.880(18)
Fe1	O2	1.9925(13)	Fe1	O2	1.981(16)
Fe1	N1	2.1117(18)	Fe1	N1	2.067(16)
Fe1	N2	2.1131(15)	Fe1	N2	2.054(17)
Fe1	O2*	2.2015(14)	Fe1	O2*	2.18(2)

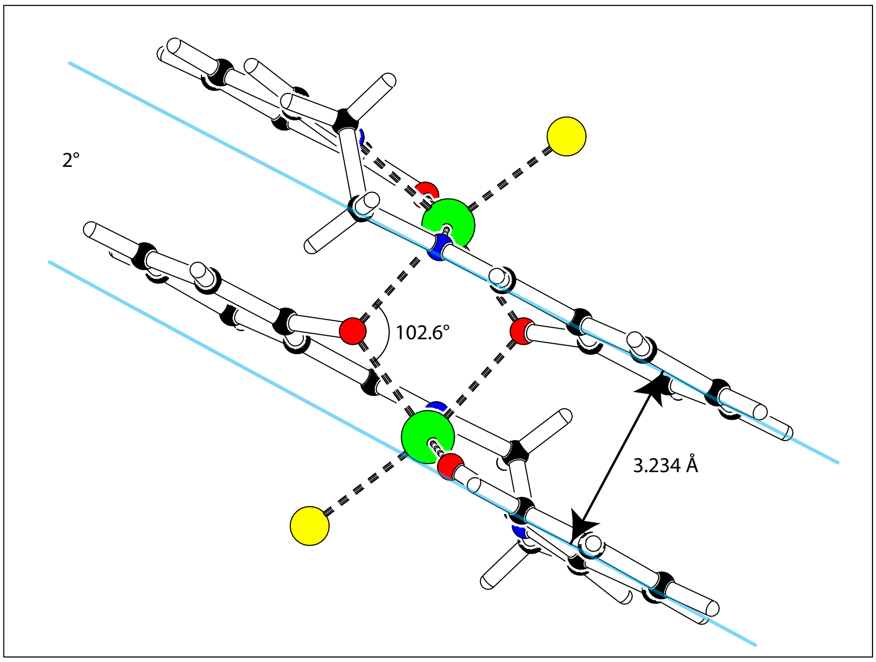

Figure 5.18: Phenyl to phenyl distance and angle on **7** at 5.54 GPa. Fe are in green, Cl in yellow, O in red, N in blue, C in black and H in white.

space between molecules. The Cg6–Cg6* interaction is the most representative with a decrease in distance from 5.2391(15) Å at ambient pressure to 4.556(13) Å at 5.54 GPa. The normal of the phenyl group is almost in the (a, b, c) direction which explains the similarities in the reduction on the a, b and c axes (Figure 5.19).

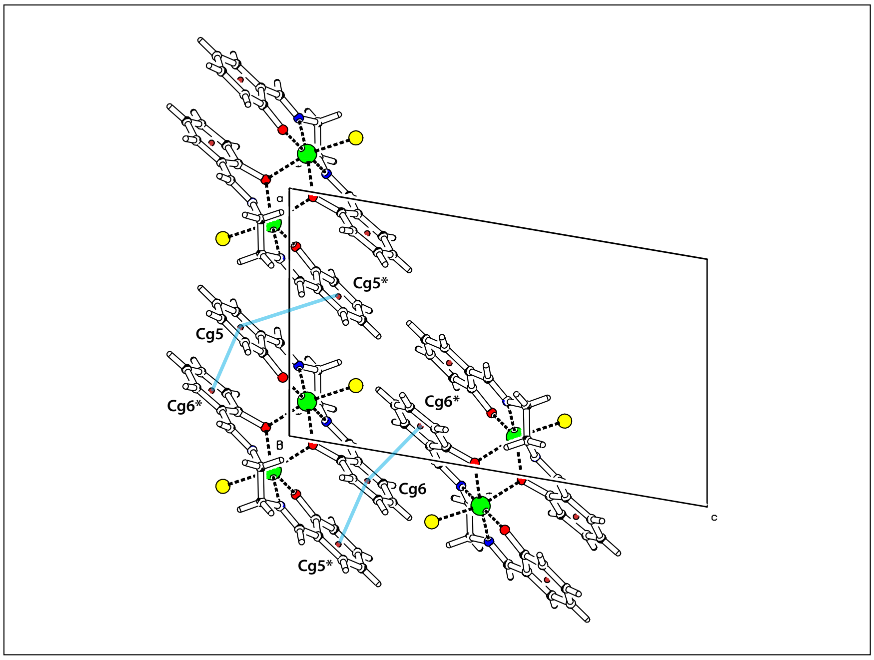

Figure 5.19: $\pi\cdots\pi$ interactions of $[Fe(salen)Cl]_2$ at 5.54 GPa. View along the *b*-axis. Fe are in green, Cl in yellow, O in red, N in blue, C in black and H in white.

5.4 Magnetism and conclusion

High pressure crystallography and high pressure magnetism can achieve a correlation on identical molecules at different pressures. Thus, only the structure changes and the chemical environment remains the same. Our crystallographic results revealed some changes in the Fe–O bonds lengths and Fe–O–Fe angles (Table 5.9 and Table 5.10). However no magnetic measurements were possible during the given time. The Fe–O oxo-bridged bonds remain rather similar in ($[N(CH_2Ph)(CH_2CH_3)_3]_2[Fe_2OCl_6]$) or decrease in ($[Fe(salen)Cl]_2$) or increase in ($[N(CH_3)_4]_2[Fe_2OCl_6] \cdot CH_3CN$) and finally the two Fe–O oxo-bridged bonds can become asymmetric as in $[Fe(salen)Cl]_2$ with a difference of 0.19(4) Å at 5.54 GPa. The oxo-bridged Fe–O–Fe angle also shows interesting behaviour with a decrease for both $[N(CH_2Ph)(CH_2CH_3)_3]_2[Fe_2OCl_6]$ and $[Fe(salen)Cl]_2$. The decrease in the Fe–O–Fe angle of $[N(CH_3)_4]_2[Fe_2OCl_6] \cdot CH_3CN$ is really impressive with 13.7(15)° for just 1.49 GPa. The behaviour of $[N(CH_2Ph)(CH_2CH_3)_3]_2[Fe_2OCl_6]$ is different as the angle increases at the start by 7.85(39)° and then decreases by 3.65(49)° at 1.66 GPa. Changes in the oxo-bridged angle are interesting because they occur in the range available for the magnetic pressure cell (~1.5 GPa). The changes in the oxo-bridged bond lengths are not so important and might not be significant in high pressure magnetism experiments.

Table 5.9: Evolution of Fe–O bonds length of **5**, **6** and **7** as a function of pressure.

(a) $[N(CH_3)_4]_2[Fe_2OCl_6] \cdot CH_3CN$

Phase	phase I	phase I	phase II	phase II	phase II
Pressure (GPa)	ambient	0.21	0.87	1.49	2.18
Fe1–O1 (Å)	1.735(2)	1.737(2)	1.767(16)	1.764(19)	1.79(3)
Fe2–O1 (Å)	–	–	1.751(15)	1.742(17)	1.74(3)

(b) $[N(CH_2Ph)(CH_2CH_3)_3]_2[Fe_2OCl_6]$

Phase	Phase I	Phase I	Phase II	Phase III	Phase III	Phase III
Pressure (GPa)	ambient	0.46	1.66	2.82	3.89	5.06
Fe1–O1 (Å)	1.753(3)	1.751(3)	1.760(4)	1.754(4)	1.769(4)	1.754(5)
Fe2–O1 (Å)	1.754(3)	1.751(3)	1.757(4)	1.763(4)	1.748(4)	1.755(5)

(c) $[Fe(salen)Cl]_2$

Pressure (GPa)	ambient	0.55	0.82	1.45	1.85	3.09	5.54
Fe1–O2 (Å)	1.9925(13)	1.984(4)	1.984(4)	1.983(5)	1.983(3)	1.984(6)	1.978(16)
Fe1–O2* (Å)	2.2015(14)	2.174(6)	2.176(6)	2.164(8)	2.176(6)	2.166(9)	2.17(2)

Table 5.10: Evolution of the Fe–O–Fe angle of **5**, **6** and **7** as a function of pressure.

(a) $[N(CH_3)_4]_2[Fe_2OCl_6] \cdot CH_3CN$

Phase	phase I	phase I	phase II	phase II	phase II
Pressure (GPa)	ambient	0.21	0.87	1.49	2.18
Fe1–O1–(Fe1a,Fe2)	158.3(6)	157.2(7)	146.1(8)	144.6(9)	140.1(14)

(b) $[N(CH_2Ph)(CH_2CH_3)_3]_2[Fe_2OCl_6]$

Phase	Phase I	Phase I	Phase II	Phase III	Phase III	Phase III
Angle	ambient	0.46 GPa	1.66 GPa	2.82 GPa	3.89 GPa	5.06 GPa
Fe1–O1–Fe2	154.8(2)	162.65(19)	159.0(3)	159.0(3)	159.2(3)	159.9(3)

(c) $[Fe(salen)Cl]_2$

Pressure (GPa)	ambient	0.55	0.82	1.45	1.85	3.09	5.54
Fe1–O2–Fe1*	103.76(6)	104.7(3)	104.4(3)	104.7(3)	104.1(3)	103.8(4)	102.6(9)

Chapter 6

Conclusion

Two Mn_{12} analogues have been studied: $[Mn_{12}O_{12}(O_2CCH_2Bu^t)_{16}(H_2O)_4] \cdot MeNO_2 \cdot CH_2Cl_2$ and $[Mn_{12}O_{12}(MeCO_2)_{16}(H_2O)_4] \cdot 2\,CH_3COOH \cdot 4\,H_2O$. The pressure cell used for the magnetic experiments did not allow us to use frequencies higher than 20-30 Hz for the out of phase AC susceptibility measurements. The maximum pressure that can achieved is also rather low compared to the diamond Anvil cell used for crystallography. The estimation of the energy barrier from the fit of the natural logarithm of the relaxation time as a function of the inverse temperature gave limited results due to small changes and the lack of precision. The widening of the curve compared to a true Lorentzian might be circumvented by a frequency scanning measurement rather than a temperature scanning measurement which, again, necessitates a better pressure cell for high frequencies. The hysteresis loop experiments lacked a good theoretical model of the loop.

However, we have shown the tilting of an elongated Jahn-Teller axis from “horizontal” to “vertical” on $[Mn_{12}O_{12}(O_2CCH_2Bu^t)_{16}(H_2O)_4] \cdot MeNO_2 \cdot CH_2Cl_2$ (**2a**), this behaviour has been seen in the single crystal X-ray measurements and is consistent with the changes observed in the out of phase AC susceptibility and hysteresis loops. An increase in the energy barrier on the LT peak of **2a** was also reported and ambient pressure values compare well to those reported.[26,104] Changes in the HT peak were too small to make a conclusion, however, the value reported is in agreement with the value found in the literature.[26]

Complex **1** is more complicated. At ambient pressure, the energy barrier is in agreement with the literature.[77] At high pressure, a second LT species and a second HT species is clearly present making the calculation of the energy barrier difficult. For the HT species we saw an increase of the energy barrier with a value in the same order of magnitude as those reported.[74,78] Finally, the hysteresis loops revealed a pressure dependence of the quantum tunnelling steps at 0.9 T and 1.3 T. For the 0.9 T steps our results show the same trend as previous studies, with an increase of the D parameter.[74,78]

The crystallographic study of $[Gd(PhCOO)_3(DMF)]_n$ as a function of pressure revealed a phase change via the twisting of a phenyl group. A short H···H contact between two phenyl groups of the chains induces the phase change. As a result, an inversion centre is lost and the space group goes from $P4_2/n$ to P-4. It could be the reason why no shorter contacts than the ambient pressure short contacts found in the CCDC database were seen.[40,92,93] The crystal would prefer to undergo major changes to avoid such contacts. However, the number of short contacts are more important in high pressure structures with four more of these in the $[Gd(PhCOO)_3(DMF)]_n$ complex and the $[VO(salpropane)]_n$ complex than in ambient pressure structures.

Both chains show very little effect of pressure on the backbone of the chains. This is a problem for magnetic studies of chains under pressure as magnetic properties strongly depend on the coordination sphere of the metal centres, which are the backbone of the molecule. Therefore, a new approach could be investigated on a zigzag chain[15] for example $[Co(hfac)_2(NITPhOMe)]$ (hfac = hexafluoroacetylacetonate and NITPhOMe = 4'-methoxy-phenyl-4,4,5,5-tetramethylimidazoline-1-oxyl-3-oxide).[94] The zigzag chain would be more sensitive to high pressure. Another approach is a polymerisation induced by pressure. Moggach *et al.*[95] reported a conversion of long intermolecular interactions into covalent bonds on $[GuH][Cu_2(OH)(cit)(Gu)_2]$ (H_4cit = citric acid, Gu = guanidine and GuH = guanidinium cation). This would produce a significant change in the magnetic properties.

The iron salen complexes and iron chloride complexes revealed the most important intra-molecular changes. $[N(CH_3)_4]_2[Fe_2OCl_6]\cdot CH_3CN$ revealed significant changes in the O–Fe–O angle with an increase of 5.1° and the Fe–O bonds in $[N(CH_3)_4]_2[Fe_2OCl_6]\cdot CH_3CN$ complex broke their symmetry, one bond increases by 0.06(3) Å, the other one doesn't change given the standard deviation. The last complex, $[Fe(salen)Cl]_2$, is more rigid but the intra-molecular $\pi\cdots\pi$ revealed a decrease of 0.7 Å between the centroids. Similarly to $[Gd(PhCOO)_3(DMF)]_n$ and $[VO(salpropane)]_n$ complexes, numerous short contacts are present at high pressure except for the $[Fe(salen)Cl]_2$ complex.

For $[N(PhCH_2)(CH_2CH_3)_3]_2[Fe_2OCl_6]$ and $[N(CH_3)_4]_2[Fe_2OCl_6]\cdot CH_3CN$ changes in the Fe–O bonds and O–Fe–O angles could reveal changes in the magnetic properties, but the very low magnetic response would make them very difficult to study at high pressure.

The new design of the diamond anvil cell greatly improved the quality of data collected compared to the old Beryllium cell. The use of a synchrotron light source was also helpful in increasing speed of collection, the quality of data and the completeness. Further developments on low temperature, high pressure crystallography are in progress in order to have even more accurate data as the magnetic experiments are done at low temperature. Triclinic structures suffer from the low completeness of data but results still have been obtained *e.g.* ($[\mathrm{Mn_{12}O_{12}(O_2CCH_2Bu^t)_{16}(H_2O)_4}]\cdot\mathrm{MeNO_2}\cdot\mathrm{CH_2Cl_2}$).

In the magnetic measurements, the NiCrAl piston cylinder pressure cell has been successfully used up to 1.5 GPa and the CuBe cell up to 1.1 GPa. Although the pressure range is low compared to the diamond anvil cell used for the crystallography, successful results have been obtained. Very high pressures are not necessary to observe significant changes and low pressures below 1.5 GPa are enough for some changes to emerge.

As technical difficulties are pushed further away this will allow us to explore the correlation between the structure and the magnetic properties of a molecule as a function of pressure.

Appendix A

SQUID sequence

```
FIELD COOLING + 10K CENTERING
HYSTERESIS LOOP
Set Temperature 10.000K at 2.000K/min.
Waitfor Temp:Stable Field:Stable Delay:10secs
Set Magnetic Field 0.00Oe, No Overshoot, Hi Res Enabled
Waitfor Field:Stable Delay:30secs
Set Temperature 2.000K at 2.000K/min.
Set Datafile: C:\QdMpms\Data\Murrie\PP103
Waitfor Temp:Stable Delay:600secs
FIRST STEP
Scan Field from 50.00Oe to 16050.00Oe in 1000.00Oe increments (17 steps), No
   →Overshoot, Hi Res Enabled
    Waitfor Temp:Stable Delay:15secs
    Measure DC: 4.00 cm, 24 pts, 3 scans, AutoRng, Long, Iterative Reg.,
       →track:Yes, raw:Yes, diag:Yes
End Scan
Scan Field from 17000.00Oe to 20000.00Oe in 1000.00Oe increments (4 steps),
   →No Overshoot, Hi Res Enabled
    Waitfor Temp:Stable Delay:15secs
    Measure DC: 4.00 cm, 24 pts, 3 scans, AutoRng, Long, Iterative Reg.,
       →track:Yes, raw:Yes, diag:Yes
End Scan
Scan Field from 25000.00Oe to 50000.00Oe in 5000.00Oe increments (6 steps),
   →No Overshoot, Hi Res Enabled
    Waitfor Temp:Stable Delay:15secs
    Measure DC: 4.00 cm, 24 pts, 3 scans, AutoRng, Long, Iterative Reg.,
       →track:Yes, raw:Yes, diag:Yes
End Scan
SECOND STEP
Scan Field from 45000.00Oe to 25000.00Oe in −5000.00Oe increments (5 steps),
   →No Overshoot, Hi Res Enabled
    Waitfor Temp:Stable Delay:30secs
    Measure DC: 4.00 cm, 24 pts, 3 scans, AutoRng, Long, Iterative Reg.,
       →track:Yes, raw:Yes, diag:Yes
End Scan
Scan Field from 20000.00Oe to 16000.00Oe in −1000.00Oe increments (5 steps),
   →No Overshoot, Hi Res Enabled
    Waitfor Temp:Stable Delay:30secs
    Measure DC: 4.00 cm, 24 pts, 3 scans, AutoRng, Long, Iterative Reg.,
```

```
        →track:Yes, raw:Yes, diag:Yes
End Scan
Scan Field from 15500.00Oe to 8000.00Oe in −500.00Oe increments (16 steps),
    →No Overshoot, Hi Res Enabled
    Waitfor Temp:Stable Delay:30secs
    Measure DC: 4.00 cm, 24 pts, 3 scans, AutoRng, Long, Iterative Reg.,
        →track:Yes, raw:Yes, diag:Yes
End Scan
Scan Field from 7800.00Oe to −14000.00Oe in −200.00Oe increments (110 steps),
    → No Overshoot, Hi Res Enabled
    Waitfor Temp:Stable Delay:30secs
    Measure DC: 4.00 cm, 24 pts, 3 scans, AutoRng, Long, Iterative Reg.,
        →track:Yes, raw:Yes, diag:Yes
End Scan
Scan Field from −14500.00Oe to −15500.00Oe in −500.00Oe increments (3 steps),
    → No Overshoot, Hi Res Enabled
    Waitfor Temp:Stable Delay:30secs
    Measure DC: 4.00 cm, 24 pts, 3 scans, AutoRng, Long, Iterative Reg.,
        →track:Yes, raw:Yes, diag:Yes
End Scan
Scan Field from −16000.00Oe to −20000.00Oe in −1000.00Oe increments (5 steps)
    →, No Overshoot, Hi Res Enabled
    Waitfor Temp:Stable Delay:30secs
    Measure DC: 4.00 cm, 24 pts, 3 scans, AutoRng, Long, Iterative Reg.,
        →track:Yes, raw:Yes, diag:Yes
End Scan
Scan Field from −25000.00Oe to −50000.00Oe in −5000.00Oe increments (6 steps)
    →, No Overshoot, Hi Res Enabled
    Waitfor Temp:Stable Delay:30secs
    Measure DC: 4.00 cm, 24 pts, 3 scans, AutoRng, Long, Iterative Reg.,
        →track:Yes, raw:Yes, diag:Yes
End Scan
THIRD STEP
Scan Field from −45000.00Oe to −25000.00Oe in 5000.00Oe increments (5 steps),
    → No Overshoot, Hi Res Enabled
    Waitfor Temp:Stable Delay:30secs
    Measure DC: 4.00 cm, 24 pts, 3 scans, AutoRng, Long, Iterative Reg.,
        →track:Yes, raw:Yes, diag:Yes
End Scan
Scan Field from −20000.00Oe to −16000.00Oe in 1000.00Oe increments (5 steps),
    → No Overshoot, Hi Res Enabled
    Waitfor Temp:Stable Delay:30secs
    Measure DC: 4.00 cm, 24 pts, 3 scans, AutoRng, Long, Iterative Reg.,
        →track:Yes, raw:Yes, diag:Yes
End Scan
Scan Field from −15500.00Oe to −8000.00Oe in 500.00Oe increments (16 steps),
    →No Overshoot, Hi Res Enabled
    Waitfor Temp:Stable Delay:30secs
    Measure DC: 4.00 cm, 24 pts, 3 scans, AutoRng, Long, Iterative Reg.,
        →track:Yes, raw:Yes, diag:Yes
End Scan
Scan Field from −7800.00Oe to 14000.00Oe in 200.00Oe increments (110 steps),
    →No Overshoot, Hi Res Enabled
    Waitfor Temp:Stable Delay:30secs
    Measure DC: 4.00 cm, 24 pts, 3 scans, AutoRng, Long, Iterative Reg.,
        →track:Yes, raw:Yes, diag:Yes
End Scan
```

```
Scan Field from 14500.00Oe to 15500.00Oe in 500.00Oe increments (3 steps), No
   → Overshoot, Hi Res Enabled
    Waitfor Temp:Stable Delay:30secs
    Measure DC: 4.00 cm, 24 pts, 3 scans, AutoRng, Long, Iterative Reg.,
       →track:Yes, raw:Yes, diag:Yes
End Scan
Scan Field from 16000.00Oe to 20000.00Oe in 1000.00Oe increments (5 steps),
   →No Overshoot, Hi Res Enabled
    Waitfor Temp:Stable Delay:30secs
    Measure DC: 4.00 cm, 24 pts, 3 scans, AutoRng, Long, Iterative Reg.,
       →track:Yes, raw:Yes, diag:Yes
End Scan
Scan Field from 25000.00Oe to 50000.00Oe in 5000.00Oe increments (6 steps),
   →No Overshoot, Hi Res Enabled
    Waitfor Temp:Stable Delay:30secs
    Measure DC: 4.00 cm, 24 pts, 3 scans, AutoRng, Long, Iterative Reg.,
       →track:Yes, raw:Yes, diag:Yes
End Scan
Set Magnetic Field 0.00Oe, Oscillate, Hi Res Enabled
Set Temperature 8.100K at 2.000K/min.
Waitfor Temp:Stable Delay:600secs
AC SUSCEPTIBILITY
Set Datafile: C:\QdMpms\Data\Murrie\PP104
Scan Temp from 7.950K to 1.800K at 1.000K/min in −0.15K increments (42 steps)
   → Settle
    Waitfor Temp:Stable Delay:15secs
    Measure AC: 3.0000Oe, 19.998 Hz, 3 meas, 3 blks, 1E−005 Null, x 1, 0 s,
       →AutoRng, track:Yes, diag:Yes, raw:Yes
End Scan
Scan Temp from 7.950K to 6.000K at 1.000K/min in −0.15K increments (14 steps)
   → Settle
    Waitfor Temp:Stable Delay:15secs
    Measure AC: 3.0000Oe, 9.999 Hz, 3 meas, 3 blks, 1E−005 Null, x 1, 0 s,
       →AutoRng, track:Yes, diag:Yes, raw:Yes
End Scan
Scan Temp from 5.950K to 1.800K at 1.000K/min in −0.05K increments (84 steps)
   → Settle
    Waitfor Temp:Stable Delay:15secs
    Measure AC: 3.0000Oe, 9.999 Hz, 3 meas, 3 blks, 1E−005 Null, x 1, 0 s,
       →AutoRng, track:Yes, diag:Yes, raw:Yes
End Scan
Scan Temp from 7.950K to 6.000K at 1.000K/min in −0.15K increments (14 steps)
   → Settle
    Waitfor Temp:Stable Delay:15secs
    Measure AC: 3.0000Oe, 4.999 Hz, 3 meas, 3 blks, 1E−005 Null, x 1, 0 s,
       →AutoRng, track:Yes, diag:Yes, raw:Yes
End Scan
Scan Temp from 5.950K to 1.800K at 1.000K/min in −0.05K increments (84 steps)
   → Settle
    Waitfor Temp:Stable Delay:15secs
    Measure AC: 3.0000Oe, 4.999 Hz, 3 meas, 3 blks, 1E−005 Null, x 1, 0 s,
       →AutoRng, track:Yes, diag:Yes, raw:Yes
End Scan
Scan Temp from 7.950K to 6.000K at 1.000K/min in −0.15K increments (14 steps)
   → Settle
    Waitfor Temp:Stable Delay:15secs
    Measure AC: 3.0000Oe, 1.001 Hz, 3 meas, 3 blks, 1E−005 Null, x 1, 0 s,
```

```
        →AutoRng, track:Yes, diag:Yes, raw:Yes
End Scan
Scan Temp from 5.950K to 1.950K at 1.000K/min in −0.05K increments (81 steps)
    → Settle
    Waitfor Temp:Stable Delay:15secs
    Measure AC: 3.0000Oe, 1.001 Hz, 3 meas, 3 blks, 1E−005 Null, x 1, 0 s,
        →AutoRng, track:Yes, diag:Yes, raw:Yes
End Scan
Scan Temp from 1.920K to 1.800K at 0.500K/min in −0.02K increments (7 steps)
    →Settle
    Waitfor Temp:Stable Delay:15secs
    Measure AC: 3.0000Oe, 1.001 Hz, 3 meas, 3 blks, 1E−005 Null, x 1, 0 s,
        →AutoRng, track:Yes, diag:Yes, raw:Yes
End Scan
Scan Temp from 6.600K to 4.650K at 1.000K/min in −0.15K increments (14 steps)
    → Settle
    Waitfor Temp:Stable Delay:15secs
    Measure AC: 3.0000Oe, 0.500 Hz, 3 meas, 3 blks, 1E−005 Null, x 1, 0 s,
        →AutoRng, track:Yes, diag:Yes, raw:Yes
End Scan
Scan Temp from 4.500K to 1.950K at 1.000K/min in −0.05K increments (52 steps)
    → Settle
    Waitfor Temp:Stable Delay:15secs
    Measure AC: 3.0000Oe, 0.500 Hz, 3 meas, 3 blks, 1E−005 Null, x 1, 0 s,
        →AutoRng, track:Yes, diag:Yes, raw:Yes
End Scan
Scan Temp from 1.920K to 1.800K at 0.500K/min in −0.02K increments (7 steps)
    →Settle
    Waitfor Temp:Stable Delay:15secs
    Measure AC: 3.0000Oe, 0.500 Hz, 3 meas, 3 blks, 1E−005 Null, x 1, 0 s,
        →AutoRng, track:Yes, diag:Yes, raw:Yes
End Scan
Scan Temp from 7.950K to 4.650K at 1.000K/min in −0.15K increments (23 steps)
    → Settle
    Waitfor Temp:Stable Delay:15secs
    Measure AC: 3.0000Oe, 0.100 Hz, 3 meas, 3 blks, 1E−005 Null, x 1, 0 s,
        →AutoRng, track:Yes, diag:Yes, raw:Yes
End Scan
Scan Temp from 4.500K to 1.950K at 1.000K/min in −0.05K increments (52 steps)
    → Settle
    Waitfor Temp:Stable Delay:15secs
    Measure AC: 3.0000Oe, 0.100 Hz, 3 meas, 3 blks, 1E−005 Null, x 1, 0 s,
        →AutoRng, track:Yes, diag:Yes, raw:Yes
End Scan
Scan Temp from 1.920K to 1.800K at 0.500K/min in −0.02K increments (7 steps)
    →Settle
    Waitfor Temp:Stable Delay:15secs
    Measure AC: 3.0000Oe, 0.100 Hz, 3 meas, 3 blks, 1E−005 Null, x 1, 0 s,
        →AutoRng, track:Yes, diag:Yes, raw:Yes
End Scan
Set Magnetic Field 0.00Oe, Oscillate, Hi Res Enabled
Waitfor Delay:30secs
Set Temperature 10.000K at 2.000K/min.
Waitfor Temp:Stable Delay:30secs
```

Bibliography

[1] R. J. Silbey and R. A. Alberty, *Physical chemistry*, 2001.

[2] P. W. Anderson, *Phys. Rev.*, 1950, **79**, 350–356.

[3] S. F. A. Kettle, *Physical Inorganic Chemistry*, Oxford : Spektrum, 1996.

[4] V. Poulsen, *Method of recording and reproducing sounds or signals*, US patent 661619, 1900.

[5] S. N. Piramanayagam, *J. Appl. Phys.*, 2007, **102**, 011301.

[6] S. M. Thompson, *J. Phys. D: Appl. Phys.*, 2008, **41**, 093001.

[7] J. F. Hu, J. S. Chen, Y. F. Ding, B. C. Lim, W. L. Phyoe and B. Liu, *appl. phys. lett.*, 2008, **93**, 072504.

[8] B. Terris, *J. Magn. Magn. Mater.*, 2009, **321**, 512 – 517.

[9] H. H. Wickman, A. M. Trozzolo, H. J. Williams, G. W. Hull and F. R. Merritt, *Phys. rev.*, 1967, **155**, 563–566.

[10] J. S. Miller, J. C. Calabrese, H. Rommelmann, S. R. Chittipeddi, J. H. Zhang, W. M. Reiff and A. J. Epstein, *J. Am. Chem. Soc.*, 1987, **109**, 769–781.

[11] R. Sessoli, H.-L. Tsai, A. R. Schake, S. Wang, J. B. Vincent, K. Folting, D. Gatteschi, G. Christou and D. N. Hendrickson, *J. Am. Chem. Soc.*, 1993, **115**, 1804–1816.

[12] T. Lis, *Acta Cryst.*, 1980, **B36**, 2042–2046.

[13] S. M. J. Aubin, M. W. Wemple, D. M. Adams, H.-L. Tsai, G. Christou and D. N. Hendrickson, *J. Am. Chem. Soc.*, 1996, **118**, 7746–7754.

[14] G. Aromí and E. K. Brechin, *Struct Bond*, 2006, **122**, 1–67.

[15] M. Murrie and D. J. Price, *Annu. Rep. Prog. Chem., Sect. A: Inorg. Chem.*, 2007, **103**, 20–38.

[16] A. M. Ako, I. J. Hewitt, V. Mereacre, R. Clérac, W. Wernsdorfer, C. E. Anson and A. K. Powell, *Angew. Chem. Int. Ed.*, 2006, **45**, 4926–4929.

[17] C. J. Milios, A. Vinslava, W. Wernsdorfer, S. Moggach, S. Parsons, S. P. Perlepes, G. Christou and E. K. Brechin, *J. Am. Chem. Soc.*, 2007, **129**, 2754–2755.

[18] C. Delfs, D. Gatteschi, L. Pardi, R. Sessoli, K. Wieghardt and D. Hanke, *Inorg. Chem.*, 1993, **32**, 3099–3103.

[19] N. Ishikawa, M. Sugita, T. Ishikawa, S.-y. Koshihara and Y. Kaizu, *J. Am. Chem. Soc.*, 2003, **125**, 8694–8695.

[20] N. Ishikawa, *Polyhedron*, 2007, **26**, 2147 – 2153.

[21] S. Osa, T. Kido, N. Matsumoto, N. Re, A. Pochaba and J. Mrozinski, *J. Am. Chem. Soc.*, 2004, **126**, 420–421.

[22] A. Mishra, W. Wernsdorfer, K. A. Abboud and G. Christou, *J. Am. Chem. Soc.*, 2004, **126**, 15648–15649.

[23] J. An, Z.-D. Chen, X.-X. Zhang, H. G. Raubenheimer, C. Esterhuysen, S. Gao and G.-X. Xu, *J. Chem. Soc., Dalton Trans.*, 2001, 3352–3356.

[24] H.-L. Tsai, D.-M. Chen, C.-I. Yang, T.-Y. Jwo, C.-S. Wur, G.-H. Lee and Y. Wang, *Inorg. Chem. Comm.*, 2001, **4**, 511–514.

[25] J. Lim, Y. Do and J. Kim, *Bull. Kor. Chem. Soc.*, 2005, **26**, 1065–1070.

[26] M. Soler, W. Wernsdorfer, Z. Sun, D. Ruiz, J. C. Huffman, D. N. Hendrickson and G. Christou, *Polyhedron*, 2003, **22**, 1783–1788.

[27] K. Takeda, K. Awaga and T. Inabe, *Phys. Rev. B*, 1998, **57**, R11062–R11064.

[28] S. M. J. Aubin, Z. Sun, H. J. Eppley, E. M. Rumberger, I. A. Guzei, K. Folting, P. K. Gantzel, A. L. Rheingold, G. Christou and D. N. Hendrickson, *Inorg. Chem.*, 2001, **40**, 2127–2146.

[29] K. Takeda, K. Awaga, T. Inabe, A. Yamaguchi, H. Ishimoto, T. Tomita, H. Mitamura, T. Goto, N. Môri and H. Nojiri, *Phys. Rev. B*, 2002, **65**, 094424.

[30] S. Takahashi, R. S. Edwards, J. M. North, S. Hill and N. S. Dalal, *Phys. Rev. B*, 2004, **70**, 094429.

[31] *The SQUID Handbook: Applications of SQUIDs and SQUID Systems*, ed. J. Clarke and A. I. Braginski, Wiley, 2006, vol. 2, pp. 392–435.

[32] J. Clarke, *SQUIDs*, Scientific American, 1994, vol. 2, p. 46.

[33] J. W. Rohlf, *Modern Physics from α to Z^0*, Wiley, 1994.

[34] R. J. Cernik, W. Clegg, C. R. A. Catlow, G. Bushnell-Wye, J. V. Flaherty, G. N. Greaves, I. Burrows, D. J. Taylor, S. J. Teat and M. Hamichi, *J. Synchrotron Radiat.*, 2000, 7, 40.

[35] D. Thompson, *IEEE Trans. Nucl. Sci.*, 1979, **26**, 3803–3805.

[36] D. Thompson, *Nucl. Instrum. Methods*, 1980, **177**, 27 – 34.

[37] S. A. Moggach, S. Parsons and P. A. Wood, *Crystallogr. Rev.*, 2008, **14**, 143–184.

[38] F. H. Allen, *Acta Cryst.*, 2002, **B58**, 380–388.

[39] C. Murli, S. M. Sharma, S. Karmakar and S. K. Sikka, *Physica B*, 2003, **339**, 23 – 30.

[40] S. A. Moggach and S. Parsons, *private communication*.

[41] C. M. Edwards and I. S. Butler, *Coord. Chem. Rev.*, 2000, **199**, 1–53.

[42] C. Slebodnick, J. Zhao, R. Angel, B. E. Hanson, Y. Song, Z. Liu and R. J. Hemley, *Inorg. Chem.*, 2004, **43**, 5245–5252.

[43] N. Casati, P. Macchi and A. Sironi, *Angew. Chem. Int. Ed.*, 2005, **44**, 7736–7739.

[44] G. Mínguez Espallargas, L. Brammer, D. R. Allan, C. R. Pulham, N. Robertson and J. E. Warren, *J. Am. Chem. Soc.*, 2008, **130**, 9058–9071.

[45] M. Bujak and R. J. Angel, *J. Phys. Chem. B*, 2006, **110**, 10322–10331.

[46] S. Tancharakorn, F. P. A. Fabbiani, D. R. Allan, K. V. Kamenev and N. Robertson, *J. Am. Chem. Soc.*, 2006, **128**, 9205–9210.

[47] K. Suzuki, J. Haines, P. Rabu, K. Inoue and M. Drillon, *J. Phys. Rev.*, 2008, **112**, 19147–19150.

[48] J. Eggert, 63rd Scottish universities summer school in physics, 2008.

[49] S. Klotz, 63rd Scottish universities summer school in physics, 2008.

[50] W. A. Bassett, *High Pressure Res.*, 2009, **29**, 163–186.

[51] S. A. Moggach, D. R. Allan, S. Parsons and J. E. Warren, *J. Appl. Crystallogr.*, 2008, **41**, 249–251.

[52] G. J. Piermarini, S. Block, J. D. Barnett and R. A. Forman, *J. Appl. Phys.*, 1975, **46**, 2774–2780.

[53] K. Murata, H. Yoshino, H. O. Yadav, Y. Honda and N. Shirakawa, *Rev. Sci. Instrum.*, 1997, **68**, 2490–2493.

[54] A. Eiling and J. S. Schilling, *J. Phys. F: Met. Phys.*, 1981, **11**, 623–639.

[55] Bruker-Nonius, *SAINT version 7*, Bruker-AXS, Madison, Wisconsin, USA, 2006.

[56] G. M. Sheldrick, *SADABS version 2004-1*, Bruker-AXS, Madison, Wisconsin, USA, 2004.

[57] P. W. Betteridge, J. R. Carruthers, R. I. Cooper, K. Prouta and D. J. Watkina, *J. Appl. Crystallogr.*, 2003, **36**, 1487.

[58] A. Dawson, D. R. Allan, S. Parsons and M. Ruf, *J. Appl. Cryst.*, 2004, **37**, 410–416.

[59] S. Parsons, *S.SHADE*, The University of Edinburgh, Edinburgh, United Kingdom, 2004.

[60] K. Brandenburg and H. Putz, *DIAMOND*, Crystal Impact, Bonn, Germany, 2005.

[61] I. J. Bruno, J. C. Cole, P. R. Edgington, M. Kessler, C. F. Macrae, P. McCabe, J. Pearsona and R. Taylora, *Acta Cryst.*, 2002, **B58**, 389–397.

[62] A. L. Spek, *PLATON-A multipurpose Crystallographic Tool*, Utrecht University, Utrecht University, Padualaan 8, 3584 CH Utrecht, The Netherlands, 2007.

[63] L. J. Farrugia, *J. Appl. Cryst.*, 1999, **32**, 837–838.

[64] F. H. Allen and W. D. S. Motherwell, *Acta Cryst.*, 2002, **B58**, 407–422.

[65] D. Martien, *Introduction to: AC susceptibility*, Quantum design, 2004.

[66] A. Cornia, A. C. Fabretti, R. Sessoli, L. Sorace, D. Gatteschi, A.-L. Barra, C. Daiguebonne and T. Roisnel, *Acta Cryst. Section C*, 2002, **58**, m371–m373.

[67] R. Amigó, E. del Barco, L. Casas, E. Molins, J. Tejada, I. B. Rutel, B. Mommouton, N. Dalal and J. Brooks, *Phys. Rev. B*, 2002, **65**, 172403.

[68] E. M. Chudnovsky and D. A. Garanin, *Phys. Rev. Lett.*, 2001, **87**, 187203.

[69] A. Cornia, R. Sessoli, L. Sorace, D. Gatteschi, A. L. Barra and C. Daiguebonne, *Phys. Rev. Lett.*, 2002, **89**, 257201.

[70] S. Hill, N. Anderson, A. Wilson, S. Takahashi, K. Petukhov, N. Chakov, M. Murugesu, J. North, E. del Barco, A. Kent, N. Dalal and G. Christou, *Polyhedron*, 2005, **24**, 2284–2292.

[71] M. Wojdyr, *Fityk*, 2008.

[72] R. J. Wells, *J. Quant. Spectrosc. Radiat. Transfer*, 1999, **62**, 29–48.

[73] K. Park, M. A. Novotny, N. S. Dalal, S. Hill and P. A. Rikvold, *Phys. Rev. B*, 2001, **65**, 014426.

[74] Y. Murata, K. Takeda, T. Sekine, M. Ogata and K. Awaga, *J. Phys. Soc. Jpn.*, 1998, **67**, 3014–3017.

[75] A. Caneschi, D. Gatteschi, R. Sessoli, A. L. Barra, L. C. Brunel and M. Guillot, *J. Am. Chem. Soc.*, 1991, **113**, 5873–5874.

[76] A. D. Kent, Y. Zhong, L. Bokacheva, D. Ruiz, D. N. Hendrickson and M. P. Sarachik, *Europhys. Lett.*, 2000, **49**, 521–527.

[77] M. Novak, R. Sessoli, A. Caneschi and D. Gatteschi, *J. Magn. Magn. Mater.*, 1995, **146**, 211–213.

[78] A. Sieber, R. Bircher, O. Waldmann, G. Carver, G. Chaboussant, H. Mutka and H.-U. Güdel, *Angew. Chem. Int. Ed.*, 2005, **44**, 4239–4242.

[79] R. Sessoli, D. Gatteschi, A. Caneschi and M. A. Novak, *Nature*, 1993, **365**, 141–143.

[80] Y.-C. Su, S.-Q. Shen and R.-B. Tao, *J. Magn. Magn. Mater.*, 2006, **299**, 376–382.

[81] J. A. A. J. Perenboom, J. S. Brooks, S. Hill, T. Hathaway and N. S. Dalal, *Phys. Rev. B*, 1998, **58**, 330–338.

[82] A. L. Barra, D. Gatteschi and R. Sessoli, *Phys. Rev. B*, 1997, **56**, 8192–8198.

[83] M. Murrie and S. Parsons, Private communication.

[84] A. W.-H. Lam, W.-T. Wong, S. Gao, G. Wen and X.-X. Zhang, *Eur. J. Inorg. Chem.*, 2003, 149.

[85] P. A. Wood, D. Francis, W. G. Marshall, S. A. Moggach, S. Parsons, E. Pidcock and A. L. Rohl, *Cryst. Eng. Comm.*, 2008, **10**, 1154–1166.

[86] C. A. Hunter, J. Singh and J. M. Thornton, *J. Mol. Biol.*, 1991, **218**, 837–846.

[87] R. O. Gould, A. M. Gray, P. Taylor and M. D. Walkinshaw, *J. Am. Chem. Soc.*, 1985, **107**, 5921–5927.

[88] S. Negoro, H. Asada, M. Fujiwara and T. Matsushita, *Inorg. chem. comm.*, 2003, **6**, 357–360.

[89] D. L. Hughes, U. Kleinkes, G. J. Leigh, M. Maiwald, J. R. Sanders, C. Sudbrake and J. Weisner, *J. Chem. Soc., Dalton Trans.*, 1993, **20**, 3093.

[90] C. A. Root, J. D. Hoeschele, C. R. Cornman, J. W. Kampf and V. L. Pecoraro, *Inorg. Chem.*, 1993, **32**, 3855–3861.

[91] M. Mathew, A. J. Carty and G. J. Palenik, *J. Am. Chem. Soc.*, 1970, **92**, 3197–3198.

[92] S. A. Moggach, D. R. Allan, C. A. Morrison, S. Parsons and L. Sawyer, *Acta Cryst. Section B*, 2005, **61**, 58–68.

[93] S. A. Moggach, W. G. Marshall and S. Parsons, *Acta Cryst. Section B*, 2006, **62**, 815–825.

[94] A. Caneschi, D. Gatteschi, N. Lalioti, C. Sangregorio, R. Sessoli, G. Venturi, A. Vindigni, A. Rettori, M. G. Pini and M. A. Novak, *Angew. Chem. Int. Ed.*, 2001, **40**, 1760–1763.

[95] S. A. Moggach, K. W. Galloway, A. R. Lennie, P. Parois, N. Rowantree, E. K. Brechin, J. E. Warren, M. Murrie and S. Parsons, *Cryst. Eng. Comm.*, accepted.

[96] H. Weihe and H. U. Güdel, *J. Am. Chem. Soc.*, 1997, **119**, 6539–6543.

[97] R. N. Mukherjee, T. D. P. Stack and R. H. Holm, *J. Am. Chem. Soc.*, 1988, **110**, 1850–1861.

[98] M. Gerloch, E. D. McKenzie and A. D. C. Towl, *J. Chem. Soc. A*, 1969, 2850–2858.

[99] F. E. Mabbs, V. N. McLachlan, D. McFadden and A. T. McPhail, *J. Chem. Soc., Dalton Trans.*, 1973, 2016–2021.

[100] R. E. Norman, R. C. Holz, S. Menage, L. Que, J. H. Zhang and C. J. O'Connor, *Inorg. Chem.*, 1990, **29**, 4629–4637.

[101] G. Haselhorst, K. Wieghardt, S. Keller and B. Schrader, *Inorg. Chem.*, 1993, **32**, 520–525.

[102] Y.-X. Zhou, X.-F. Zheng, D. Han, H.-Y. Zhang, X.-Q. Shen, C.-Y. Niu, P.-K. Chen, H.-W. Hou and Y. Zhu, *Synthesis and Reactivity in Inorganic, Metal-Organic, and Nano-Metal Chemistry*, 2006, **36**, 693–699.

[103] M. Gerloch and F. E. Mabbs, *J. Chem. Soc. A*, 1967, 1900–1908.

[104] Z. Sun, D. Ruiz, N. R. Dilley, M. Soler, J. Ribas, K. Folting, M. B. Maple, G. Christou and D. N. Hendrickson, *Chem. Commun.*, 1999, 1973–1974.